Characterization of MnZn Ferrite Materials and Finite Element Method for MnZn Ferrite Core Loss Calculations

by

Ping Han

Thesis submitted to the Faculty of the
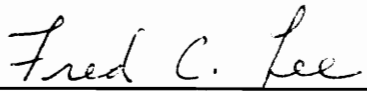
Virginia Polytechnic Institute and State University

in partial fulfillment of the requirements for the degree of
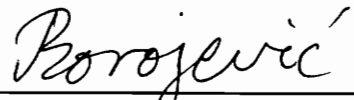
MASTER OF SCIENCE

in

Electrical Engineering

APPROVED :

Fred C. Lee

Fred C. Lee, Chairman

Dan Y Chen

Dan Y. Chen

Borojevic

Dusan Borojevic

September, 1995

Blacksburg, Virginia

C.2

Characterization of MnZn Ferrite Materials and Finite Element Method for MnZn Ferrite Core Loss Calculations

by

Ping Han

Fred C. Lee, Chairman

Electrical Engineering

(ABSTRACT)

This work presents the method of calculating the core loss in ferrite cores by using a linear and sinusoidal finite element solver based on the material property data (the complex permeability, the dielectric constant, and the AC conductivity) measured in the laboratory. Due to the lack of published material data and fundamental test procedures, this work also demonstrates the measurement techniques of material data which are necessary for the finite element analysis (FEA) of the ferrite core loss.

First, a linear mathematical model of the ferrite core loss is formulated to characterize the hysteresis loss and the eddy current loss. The magnetic properties (the real and the imaginary components of the complex permeability) and the electric properties (the dielectric constant and the conductivity) are required.

Second, the experimental procedures of those four properties are first presented. Toroids with 1.1 OD/ID ratios are selected as samples to obtain the magnetic properties. It is illustrated that the hysteresis loss should be measured at the frequency of interest, instead of DC, due to its frequency-dependence. The electric property data of ferrites are

collected by using a disk sample which forms a capacitor. The conductivity tested is frequency-dependent due to the combination of the dielectric loss and the DC conduction loss.

Finally, core loss simulations for the sample toroid, an EE core, and an RM10 core are performed and compared with the measurements. The flux and loss distributions are demonstrated in the last two cores. The hot spots are identified from the field plots.

Acknowledgements

I must express my deepest gratitude to my advisor, Dr. Fred C. Lee, for his encouragement, support, and insight. His initiative and guidance enabled me to complete this work. His great intelligence and endless enterprising spirit have influenced my character. I would like to thank my Master's committee members, Dr. Dan Y. Chen, and Dr. Dusan Borojevic, for their suggestions regarding this research. I am especially thankful to Mr. Glenn R. Skutt. who made significant contributions to this creative work with his knowledge and experiences. I am grateful to all the faculty, staff and students at the Virginia Power Electronics Center (VPEC) for their technical assistance and friendly help. In particular, I would like to express my appreciation to Mr. Ju Zhang, Mr. Kunrong Wang, Mr. C. Y. Lin, Mr. Wei Chen, Ms. Ning Dai and Prof. Xingfun Zhuang for sharing their valuable experience during our numerous discussions. I thank Mr. Alex Shpilman, Philips; Mr. Chris Mathis, Magnetics; Mr. John Gilmore, Ansoft Company; and Jim

Florence, Ceramic Magnetics, who provided a lot of technical consultation and material support for this research. I am greatly thankful to my father Xianchang Han and my mother Yuwen Song for their bringing me up and encouraging me to pursue excellence and take new challenges. Finally, I would like to dedicate my thesis to my dear husband Zhenguo Yuan and my lovely daughter Wendy Yuan for their love, support, and understanding through the course of this research.

Table of Contents

1. Introduction

1.1 Background and Objective

The trend of power electronics circuit development is towards high efficiency and miniaturization. Magnetic device design is critical to reducing the size and increasing the efficiency of power electronics circuits.

In order to minimize the size for a given throughput power, inductors and transformers are usually subject to high-frequency and large-amplitude excitations. A designer must be able to accurately compute the losses in the magnetic components which affect the efficiency of the whole circuit.

Generally speaking, the power dissipation in inductors or transformers is composed of the winding loss and the core loss. The winding loss at high frequencies is the summation of the DC conduction loss, the eddy effect loss, and the proximity loss. Numerous papers [1,2,3,4, 5,6,7,8, 9,10,11] have been published to date dealing with winding loss analysis

by using one- or two- dimensional analytical calculations. Several commercial finite element solvers [12,13,14,15] are available to deal with winding loss analysis easily which feature visualization of flux distribution and current distribution in the winding. The broad topic on the winding loss examination will not be addressed here. This work only concentrates on the loss analysis of ferrite cores.

Power ferrites are widely used as the core materials of the transformers and inductors in the power electronics circuits. Such core materials are of both ferromagnetic and semiconductive natures so that they have high permeability and low eddy current loss at high frequencies. Therefore, they are widely used for the high-frequency applications. Since power ferrites have non-linear permeability (saturation and hysteresis), frequency-dependent conductivity, and temperature-sensitive permeability and conductivity [16,17,18,19]—those characteristics are not provided by the manufacturers[20] — core loss analysis cannot be readily performed based on the material data. Core loss values are normally obtained from the measurements[21,22].

The experimental method proposed by Thottuvelil [21] is to measure total core losses for any specific devices under sinusoidal or arbitrary excitation conditions. However, the measurements require expensive specialized instruments and are usually limited to a certain frequency and flux density range. The measurement provides only the value of total core loss. The information about loss distributions is unknown, and the hot spots due to non-uniform loss distribution in the devices cannot be identified.

Mulder proposed an empirical method [22], where a representative small toroidal core was selected to ensure that the hysteresis loss dominated the eddy current loss in the core. Therefore, the measured loss was assumed to be the hysteresis loss only. After the loss density data were acquired at different frequency and flux density levels under sinusoidal excitation conditions, the hysteresis loss density, P_{h_d}, was expressed as an exponential function of the frequency, f, and the peak flux density, B_m, at a particular temperature by using the curve-fitting technique

$$P_{h\_d} = kB^m f^n, \tag{1.1}$$

where k, m, and n are constants. For any other shape cores with the same core material, the hysteresis loss density can be calculated from Eq. (1.1), the eddy current loss density, P_{e_d}, can be computed according to a standard expression,

$$P_{e\_d} = \pi B^2 f^2 A_e \sigma / 4, \tag{1.2}$$

where A_e and σ stand for the effective cross-sectional area and conductivity of the core material, respectively. The major advantage of this method over the previous experimental method [21] is its capability of calculating the core loss in a variety of cores analytically. This method makes possible the computer-aided design (CAD) for magnetic devices. However, the loss distributions within a core are still unavailable.

The FEA is obviously a useful numerical method to analyze the loss distributions and calculate the total loss in the transformers and inductors, and it should be widely used for the core loss analysis. Ideally, the complete FEA solution for the core loss must be capable

of addressing the nonlinear ferrite material characteristics, making electro-thermal simulation possible, and offering provision to cope with anisotropic and inhomogeneous materials. Unfortunately, such an FEA solver has not been developed yet. Also, the material characteristic data for ferrites under a variety of excitation and environmental conditions must be available for the numerical simulation. But manufacturers generally provide only some limited data under DC or sinusoidal excitation conditions. Particularly, only DC conductivity, curves of initial permeability vs. frequency, initial permeability vs. temperature, and amplitude permeability for some particular frequency and temperature points are provided. Dielectric constant information is usually not available, or is available at DC. The lack of needed material data impedes the use of FEA to quantify the ferrite core loss.

In Reference [23], a nonlinear FEA program (EMAS®) was used in combination with other programs to compute total loss in iron cores under sinusoidal input conditions. But the applicability of extending such a method to ferrite cores was not addressed.

The FEA of the ferrite core loss was investigated by the authors in [24] using the following approximations:

1. the excitation waveform is sinusoidal;

2. the ferrite material properties are linear, isotropic, and homogenous;

3. the hysteresis loss is represented by the imaginary component of permeability.

Two approaches towards the core loss simulations were presented: the combined loss approach which lumps all the core losses into one loss term, and the separated loss

approach which divides the total core loss into the eddy current loss and the hysteresis loss. The former method was not able to produce the correct breakdown of losses and provided incorrect loss distribution, even though the calculated total core loss was accurate. The latter method assumed that the measured core loss from a toroidal sample at 1 kHz represented the hysteresis loss. The eddy current loss accounts for the difference between the high-frequency loss and low-frequency loss of the sample core. Then an effective conductivity, σ_{eff}, which was used as one of the core material data in the simulation, can be calculated from the loss difference according to Eq. (1.2). The successful simulations of the sample toroid were presented in the paper. However, since the σ_{eff} is much greater than the material conductivity, it results in the smaller skin depth and the overestimation of the eddy effect. After the paper was published, the latter method was used to simulate the core loss in an RM10 core as a part of our research. Unfortunately, the calculated losses were much smaller than the measured loss. It means that this type of the hysteresis loss and the eddy current loss separation is impractical so that it is hard to apply to differently shaped cores, such as an RM core.

The objective of this thesis is to improve the separated loss method proposed in [24] and to simulate the core loss in ferrite cores correctly by a linear and sinusoidal FEA solver, Maxwell®. Since the ferrite material properties (the complex permeability, the conductivity, and the dielectric constant) are used as the input data of the simulations, the characterization of the ferrite materials is the most important to the accuracy of the loss analysis. The error existing in the latter method[24] was due to the misuse of the

imaginary permeability and the conductivity. This work will initiate a characterization approach towards ferrite materials based on the understanding of the loss mechanisms of the ferrites. Eventually, the FEA of the core loss will be performed on a sample toroid core, an EI core, and an RM core, to show the correctness of the material characterization and the ability to visualize field and loss distributions.

1.2 Outline of the Work

Since MnZn ferrites are popular core materials for the magnetic devices in the power electronics circuits, this work concentrates only on MnZn ferrites. But all the rules found in MnZn ferrites can be applied to NiZn ferrites as well.

1.2.1. Loss Mechanisms and a Mathematical Model of Ferrites

In order to simulate the core loss correctly by using a linear FEA solver, it is essential to understand the real physics of the ferrite losses. Such an understanding will explain the approximations made in the linearization process and will facilitate the development of a mathematical model for the core loss in a ferrite core.

The first part of Chapter 2 discusses the physical background of the core loss. The second part illustrates how a nonlinear hysteresis loop is modeled by an ellipse. In the end,

the core loss formula derived from Maxwell's equations and the Poynting theorem shows how the total loss is classified into the hysteresis loss and the eddy current loss.

On the one hand, Chapter 2 provides the theoretical basis for the core loss analysis by using a linear FEA solver; on the other hand, it reveals that the complex permeability, the AC conductivity, and the dielectric constant are required in the simulations.

1.2.2 Characterization of MnZn Ferrite Materials

Chapter 2 clearly states which material data are needed in the simulation of the ferrite core loss. Chapter 3 demonstrates the acquisition procedures of the material characteristic data and the test setups. Also, the sample selections which affect the accuracy of the material data measurements are discussed.

Since ferrites combine the ferromagnetic and dielectric characteristics, the magnetic and the electric property measurements need to be performed separately.

The magnetic properties include the real component of the permeability and the imaginary component of the permeability which can be converted from the measured core loss. This work uses impedance approach[25] to characterize the two components of the complex permeability and core loss. The permeability of ferrites are the frequency, the flux density, and the temperature dependent. The room temperature (23~25°C) is used in this work to limit the permeability variation due to the temperature.

The electric properties of ferrites, the conductivity and the dielectric constant, are measured. A lossy capacitor model [16] is employed to measure these two properties under different frequencies. They are tested at the room temperature also and under small-signal excitations.

In order to provide the measurement data for the simulations to compare with, the core loss values are obtained from experimental testing on an EI and an RM10 cores. The effective dimensions are included in the measurements to deal with a device with uneven flux distribution as an ideal device with uniform flux distribution. The inaccuracy of those dimensions are examined theoretically

1.2.3 Examples of Finite Element Simulations for Core Loss

Chapter 4 describes the simulations with a 2D or 3D linear FEA solver, Maxwell®. Three differently shaped cores (a very thin toroid, an EI core and an RM10 core) with the same ferrite material are simulated. The simulated losses are compared with the measured core losses. They match very well with less than 5% error for the very thin toroid. They have 25% and 15% differences for the EI and the RM10 cores, respectively. The main reason for the deviations is the use of the effective dimensions in the core loss tests.

Since the advantage of using FEA to examine the core loss is the ability to see the field and the loss distributions, Chapter 4 shows the pictures of those distributions in the

EI core and the RM10 core. The pictures provide a lot of information on the field and the

core losses, such as the hot spot locations in the core.

2. Loss Mechanisms and a Mathematical Model of Ferrite Core Loss

2.1 Loss Mechanisms of Magnetic Cores

The core loss is usually divided into the hysteresis loss, the eddy current loss, and the residual loss [26]. For the power electronics applications which are under large-amplitude and high-frequency operating conditions, the hysteresis loss is mainly caused by the irreversible rotation of magnetization[17] and only depends on the chemical composition, microscopic structure, and internal stresses of the core material. The eddy current loss is due to the current induced in the core under the alternating magnetic flux, and determined by the conductivity of the core material and the cross-sectional area which the flux goes through. The residual loss is generated by the power dissipation resulting from the reversible domain wall damping [27] and the reversible rotation of domains [28]. Under large magnitude conditions, most of the domain walls are extinct so that the residual loss can be ignored [29].

Figure 2.1 shows the nonlinear B-H curve with hysteresis which reflects the principal characteristics of the ferromagnetic material. When an unmagnetized ferromagnetic core is excited, the trajectory starts from the origin and increases along the B-H curve without hysteresis (the initial magnetization curve). The slope of the initial magnetization curve at the original point is defined as the initial permeability, μ_I. If the core is excited by an alternating cyclical signal, B increases with H in the lower limp and decreases in the upper limp. If H keeps increasing, but B stops going up, the maximum flux density is called the saturation, B_{SAT}. When H vanishes, the flux density is not equal to zero. This flux density is referred to as the remanence of the material, B_r. When B becomes zero, the non-zero value of H is referred to as the coercivity, H_c. When the peak flux density of the alternating cyclical excitation changes, the ratio of B to H at the tip of the loop is defined as the amplitude permeability, μ_a. The amplitude permeability, not the initial permeability, reflects the characterization of the magnetic devices in the power electronics circuits because of the large amplitude excitations in the circuits.

The nonlinear hysteresis loop has been successfully described in analytical forms in the past [17,30,31]. However, the developed formulae are rather complicated. In order to represent core material properties more conveniently, Snelling proposed the concept of the complex permeability under sine wave excitation conditions [16]. Assuming that the core operates at the linear region, the hysteresis loop can be approximated as an ellipse as shown in Fig. 2.2. Although the linearized hysteresis model cannot handle saturation, it is very useful to the loss examinations for most of the magnetic devices in power electronics.
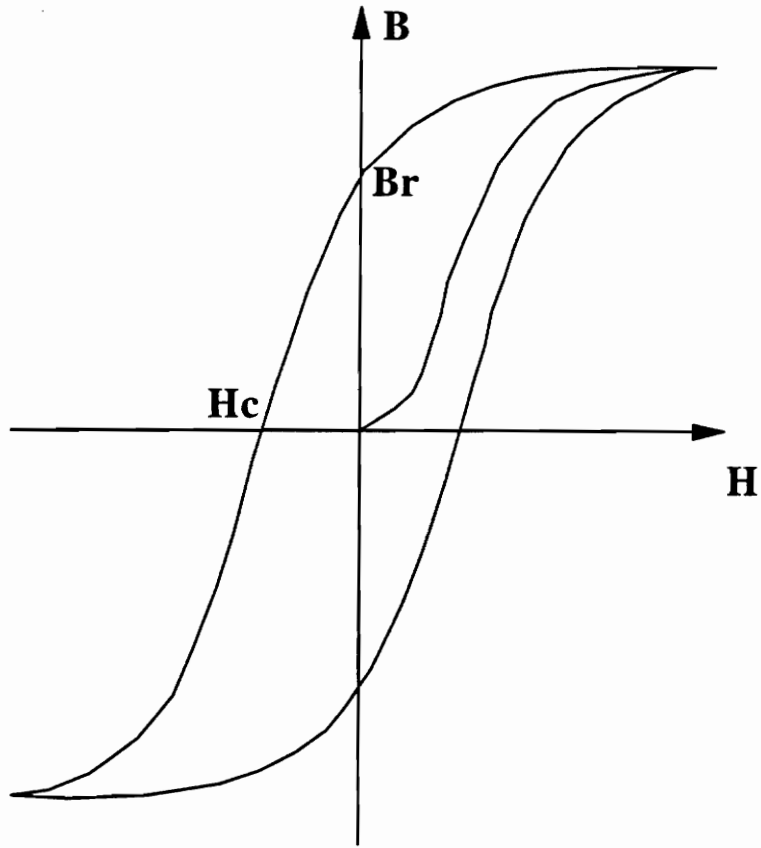
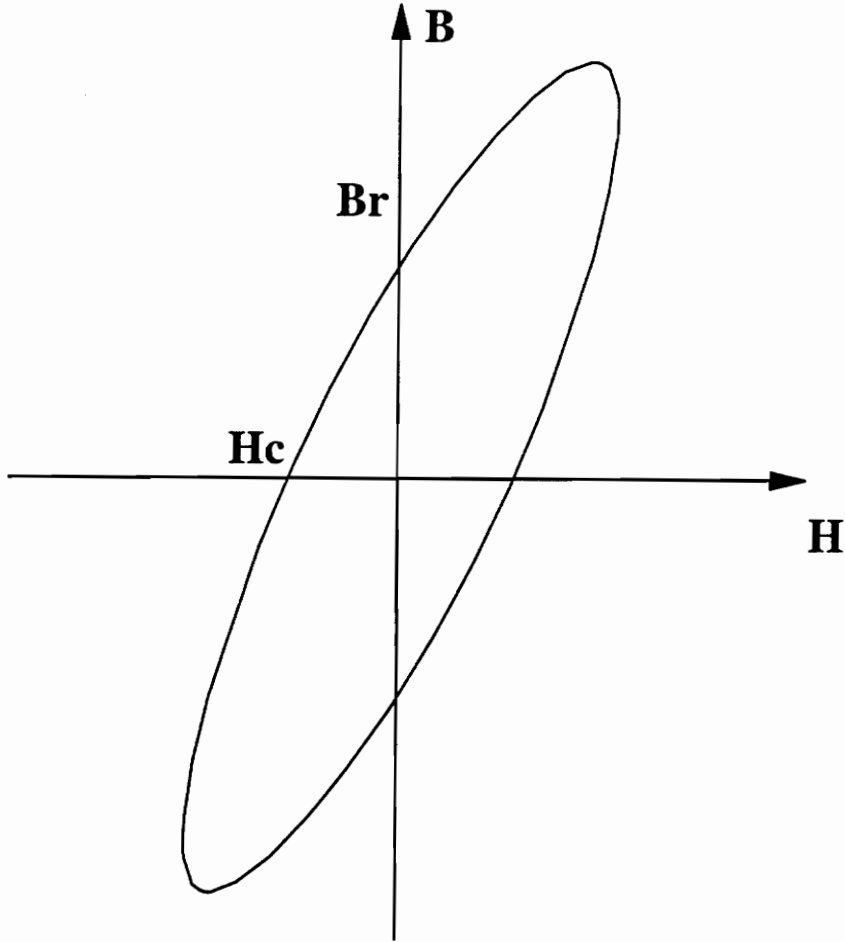Fig. 2.1 The B-H curve of a ferromagnetic material

Fig. 2.2 An approximate B-H curve with hysteresis (an ellipse)

The hysteresis loss occurs when B lags H. The permeability now is a complex number, $\overline{\mu}$, which includes the real component, μ', and the imaginary component, μ'',

$$\overline{\mu} = \mu' - j\mu''. \tag{2.1}$$

In Fig. 2.3, μ'', which is associated with the hysteresis loss, can be represented by

$$\mu'' = \frac{B_r}{H_m}; \tag{2.2}$$

μ', which is associated with the energy storage in the magnetic field, can be expressed as,

$$\mu' = \frac{\sqrt{B_m^2 - B_r^2}}{H_m}. \tag{2.3}$$

2.2 An FEA Mathematical Model of the Ferrite Core Loss

The purpose of this research is to use a linear FEA solver, Maxwell®, to calculate the ferrite core loss under sinusoidal excitation conditions. The total loss, $\sum P$, in a ferrite core can be derived based on Maxwell's equations combined with Poynting theorem (see Appendix A) in the form,

$$\sum P = \frac{1}{2} \int_v \Re e[H^* \cdot (j\omega B) + E \cdot J^* - E \cdot (j\omega D^*)]dv, \tag{2.4}$$

where   H is the magnetic field intensity,

B is the magnetic flux density,

E is the electric field intensity,

D is the electric-flux density,

J is the conduction current density,

H, B, E, D, and **J** are phasors, and

* is complex conjugate.

In linear, homogeneous and isotropic media, there are several constitutive relations between field quantities,

$$B = \mu H \tag{2.5}$$

$$D = \varepsilon E \tag{2.6}$$

$$J = \sigma E, \tag{2.7}$$

where μ, ε, and σ are the amplitude permeability, the dielectric constant, and the conductivity, respectively. As has been discussed in the previous section, μ in a ferrite material is a complex number under sine wave excitations. Similarly, ε is also a complex number in a ferrite material[16],

$$\varepsilon = \varepsilon' - j\varepsilon'', \tag{2.8}$$

where the real part, ε', is related to the electric energy in the field; the imaginary part, ε'', is related to the dielectric loss.

Substitution of Eqs. (2.1) and (2.5) ~ (2.8) into Eq. (2.4) yields

$$\sum P = \frac{1}{2}\int_v \Re e[H^* \cdot (j\omega\mu'H) - E \cdot (j\omega\varepsilon'E^*)]dv$$

$$+ \frac{1}{2}\int_v \Re e[\omega\mu''H^* \cdot H + \omega\varepsilon''E \cdot E^* + E \cdot J^*]dv. \tag{2.9}$$

Since both $H^* \cdot H$ and $E^* \cdot E$ are real phasors, $H^* \cdot (j\omega\mu'H) - E \cdot (j\omega\varepsilon'E^*)$ is

a purely imaginary term, and therefore its real component equals zero. As a result, the first

term in Eq. (2.9) is zero. Similarly, since $\omega\mu''H^* \cdot H + \omega\varepsilon''E \cdot E^* + E \cdot J^*$ is real,

$$\Re e(\omega\mu''H^* \cdot H + \omega\varepsilon''E \cdot E^* + E \cdot J^*)$$

$$= \omega\mu''H^* \cdot H + \omega\varepsilon''E \cdot E^* + E \cdot J^*. \tag{2.10}$$

Eventually, Eq. (2.9) can be simplified to,

$$\sum P = \frac{1}{2}\int_v (\omega\mu''H^* \cdot H)dv + \frac{1}{2}\int_v (\omega\varepsilon''E \cdot E^*)dv + \frac{1}{2}\int_v (E \cdot J^*)dv. \tag{2.11}$$

The first, second, and third terms in Eq. (2.11) represent the hysteresis loss, the dielectric

loss, and the ohmic loss, respectively. These are the loss mechanisms existing in a linear,

homogeneous, and isotropic medium with complex permeability and complex dielectric

constant. The last two terms can be combined into one eddy current loss term, P_e, which

can be expressed by either P_{e1} or P_{e2}:

$$P_{e1} = \frac{1}{2}\int_v (\omega\varepsilon_{AC}''E \cdot E^*)dv \tag{2.12}$$

$$P_{e2} = \frac{1}{2}\int_v \frac{J \cdot J^*}{\sigma_{AC}}dv, \tag{2.13}$$

where ε''_{AC} in Eq. (2.12) is the AC value of the imaginary part of the dielectric constant and σ_{AC} in Eq. (2.13) is the AC conductivity. Both ε''_{AC} and σ_{AC} cover the DC conduction loss and the dielectric loss. The solver, Maxwell®, uses σ_{AC} as one of the input material data and uses Eq. (2.13) to calculate the eddy current loss.

In other words, the total core loss is computed in Maxwell® by,

$$\sum P = \frac{1}{2}\int_v (\omega\mu'' H^* \cdot H)dv + \frac{1}{2}\int_v \frac{J \cdot J^*}{\sigma_{AC}}dv. \qquad (2.14)$$

The material data required are μ', μ'', ε, and σ_{AC}.

3. Characterization of MnZn Ferrites

Chapter 2 has illustrated that the complex permeability, the AC conductivity, and the dielectric constant are the material properties required in the FEA of the ferrite core loss. This chapter will discuss how to measure those properties in the laboratory.

Since ferrites are ferromagnetic and semiconductive materials, they have the magnetic properties (the real and imaginary components of the permeability) and the electric properties (the AC conductivity and the dielectric constant).

3.1 Magnetic Property and Core Loss Measurements

3.1.1 Magnetic Property Measurement

The impedance approach [25] is employed to measure the complex permeability in this study. When an N-turn winding is wound on an ideal loss-free toroidal core with

cross-sectional area, A, and magnetic mean length, l, the impedance of the winding is a pure reactance,

$$Z = j\omega L = j\omega\mu_0\mu N^2 A / l,$$ (3.1)

where μ is the real permeability of the toroid. Practically, the core is lossy and the impedance of the winding has a resistive part, r_s, as well as a reactive part, L_s,

$$Z = r_s + j\omega L_s = j\omega\mu_0\bar{\mu}N^2 A / l,$$ (3.2)

where $\bar{\mu}$ is the complex permeability (see Eq. 2.1). r_s can be expressed as the imaginary component, μ'', of the complex permeability,

$$r_s = \omega\mu_0\mu''N^2 A / l.$$ (3.3)

Such a series lossy inductance model can be alternatively represented by a parallel inductive circuit which is shown in Fig. 3.1. The impedance can be also expressed as,

$$Z = \cfrac{1}{\cfrac{1}{r_p} + \cfrac{1}{j\omega L_p}},$$ (3.4)

where r_p and L_p can be represented by the imaginary component, μ'', and the real component, μ', of parallel complex permeability,

$$r_p = \omega\mu_0\mu_p''N^2 A / l$$ (3.5)

$$L_p = j\omega\mu_0\mu_p'N^2 A / l.$$ (3.6)
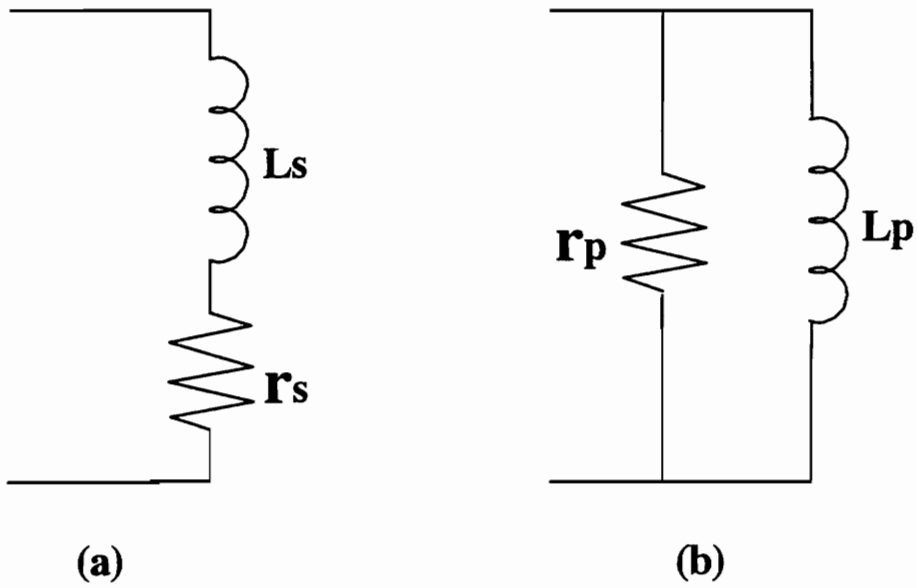
Fig. 3.1 A lossy inductor model

(a) Series model   (b) Parallel model

If a voltage driving source is used in the experiment, it is appropriate to select the parallel model because the voltage applied to the lossy inductor is the voltage dropped across the pure inductor, L_p. The peak flux density, B_m, in the core can be specified by adjusting the voltage applied to the device under test (DUT), V_{DUT},

$$V_{DUT} = 4.44 N f B_m A. \tag{3.7}$$

In the series model, however, the voltage across L_s is a function of the frequency and the source voltage. Therefore, it is not easy to control the flux density by monitoring the source voltage.

The test setup is shown in Fig. 3.2. A Hewlett-Packard HP 4194A impedance analyzer is controlled by a personal computer through the GPIB interface. The small signal sinusoidal output of the impedance analyzer — which is less than 1.2 V — is amplified to a large AC signal by a wideband power amplifier, Amplifier Research 10A250 or 700A1, and then applied to the DUT through the HP 4194A impedance probe. The probe can withstand currents up to 0.5 A and voltages of 150 V. This voltage across and the current in the DUT are then reduced by the 30-dB attenuators (PASTERNACK PE7010-30) and input to the test channel (T ch.) and the reference channel (R. ch.), respectively. The software controls the voltage across DUT, V_{DUT}, according to the required flux density, B_m, and frequency, f. Since the maximum voltage specified in the test channel is 1 V, the maximum voltage which can be applied to the DUT, V_{DUTmax}, is 30 dBV($\approx$31.62V). Once $V_{DUT,max}$ reaches 30 dBV, the software will shut down the measurement automatically.
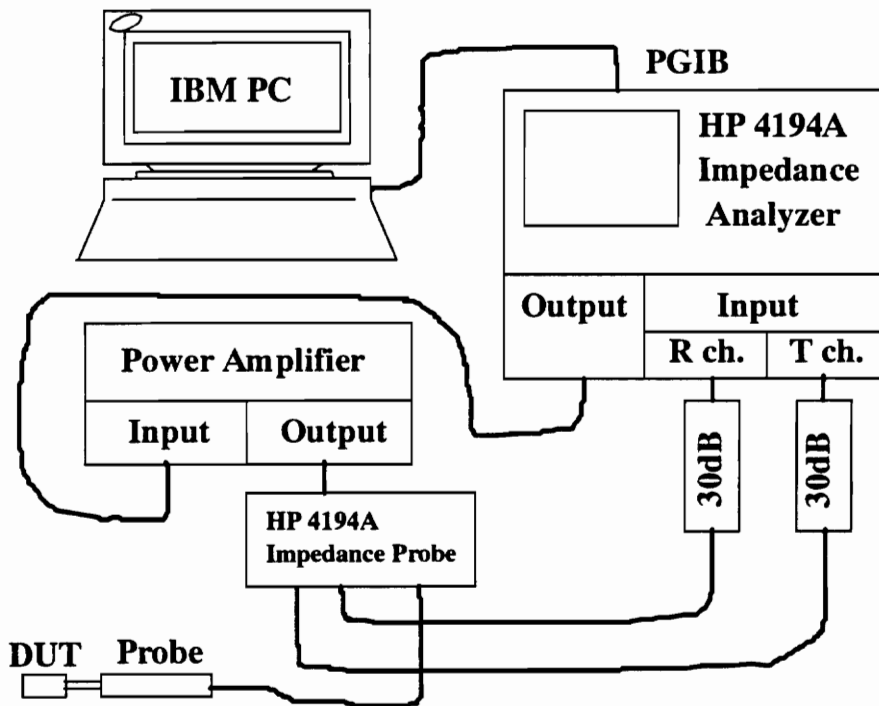
Fig. 3.2 Setup of a high-frequency core loss measurement system by using impedance approach

The Amplifier Research 700A1 is very powerful, with high gain and variable output impedance. It should be noted that the voltage gain of the amplifier cannot be set too large when the specified flux density is relatively high. Although this restriction may limit the measurable range of the flux density, it will protect the amplifier from overload. The reference and test channels have two options for input signals: 0 dB or 20 dB. Normally, the test channel, which detects relative large voltage of the DUT through a 30-dB attenuator, selects 20 dB, while the reference channel, which detects the relatively small current signal of the DUT through a 30-dB attenuator, employs 0 dB. Under a large flux density condition, the current flowing to the reference is large enough to overload the channel. The software enables the user to choose a proper attenuation.

The accuracy of the measurements depends, to a great extent, on eliminating parasitic effects in the system through proper calibrations (zero-short, zero-open, and 50-Ω). The calibration setup is shown in Fig. 3.3. The winding loss introduced by the test coil can be calibrated out by an identical coil with an air core during zero-short compensation process. Considering that this portion of loss is very small compared with the core loss, a 0-Ω standard is used instead. Since two 30-dB attenuators exist, the maximum output (OSC level = 1.2 V) should be used to get more accurate calibration data. The accuracy of the calibrations can be examined by the impedance test for 0-Ω and 50-Ω standards.

The selection of the sample toroid is very important to the accuracy of the complex permeability. Commercial toroids normally have a 1.5 ~ 2.0 OD/ID ratio [32], which
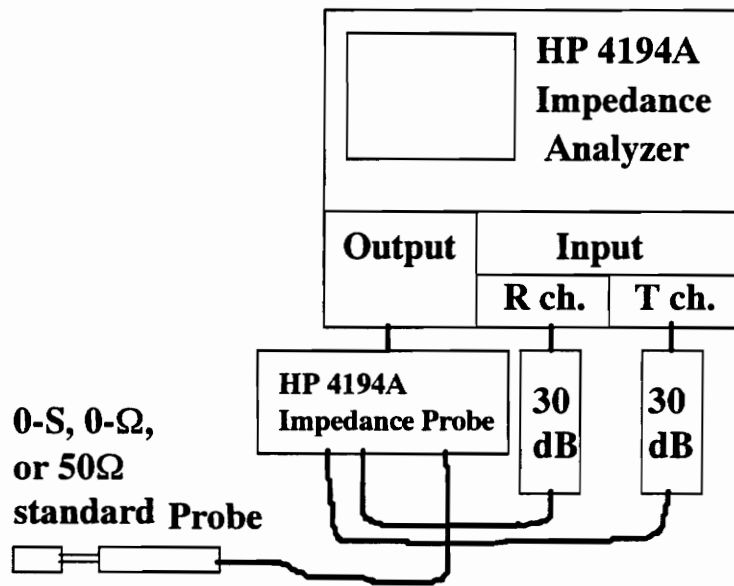
Fig. 3.3 Calibration setup of the core loss measurement system shown in Fig. 3.2

makes the flux density greatly non-uniform in the cross section. The effective dimensions — the effective cross-sectional area, A_e, the effective magnetic length, l_e, and the effective core volume, V_e — are used to approximate an actual toroid by a hypothetical toroid with a uniform flux distribution on any cross sections of the core. Those effective dimensions are defined[16] assuming that the flux density is low enough for the Rayleigh or Peterson relation to hold:

$$\frac{B}{\mu_0} = (\mu_i + v\hat{H})H \pm \frac{v}{2}(\hat{H}^2 - H^2),$$ (3.8)

where **B** and **H** are momentary values, $\hat{H}$ is the peak value of field strength, μ_i is the relative initial permeability, and v is the Rayleigh hysteresis coefficient. However, the magnetic devices in power electronics circuits are under large amplitude conditions, such that Rayleigh or Peterson relation is not valid. Although the effective dimensions are still used in practice under large amplitude of flux density conditions for convenience, they should not be used here because accurate material data are required. To be rigorous, toroids with very small radial thicknesses (i.e. OD/ID ratios close to unity) should be selected to guarantee uniform flux distribution in the cores. In this research, the MnZn BE2 ferrite toroids, manufactured by Ceramic Magnetics with 1.1 OD/ID ratio listed in Table 3.1 are used as sample cores. There are three sizes and four samples for each size. In such thin cores, the eddy current loss is negligibly small and is assumed to be zero. In other words, another advantage of using those thin cores is that the measured loss can be taken as the hysteresis loss.

Table 3.1 Dimensions of MnZn BE2 ferrite toroidal cores made by Ceramic Magnetics

Core Name	OD mm	ID mm	THK* mm	A* m²	l* m
BE2 #1a	33.11	30.11	5.06	7.59E-6	9.93E-2
BE2 #1b	33.07	30.05	4.99	7.53E-6	9.90E-2
BE2 #1c	33.11	30.09	5.07	7.65E-6	9.93E-2
BE2 #1d	33.12	30.08	5.06	7.69E-6	9.93E-2
BE2 #2a	39.39	35.66	4.96	9.25E-6	1.18E-1
BE2 #2b	39.39	35.67	5.06	9.42E-6	1.18E-1
BE2 #2c	39.41	35.69	5.01	9.32E-6	1.18E-1
BE2 #2d	39.37	35.65	5.07	9.44E-6	1.18E-1
BE2 #3a	21.90	19.96	4.96	4.81E-6	6.58E-2
BE2 #3b	21.88	19.85	5.00	5.08E-6	6.55E-2
BE2 #3c	21.89	19.95	4.89	4.74E-6	6.57E-2
BE2 #3d	21.87	19.83	5.00	5.10E-6	6.55E-2

* where THK, A, and l are the thickness, the cross-sectional area, and the magnetic length of the toroids, respectively.

The hysteresis loss is defined as the loss which is proportional to the area of the static B-H loop in the low flux density region [16]. Reference [33] proposed that the hysteresis loss increases with the frequency for "non-conducting" magnetic materials due to the effects of magnetic relaxation. The "non-conducting" material is the medium where the effects of eddy currents can be ignored. In order to see how the hysteresis loss changes in the very thin sample toroidal cores, the core loss is measured over high-frequency range (100 kHz ~ 1 MHz) and quasi-DC (1 kHz), which can represent the hysteresis loss at DC.

The high-frequency core loss can be measured by using the setup shown in Fig. 3.2. After r_p and L_p are obtained, the loss can be calculated by,

$$P = \frac{V_{DUT}^2}{r_p}.$$

(3.9)

The loss calculation is included in the test program so that the loss data are available as a part of output.

The high-frequency core loss system cannot give accurate results at low frequencies due to the structure of the impedance probe [34] shown in Fig. 3.4. The two DC capacitors, C1 and C2, in the impedance probe have relatively large voltage drops at low frequencies so that the voltage monitored by the test channel is larger than the voltage applied to the winding.

In order to sense the exciting voltage more accurately, the two-port approach [34] can be used to measure the low-frequency or high-frequency core loss. The two-port core loss measurement system is available in our laboratory which is controlled by a personal computer. However, since a low-frequency power amplifier is used, this setup can only handle low-frequency core loss measurements. The excitation voltage applied to the primary side of the DUT is the output sinusoidal voltage of the HP 4194A impedance analyzer fed through a low-frequency amplifier for which ±15-V source voltages are provided by two PS 503A dual power supplies. R_s is 1.035Ω. The secondary is a voltage pick-up winding which should be tightly wound to a small portion of the core to eliminate leakage flux and to ensure the accuracy of the sensed voltage. The flux density level can be specified by controlling the secondary voltage. The number of turns of the secondary, N_s, can be selected to guarantee the test channel voltage, V_{test}, less than 1V over the entire measurement range,

$$V_{test} = 4.44 N_s f B_m A_e \leq 1V \tag{3.10}$$
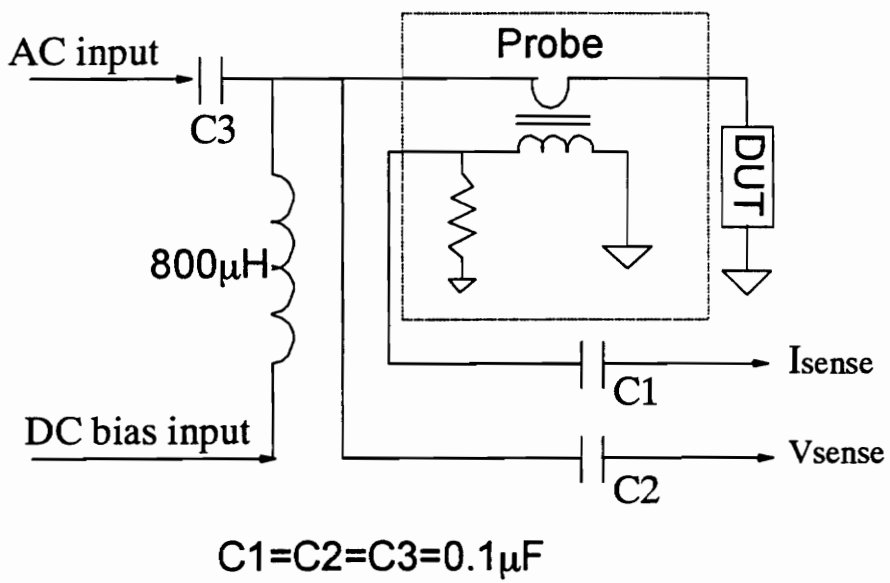
Fig. 3.4 Schematic diagram of the impedance probe
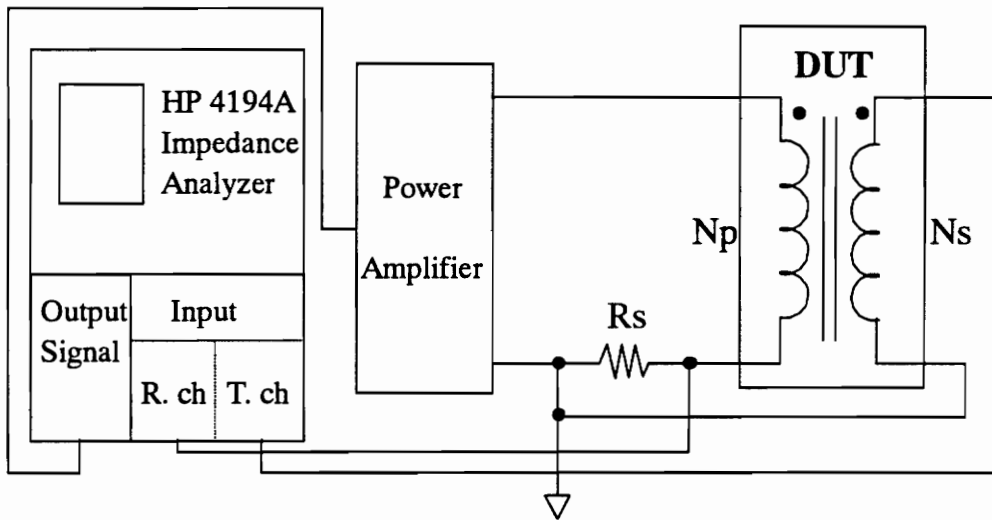
Fig. 3.5 Setup of low-frequency core loss measurement

Figure 3.6 provides the data of the hysteresis loss per cycle versus frequency for BE2 material at 50 mT, 100 mT, and 200 mT. At every constant flux density condition, the hysteresis loss per cycle increases with the frequency. It means that the material data, μ'', is a function of frequency. Using the DC value of μ'' as any high-frequency value will result in underestimation of the hysteresis loss. In other words, μ'' must be measured at the operating frequency instead of at DC.

It should be pointed out that although both the hysteresis loss and the eddy current loss are frequency-dependent, these two portions of losses are of different natures. The hysteresis loss only relies on the microstructure of the material and is independent of the geometry. However, the eddy current loss is determined by the conductivity of the material and the cross-sectional area of the core. Therefore, it is necessary to separate these two loss mechanisms.

It is obvious that the required complex permeability, μ'_s-$j\mu''_s$, should be measured at the frequency of interest. In order to guarantee the flux to be the same in any cross-sectional area and to prevent the flux leakage, the exciting winding should be uniformly and tightly wound on the sample cores. If the number of turns is not enough, several wires should be wound in parallel. The software, which controls the measurements, has the capability of testing, and then calculating μ_p' and μ_p'' based on r_p, L_p, and core dimensions according to Eqs. (3.5) and (3.6). Since the FEA solver needs μ_s' and μ_s'' as the material data, rather than μ_p' and μ_p'' , μ_p' and μ_p''
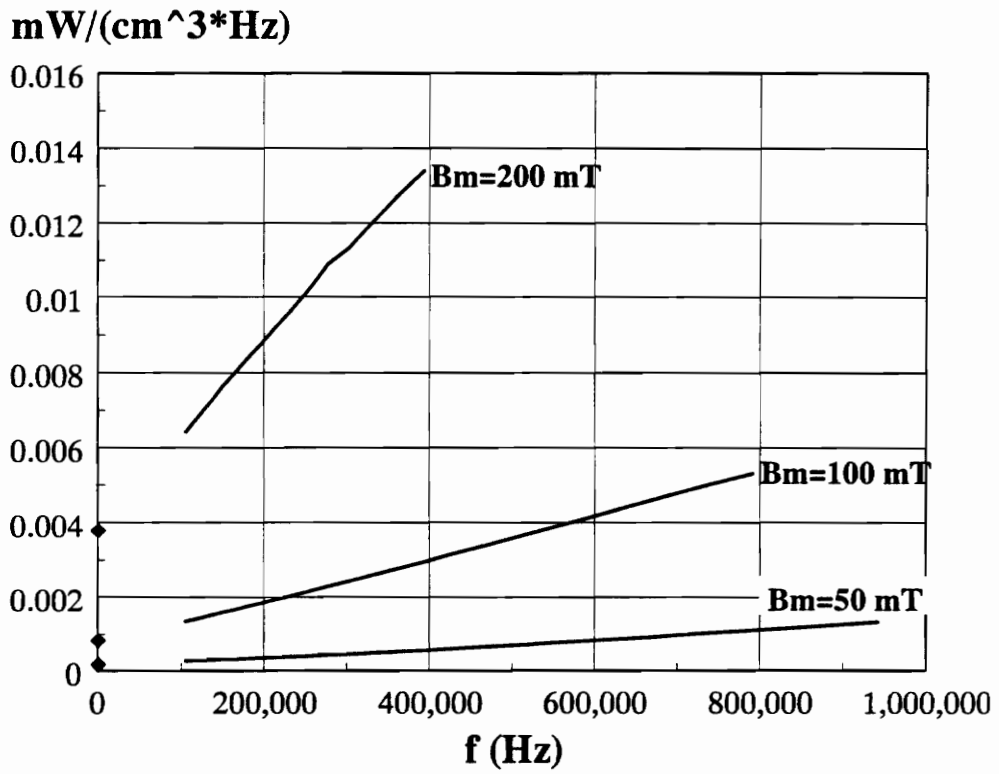
Fig. 3.6 The hysteresis loss per cycle versus frequency measured from #2c MnZn ferrite toroid

must be converted into μ_s' and μ_s''. No matter which model is used, the impedances expressed in Eqs. (3.2) and (3.4) are indentical. Therefore,

$$\mu_s' - j\mu_s'' = \frac{1}{\mu_p'} - \frac{1}{j\mu_p''}, \tag{3.11}$$

i.e.

$$\mu_s' = \frac{\mu_p'}{1 + (\mu_p''/)^2}, \tag{3.12}$$

and

$$\mu_s'' = \frac{\mu_p''}{1 + (\mu_p''/\mu_p')^2}. \tag{3.13}$$

The conversion of μ_s' and μ_s'' into μ_p' and μ_p'' can be done by means of an EXCEL program according to Eqs. (3.12) and (3.13).

The thin toroids are machined from larger block. Considering that machining effects might have happened to the surface of the cores, half of the samples (BE2#1a, BE2#1d, BE2#2b, BE2#2d, BE2#3a, and BE2#3d) are heat-treated and then measured at room temperature (23 ~ 25°C). Fig. 3.7 shows the measured hysteresis loss versus frequency at 50 mT, 100 mT, and 200 mT, respectively. The standard deviation of the loss density relative to the average value is less than 20% for the 50-mT case, and less than 13% for the 100-mT and 200-mT cases. The standard deviation of the real component relative to
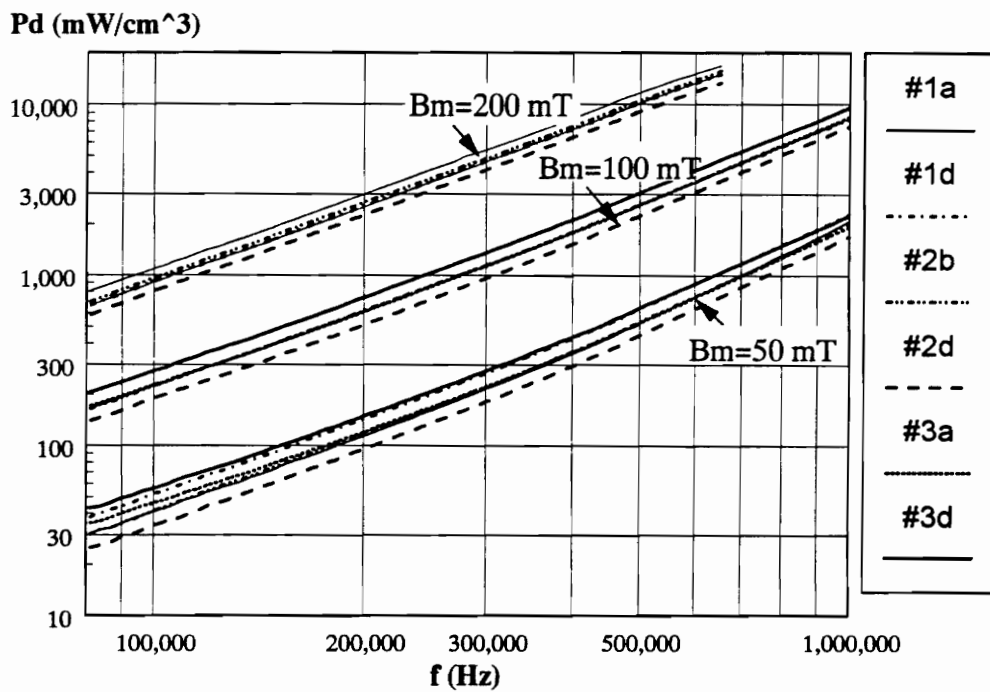
Fig. 3.7 The hysteresis loss density versus frequency measured from samples BE2#1a, BE2#1d, BE2#2b, BE2#2d, BE2#3a, and BE2#3d at 50 mT, 100 mT, and 200 mT, respectively.

the average value is less than 13% for the 50-mT case, and less than 10% for the 100-mT and 200-mT cases. Therefore, it is reasonable to use the average value of the real component of permeability and loss density (the imaginary permeability) as the material data. It is observed that the average values are very close to the values of #3a core. Therefore, it is assumed that the data collected from #3a core represent the material data. When the material properties are required at 100 kHz, 200 kHz, 300 kHz, 400 kHz, and 500 kHz, only #3a core is tested instead of all the sample cores.

Eventually, the values of complex series permeability, $\mu_s' - j\mu_s''$, can be obtained at the different conditions, as shown in Figs. (3.8) ~ (3.10). The data will be used as input magnetic material properties for the FEA of the ferrite core loss.

Mus'
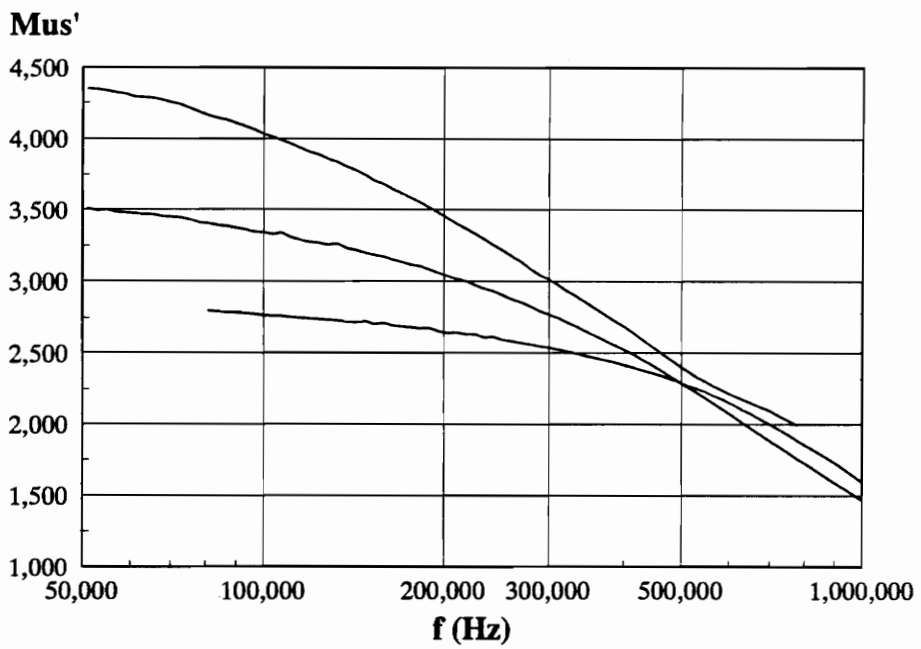
Fig. 3.8 The real component of the series permeability measured from BE2#3a toroidal core at $B_m = 50$ mT, 100 mT and 200 mT, respectively
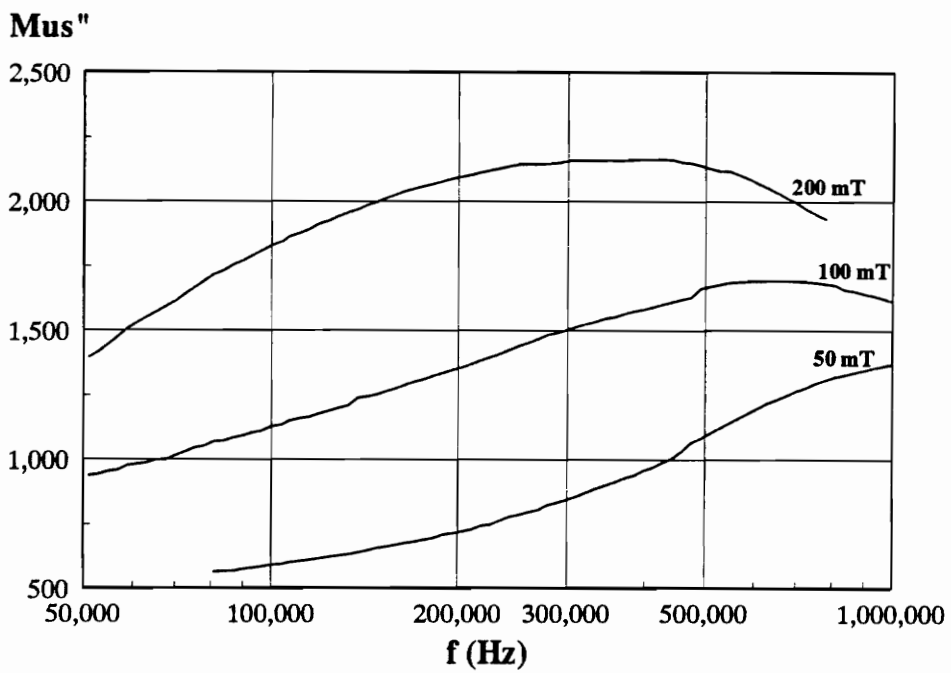
Fig. 3.9 The imaginary component of the series permeability measured from BE2#3a toroidal core at B_m = 50 mT, 100 mT and 200 mT, respectively.
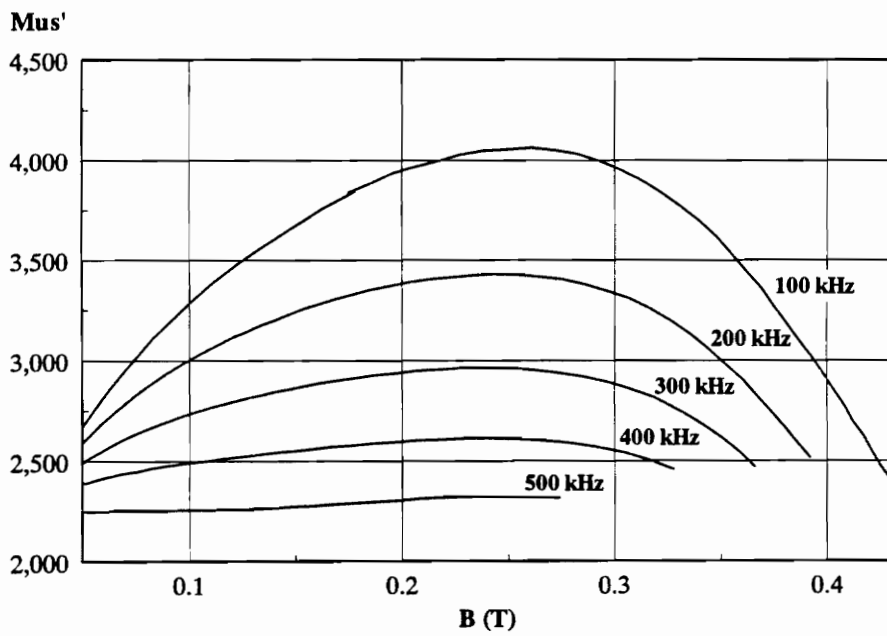
Fig. 3.10   The real component of the series permeability measured from BE2#3a toroidal core at f = 100 kHz, 200 kHz, 300 kHz, 400 kHz, and 500 kHz, respectively.
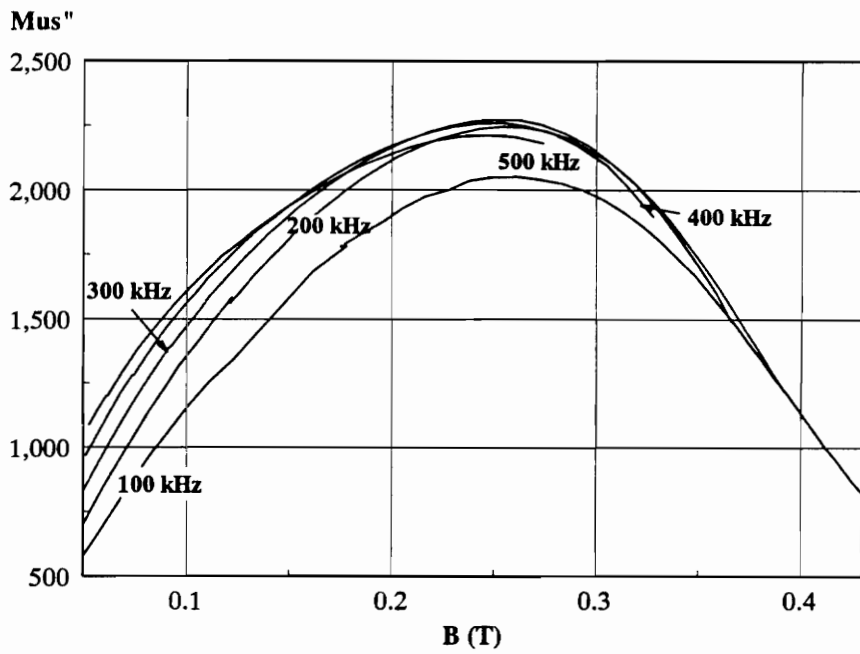
Fig. 3.8   The imaginary component of the series permeability measured from BE2#3a toroidal core at f = 100 kHz, 200 kHz, 300 kHz, 400 kHz, and 500 kHz, respectively.

3.1.2 Core Loss Measurements

In the previous section, only BE2 toroidal cores have been measured to collect the ferrite magnetic properties. This section will discuss the measurements of the core losses of a BE2 EI core and a BE2 RM10 core, respectively. It aims to use the measured core losses for comparison with the FEA results.

The setup used is the same as the one shown in Fig. 3.2. The non-uniform flux also exists in the EI core and the RM10 core. The effective dimensions (A_e, l_e, and V_e) are inevitably used to approximate the real cores with ideal cores with uniformly flux distributions. The approach of getting the effective dimensions is a little different from the approach mentioned in the previous section. The additional assumption here is that the permeability does not vary with the flux density in the same cross section under low field conditions[16]. The above approximation combined with Peterson's loss expression, yields relations for A_e and l_e for the cores which can be divided into k subsections, each subsection having a uniform cross-sectional area, A_i,

$$\frac{A_e}{l_e} = \sum_k \frac{l_i}{A_i},$$

(3.14)

$$\frac{l_e}{A_e^2} = \sum_k \frac{l_i}{A_i^2},$$

(3.15)

where l_i stands for the magnetic mean length in the i-th subsection of the core. From Eqs. (3.14) and (3.15), A_e and l_e can be obtained eventually. It should be mentioned that the assumption may be not theoretically sound, but it is practically useful [16].

For the one-port core loss measurement system, the accuracy of the sensed voltage is always lower than the two-port approach. In addition, its accuracy is also affected by using the effective dimension, A_e.

The geometry and core loss measured at 50 mT, 100 mT, and 200 mT of the EI core under test are shown in Fig. 3.9, and Fig. 3.10, respectively. The measured core losses of the RM10 ($A_e = 0.97$ cm^2 and $l_e = 4.61$ cm) at 50 mT and 100 mT are shown in Fig. 3.11 with one-turn winding.

The core loss measurements of the EI core and the RM10 core are performed at constant flux density. The fast testing ensures the temperature of 23 ~ 25°C.
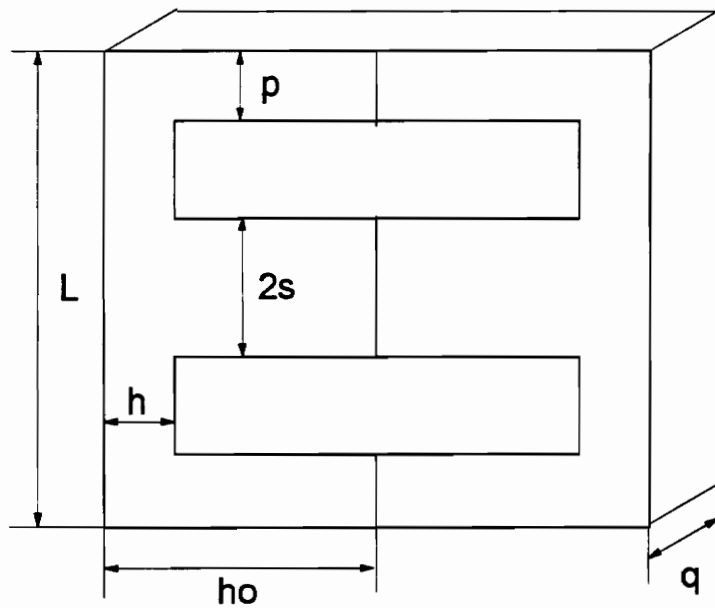
p = s = h = 4.96 mm, L = 40.12 mm,
ho = 15.99 mm, q = 10.08 mm

Fig. 3.9 Geometry of a BE2 EI core with A_e = 1.0165 cm^2 and l_e = 7.98 cm
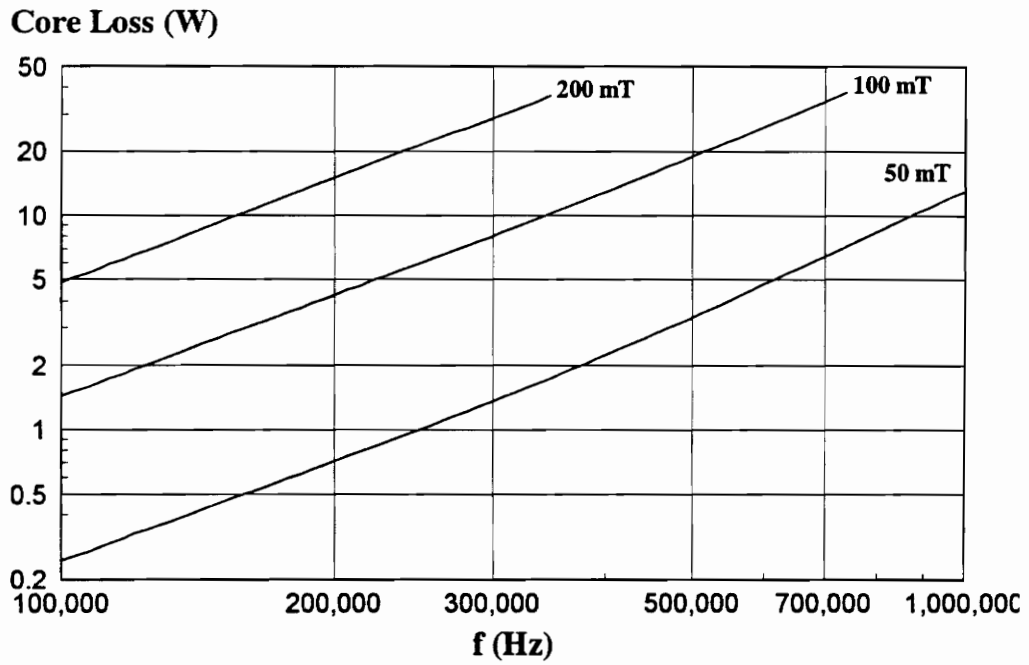
Core Loss (W)

Fig. 3.10 The measured core loss of the BE2 EI core shown in Fig. 3.9 with one-turn winding at B_m = 50 mT, 100 mT, and 200 mT, respectively.
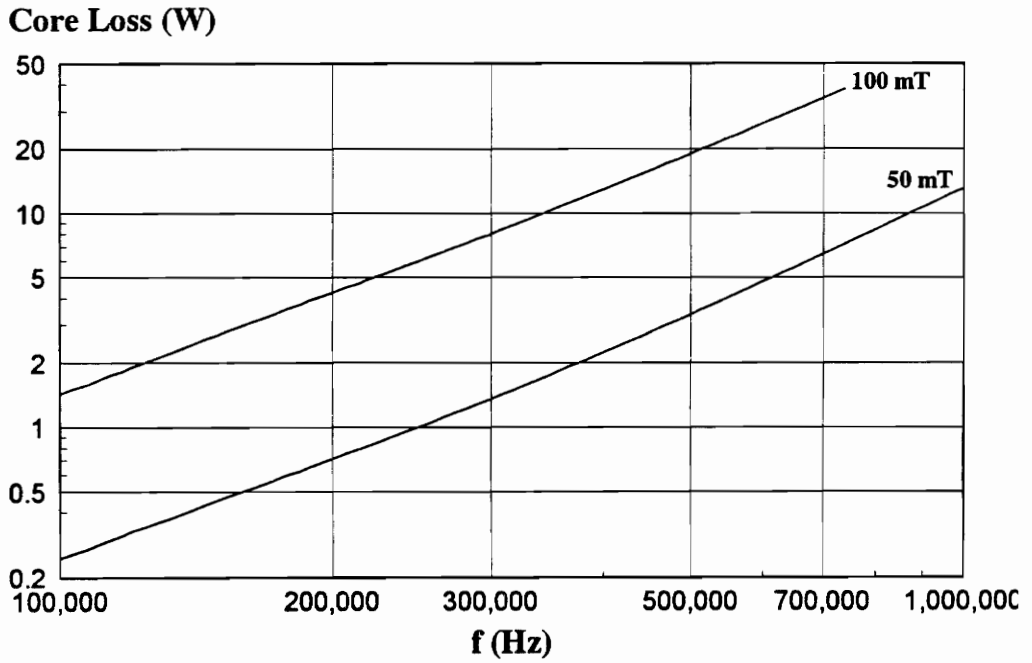
Core Loss (W)

Fig. 3.11 The measured core loss of a BE2 RM10 core with one-turn winding at B_m =50 mT and 100 mT, respectively.

3.2 Electrical Property Measurements

Ferrite materials are composed of highly conductive grains separated by low conductivity boundaries. A single grain (crystalline) with a boundary can be represented by a resistor and a loss-free capacitor in parallel, R_1-C_1, which represent the grain, in series with the other parallel elements, R_2-C_2, which represent the boundary, as shown in Fig. 3.12 [16]. σ_1 and σ_2 are the conductivity values of R_1 and R_2, respectively; ε_1 and ε_2 are the dielectric constants of C_1 and C_2, respectively. Practically, this equivalent circuit is also used to describe the polycrystalline structure of ferrites. At a specified frequency, this circuit can be simplified to a resistor, R_p, in parallel with a capacitor, C_p, as shown in Fig. 3.13. This simplified R_p-C_p parallel circuit can be also used at any frequency where R_p and C_p are functions of the frequency.

R_p and C_p have the following relations with the AC conductivity, σ_{AC}, and the relative dielectric constant, ε_r, respectively:

$$R_p = \frac{\sigma_{AC} t}{A}, \tag{3.16}$$

$$C_p = \varepsilon_r \varepsilon_0 \frac{A}{t}, \tag{3.17}$$

where t and A are the thickness and the cross-sectional area perpendicular to the current flow direction, respectively. Therefore, σ_{AC} and ε_r are functions of the frequency.
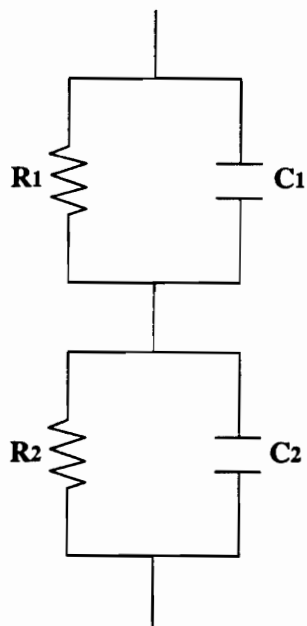
Fig. 3.12 The equivalent circuit model of a single grain in ferrites
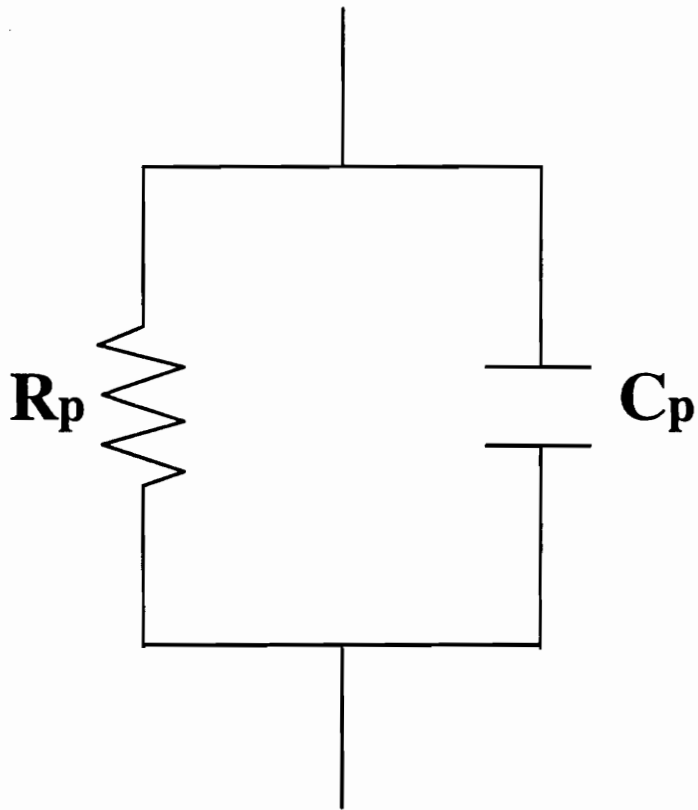
Fig. 3.13   The equivalent circuit of the bulk ferrite material

Valuable efforts have been made to understand the frequency dependence of conductivity and dielectric constant for ferrite materials [35,36,37,38]. This dependence has been explained on the basis of the microscopic structure of the ferrites. The measurement approaches have been developed. The present work requires the accurate acquisition of σ_{AC} and ε_r at different frequencies for MnZn ferrite materials because of the importance of this information for simulations. The HP 4194A impedance analyzer or the HP4192A LF impedance meter are used [35,37,39] to measure σ_{AC} and ε_r on toroidal samples. The toroid was sandwiched between two identical parallel electrodes to form an capacitor, as shown in Fig. 3.14. The authors either used silver Epoxy to glue the sample and parallel electrodes together, or used gold plated on the top and bottom surfaces of the sample as two parallel electrodes. The contact between electrodes and the sample is critical to the test accuracy. The use of gold-plated surfaces is more accurate and expensive than the use of Silver Epoxy.

In this work, the HP4194A impedance analyzer with an HP16451B dielectric test fixture is used to measure R_p and dissipation factor, D, directly on the disk-shaped BE2, as shown in Fig. 3.15.

The HP16451B dielectric test fixture could be hooked up directly to the unknown terminal of the HP4194A impedance analyzer to offer accurate measurements for R_p and D [39]. Such a fixture has four changeable guarded/guard electrodes, two of them contacting the sample directly over the entire plane, and the other two point-touching thin film electrodes which have been deposited on the sample. Our tests show that the former

**HP 4194A
Impedance
Analyzer**

**Parallel
Electrodes**

**Testing
Sample**
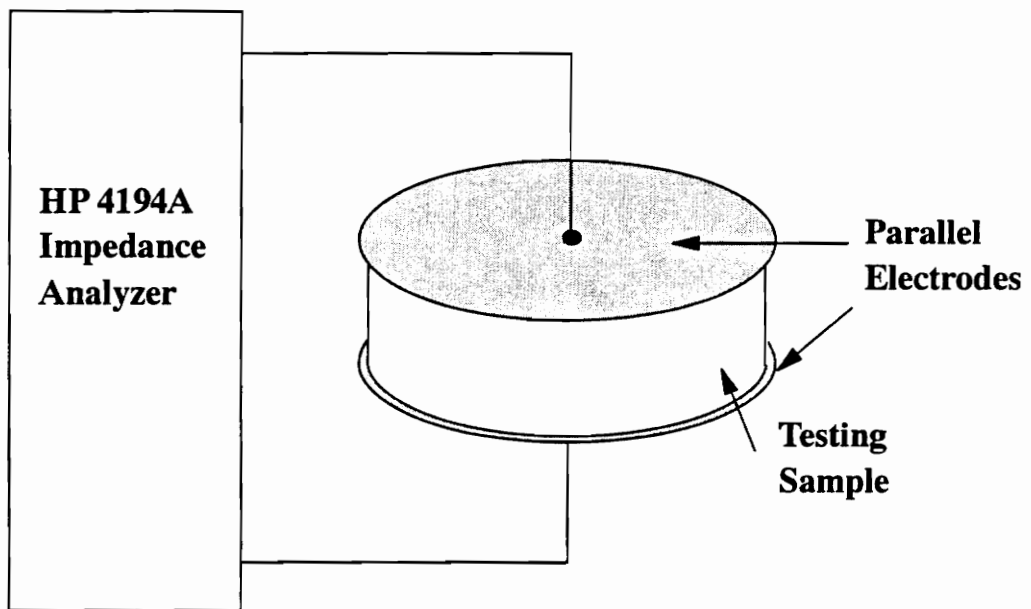
Fig. 3.14 Conductivity and dielectric constant measurement setup
using HP 4194A impedance analyzer
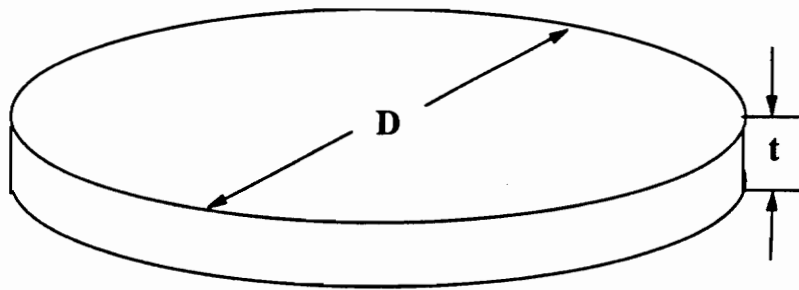
D = 14.94 mm   t = 3.00 mm

Fig. 3.15 Geometry of the BE2 disk-shaped sample for the conductivity and dielectric constant measurement

two electrodes do not work very well due to the gap between the electrodes and the sample. The electrode structure for the latter two types of electrodes is shown in Fig. 3.16. Using thin film electrodes is a good way to get rid of a big error source, the gap, and increase the test accuracy. The thin film can be metal foil, conductive paint, fired on silver, sprayed metal, evaporated metal, and metal spattering. Those techniques are not available in our lab. Especially making guarded/guard thin film electrodes requires high accuracy to ensure the isolation between them and make a perfect circle of guarded electrode. Practically, only two unguarded gold-plated thin-film electrodes are made in this research which have the same size as the cross section of the sample. Electrode C, whose inside diameter of guard electrode is bigger than the sample's, is selected as shown in Fig. 3.17. In other words, the function of guarded/guard electrodes is taken over by unguarded electrodes.

The edge capacitance which is shown in Fig. 3.18 cannot be eliminated. Since the thickness is smaller than the diameter of the sample, the edge capacitance can be neglected. After the measurements, dissipation factor, D, can be converted into C_p by

$$D = \frac{1}{2\pi f C_p R_p}.$$ (3.18)

Then conductivity and relative dielectric constant can be finally obtained based on Eqs. (3.16) and (3.17). The results of the dielectric constant and conductivity measurements are shown in Fig. 3.18 and Fig. 3.19 over 10 kHz ~ 1 MHz, respectively.
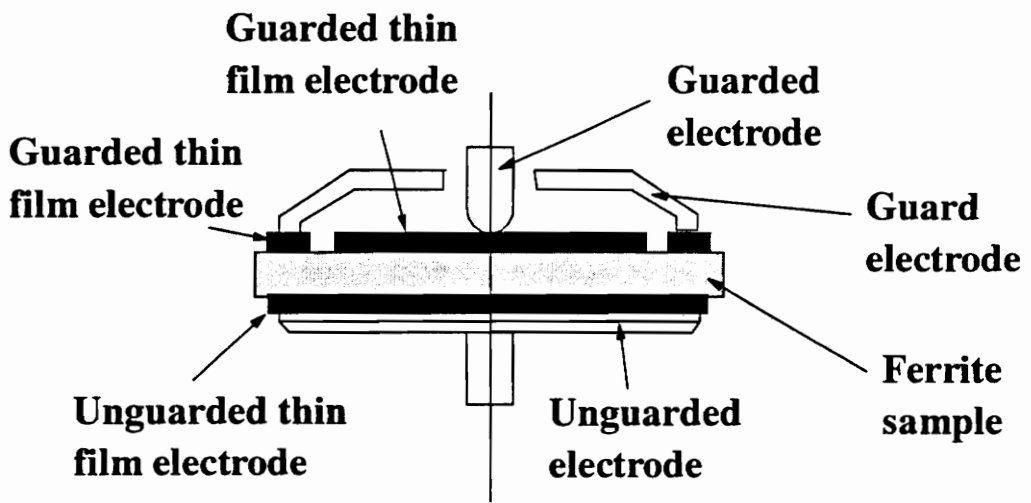
Fig. 3.16 Structure of HP16451B electrodes with thin-film electrodes
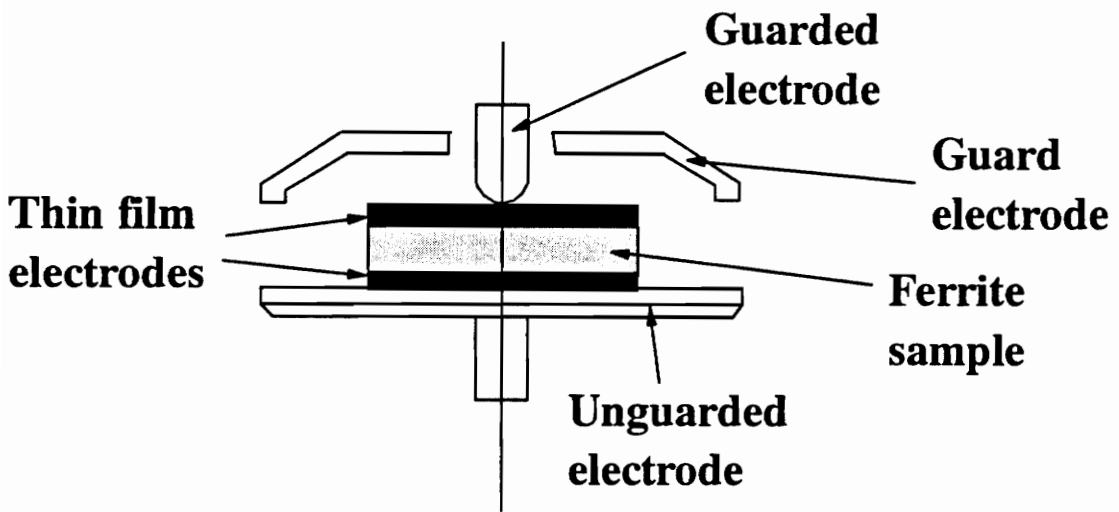
Fig. 3.17 The electrode structure of conductivity and
dielectric constant test used in this work
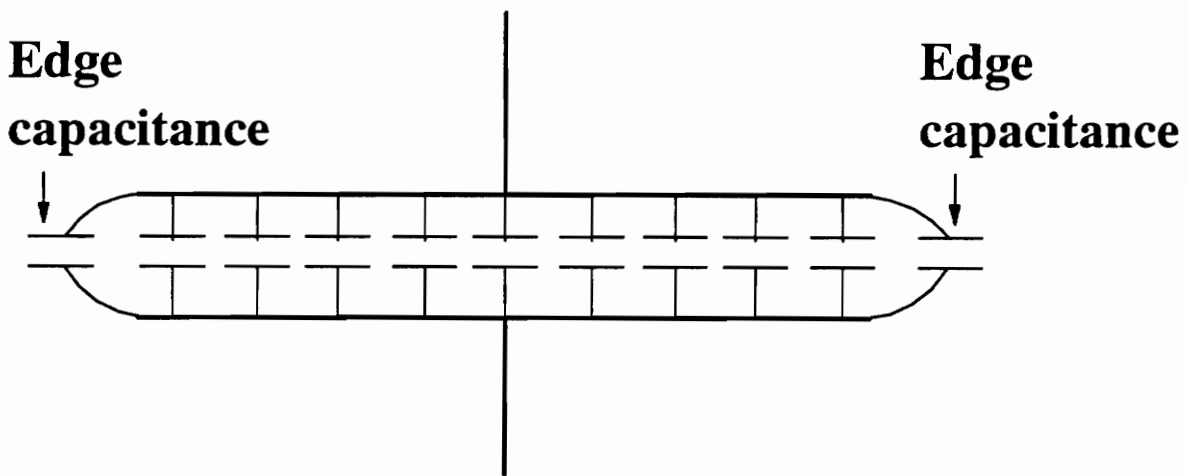
Fig. 3.18   A capacitor with edge effect

Relative dielectric constant
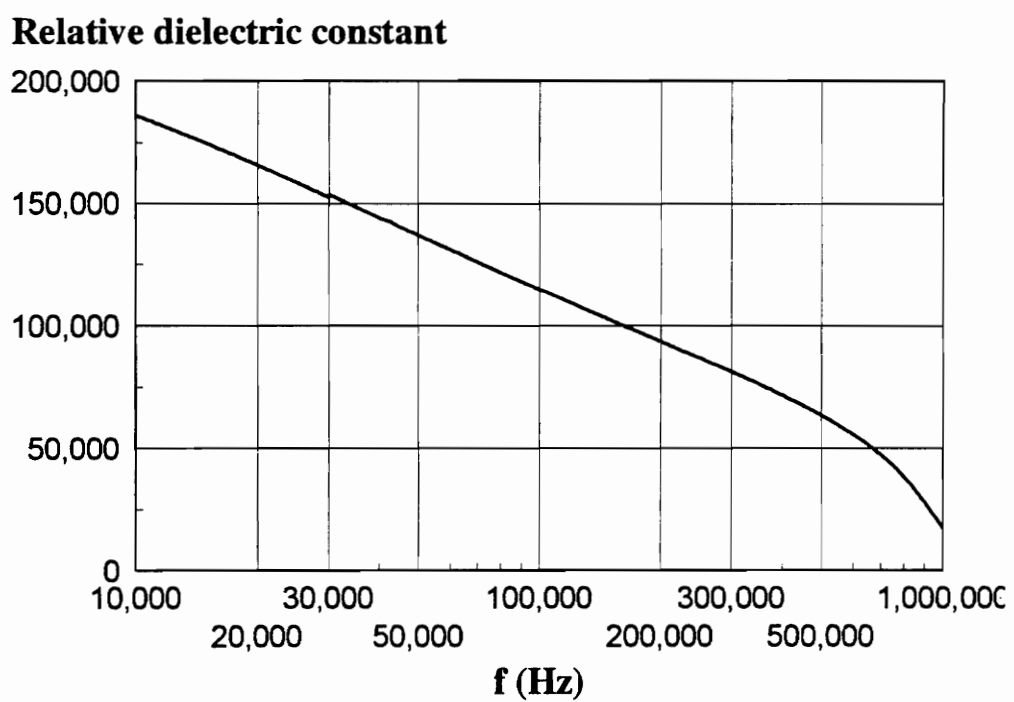
Fig. 3.19 Measured dielectric constant data on the BE2 disk sample
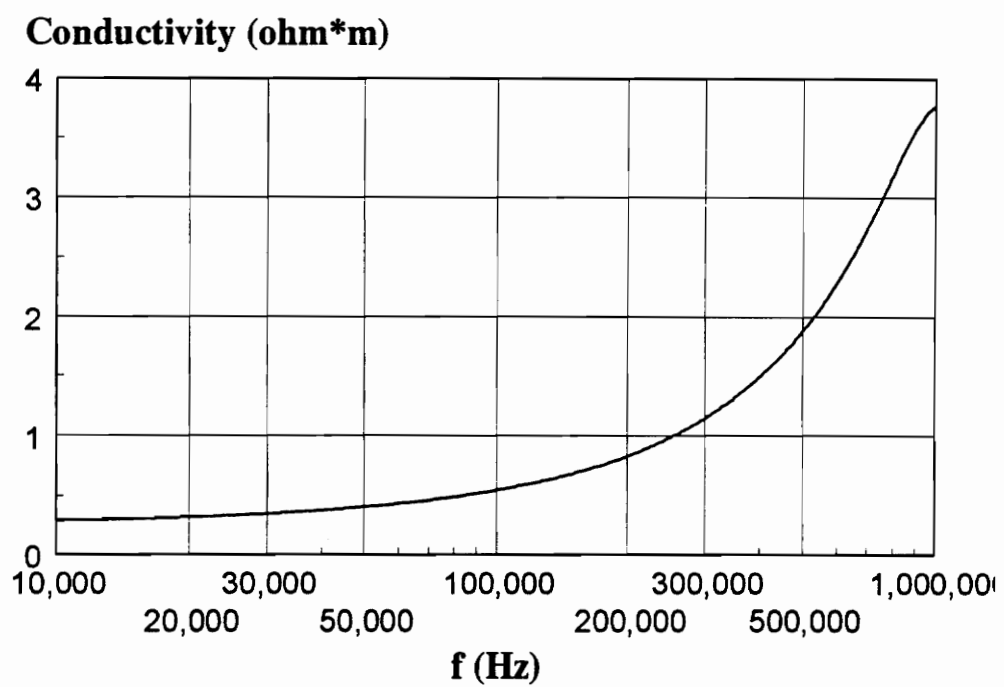
Conductivity (ohm*m)

Fig. 3.20 Measured conductivity data on the BE2 disk sample

4. Examples of Finite Element Simulations for Core Loss

The material data (the complex permeability, the AC conductivity, and the dielectric constant) required in the linear and sinusoidal excitation solver, Maxwell® have been measured in Chapter 3. This chapter will provide several simulation examples to demonstrate how to use the FEA solver to perform core loss analysis for ferrites and show the flux and the loss distributions.

4.1 Example 1: Core Loss Analysis of the Sample Toroidal Core

As the first example, BE2#2a thin toroid is simulated, and its core loss values at different operating conditions are calculated.

In order to save CUP time, Maxwell® 2D eddy current solvers are preferred. There are three types of 2D solvers: the eddy axial solver, the eddy axisymmetry solver, and the eddy field solver. The first type of solver is used to solve parallel conductor problems. It assumes that the object under study is infinitely long and the field is the same in any plane parallel to the x-y plane studied. Also, all the currents go into or out of the x-y plane normally, while the field has no normal components. For the toroid shown in Fig. 4.1, this solver is hard to use because the eddy current in the core circulates, and does not flow simply in Z direction. The second 2D solver is similar to the first one. The difference is that the object is not infinitely long in the z-direction, but axisymmetrical like pot cores. In other words, the first and the second solvers are simply used in different coordinates: xy and rz. It obviously cannot be used for the toroid. The last 2D solver is designed to solve eddy current problems of an infinitely long object. Flux is assumed to be perpendicular to the xy plane studied. Source currents disappear and are defined through boundary conditions of magnetic field intensity, H_{bound}. It seems a perfect 2D solver to examine the core loss in the toroid. For the toroid shown in Fig. 4.1, the core cross section in the yz plan can be taken as the 2D object studied, as shown in Fig. 4.2. The H values at the positions where the diameter equals ID and OD can be designated H_1 and H_2, respectively. The values at top and bottom lines of the core are described as H_3 and H_4, respectively. According to Ampere's law,

$$\oint H \cdot dl = Ni \qquad (4.1)$$

The boundary conditions are given by the following formulas:
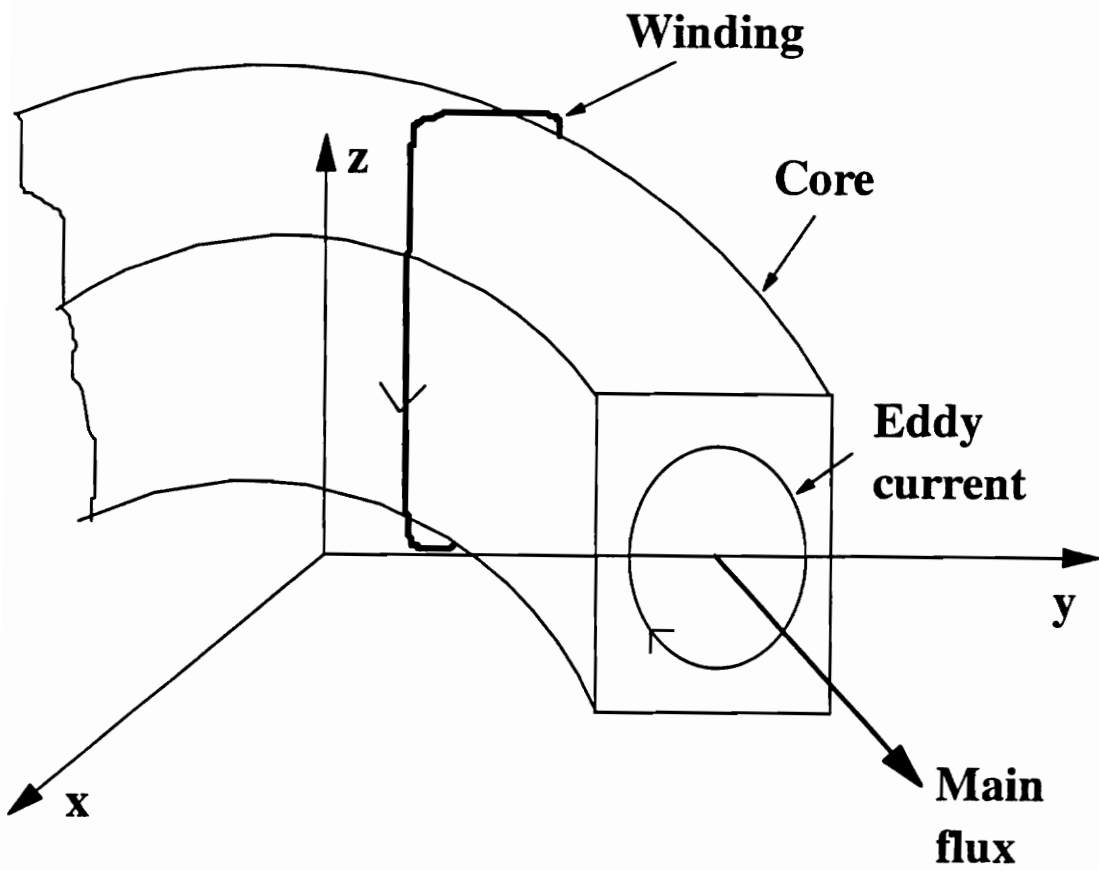
Fig. 4.1   Eddy current and flux in a toroidal core

$$H_1 = \frac{Ni}{\pi \cdot ID}$$

$$H_2 = \frac{Ni}{\pi \cdot OD} \qquad , \qquad (4.2)$$

$$H_3 = H_4 = \frac{Ni}{2 \cdot \pi \cdot x}$$

where x is the distance from any point on the H_3 or H_4 boundary to the axial line of the toroid. The excitation current, i, at certain frequency, f, and flux density, B, can be calculated from the excitation voltage, V (Eq. 3.7), and the impedance of the circuit, Z (Eqs. 3.4 ~ 3.6)

$$i = \frac{V}{Z} \qquad\qquad (4.3)$$

It is easy to see that the H values on the two boundaries, H_1 and H_2, are constant, but H values on the other two boundaries, H_3 and H_4, are functional. Right now, this solver cannot deal with functional boundary condition cases. If this function is available, the 2D solver will be a good tool to study core loss issues in toroids. The OD/ID ratio of BE2#2a thin toroid is 1.1. That means that the H values on the Boundaries, H_3 and H_4, can be approximately treated as constant. Under this assumption, this 2D eddy field solver can be utilized to simulate the loss in such thin toroid.

When the 2D solver is selected, the dielectric constant effect on the core loss calculations is primarily researched. In the 3D eddy current solver, the dielectric constant of any material is assumed to be unity. Therefore, examining the loss difference between using unity dielectric constant and using the dielectric constant measured at the frequency
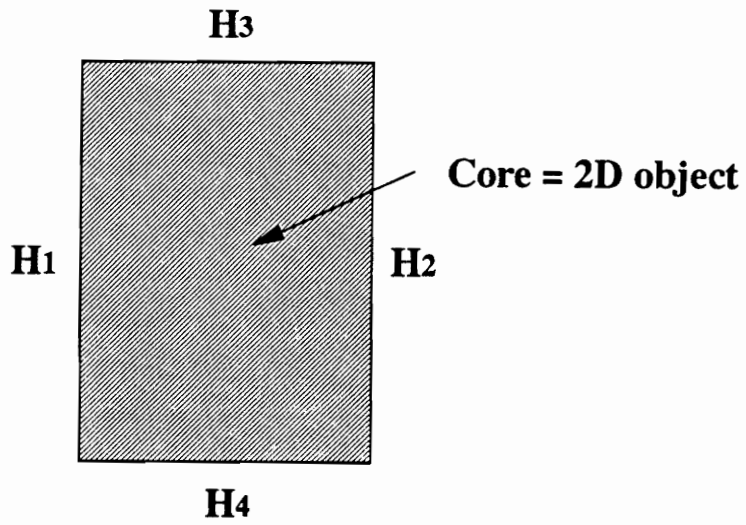
Fig. 4.2 Boundary conditions of 2D object of toroidal core used in 2D eddy field solver

of interest is helpful to evaluate the assumption made in the 3D solver. Table 4.1 gives the comparison results for the cases with both low and high values of flux density and frequency. It shows that loss differences due to these different settings for the dielectric constant are negligible. Even for the worst case here (case 4), the differences for both the eddy current loss and the hysteresis loss are less than 1%. So the assumption of unity dielectric constant in the 3D solver is adequate.

Table 4.1   The core loss comparison between taking dielectric constant as unity and its real value

	B (T)	f (kHz)	ε_{real}	$\varepsilon = 1$		$\varepsilon \neq 1$	
				P_h (W)	P_e (W)	P_h (W)	P_e (W)
case 1	.05	51	136865	6.05×10^{-3}	1.13×10^{-6}	6.05×10^{-3}	1.13×10^{-6}
case 2	.05	1000	17135	.608	4.06×10^{-3}	.610	4.07×10^{-3}
case 3	.2	51	136865	.108	1.81×10^{-5}	.108	1.81×10^{-5}
case 4	.2	702	47515	5.266	.024	5.283	.023

Simulations performed on BE2#3a toroid are done over 50 ~ 1000 kHz frequency range and under 50 mT, 100 mT, and 200 mT, respectively. Fig. 4.3 shows that the simulated core losses match the measurements well. The differences are within 5% range. It verifies that the FEA work well on the core with uniform flux distribution.
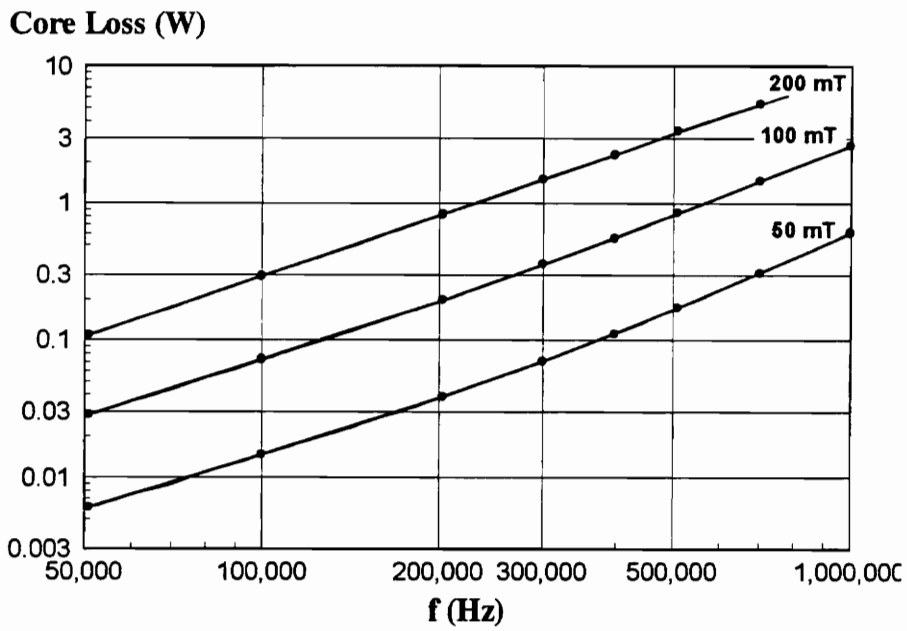
Core Loss (W)

Fig. 4.3   The core loss comparison between simulations and measurements for BE2 very thin sample
toroidal core (BE2#3a) with OD=19.96 mm, ID= 21.90 mm, and THK=4.96 mm,
where the solid lines and dots represent the measured and simulated core loss, respectively.

4.2 Example 2: Core Loss Analysis of an EI Core

This section concentrates on the simulations of the EI shown in Fig. 3.9. EI cores have simple geometry, similar to toroidal cores, but their flux distribution are more complex than toroids due to flux crowding at the corners.

Obviously, all the Maxwell® 2D solvers are not suitable for the loss analysis of the EI core. Therefore, 3D eddy current solver is used for the EI core simulation. The simulation region is reduced by using the symmetry of the geometry. In particular, only 1/8 of the EI is simulated (see Fig. 4.4). The symmetrical plane on the xz plane satisfies Dirichlet Condition; the other two symmetrical planes on the xy and yz planes, respectively, satisfy Neumman conditions.

In the first case simulated, the 1/8 EI core is excited by a 400 kHz and 1.06A sine wave of current that results in 100 mT flux density. From laboratory measurements, the material data under this condition are $\overline{\mu} = 2528 - j1584$, $\sigma = 1.485\ (s/m)$. The simulated and measured core loss for this condition can be found in Table 4.2. Table 4.2 shows that simulation result of total core loss is greater than the measurement by 8%.

Table 4.2   The simulation and measurement results of the core loss in the EI core for B_m = 100 mT and f = 400 kHz

$P_{h\_simulation}$ (W)	$P_{e\_simulation}$ (W)	$P_{total\_simulation}$ (W)	$P_{total\_measured}$ (W)	Difference
13.56	.59	14.15	13.02	8%
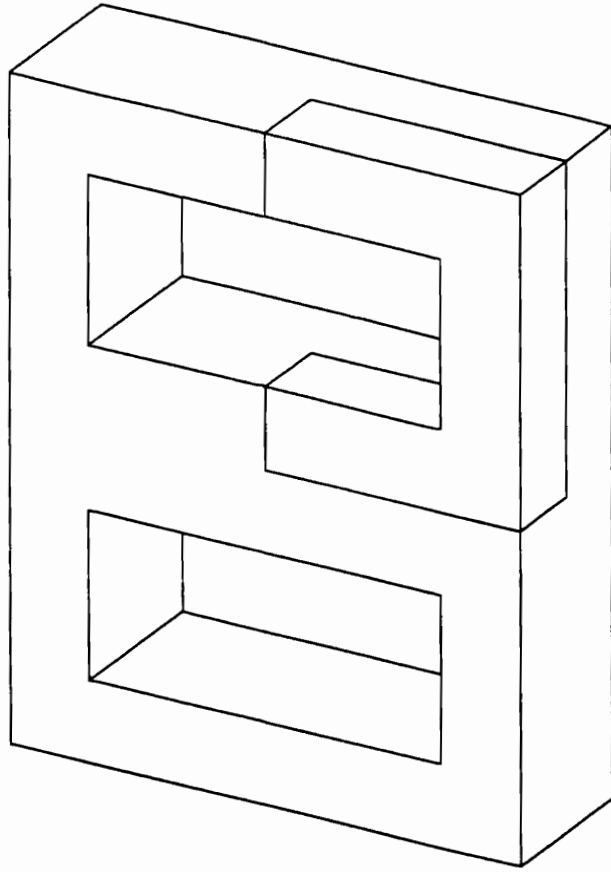
Fig. 4.4   The whole EI core and 1/8 of the EI under simulation

This solver uses a constant value of permeability for the entire EI core which means that flux is uniformly distributed in the core. However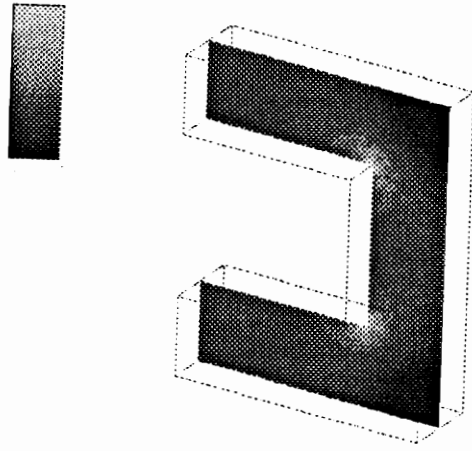, the nonuniform flux distribution on a cut-plane, which is parallel to the yz plane and cuts through the 1/8 EI core, is plotted in Fig. 4.5. It shows that the flux concentrates at the inside corners and becomes very low at the outside corners. In order to quantify the flux density variation, the flux density distribution is plotted in Fig. 4.6 along the line from the inside corner to the outside corner on the previous cut-plane. Finally, the core is divided into several parts: the inner corners, the outer corners and the main part. Then the piecewise EI core is simulated again by using the average flux density and the respective permeability values in each part given in Table 4.3. It is found that the maximum loss density value at the inner corners increases to 2660 mW/cm³, while the value obtained by using uniform permeability is only 2100 mW/cm³. Table 4.4, however, shows the calculated core is only 0.5% higher than one obtained by using constant permeability in the entire core. This phenomenon can be explained. Although the flux density reaches up to .2 mT at the inner corner, the volumes of the respective regions are so small that the localized high loss will not have evident effects on the total loss in the core. Although the volume of the core at the outer corner regions with 0 ~ 0.05 mT is not so small, the loss in those regions is relatively small due to their low flux density. The loss error resulting from inaccurate permeability value will not be critical, either. In addition, the underestimated loss at the inner corner will be compensated by the overestimated loss at the outer corner to some degree. Therefore, the piecewise approach is not necessary in the simulations if the total loss is considered.

Fig. 4.5 The nonuniform flux distribution on a cut-plane of the EI core, which is parallel to the yz plane and cut through the 1/8 EI core
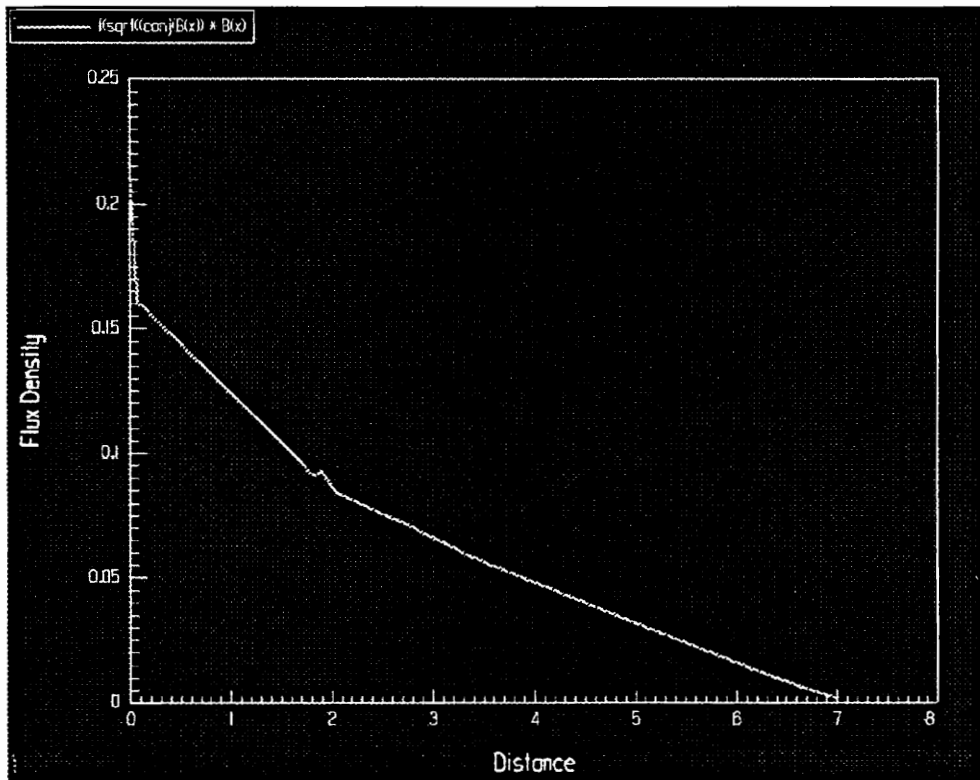
Fig. 4.6 The flux density line-plot of the EI core from the inside corner to the outside corner on the same cut-plane as used in Fig. 4.5

Table 4.3 The average flux density and the complex permeability in the inner corner, outer corner, and main part of the EI core at 400 kHz and 100 mT

	Inner corner	Outer corner	main part
Average flux density (T)	.18	.1	.025
Complex permeability	2580-j2100	2528-j1584	2215-j475

Table 4.4 The core loss comparisons between computations assuming constant flux density in the entire EI core (Approach I) and those using piecewise constant permeability approach (Approach II) for f = 400 kHz and B_m = 100 mT case

Approach I			Approach II			Total Loss
P_h (W)	P_e (W)	P_{total} (W)	P_h (W)	P_e (W)	P_{total} (W)	Difference
14.74	.78	15.52	14.82	.78	15.60	0.5 %

Fig. 4.7 shows the eddy current loss, the hysteresis loss, and the total loss distributions on the same cut-plane. It is easy to find that the hot spots are located at the inside corners. Simulations of the EI core are also performed at several flux density and frequency conditions. Figure 4.8 shows the calculated and measured core losses. The simulation results are higher than the measurements by about 25%. Since the effective dimensions, A_e and l_e, are not defined on a strong theoretical basis as explained in Chapter 3, the measurements which use those dimensions may be off from the real loss values.
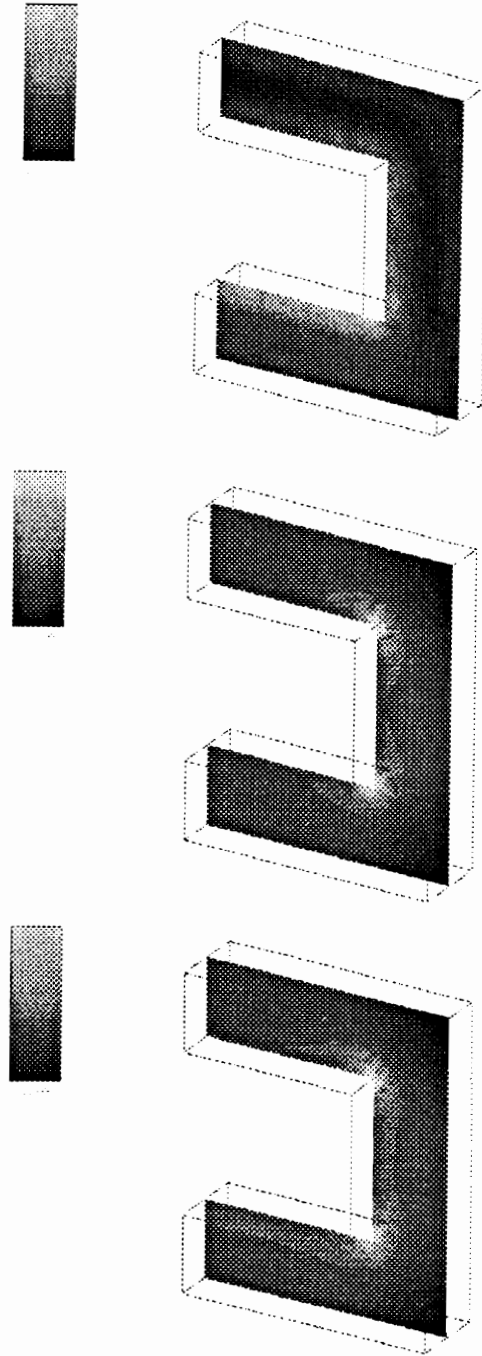
Fig. 4.7 The eddy current loss, the hysteresis loss, and the total core loss distributions on the same cut-plane of the EI core as used in Fig. 4.5 at 400 kHz and 100 mT flux density condition

Core Loss (W)
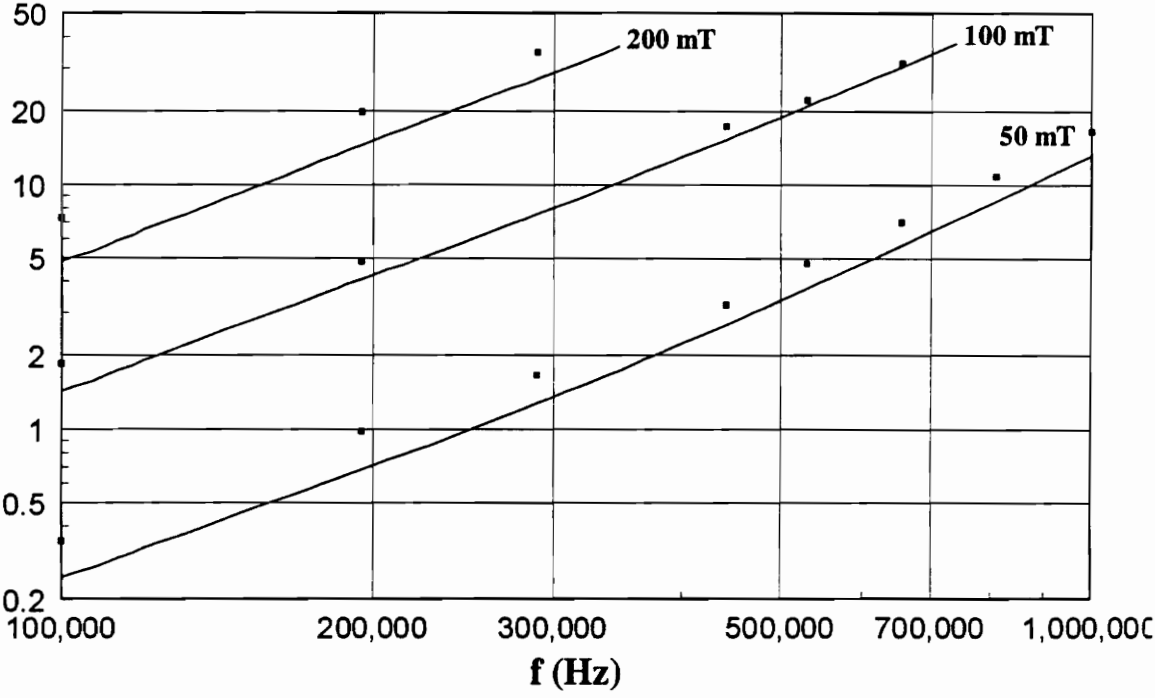
Fig. 4.8   The core loss comparison between simulations and measurements for the BE2 EI core shown in Fig. 3.9, where dots are the simulation results and solid lines are the measurement results

4.3 Example 3: Core Loss Analysis of an RM10 Core

RM cores have more complex geometry than EI cores. This section will show how to simulate RM cores by selecting a BE2 RM10 core and using the 3D eddy current solver. Fig. 4.9 shows the entire RM10 core and the 1/8 of the core under simulation. The simulated losses are compared with the measurements under the constant permeability assumption in Fig. 4.10. There are good agreements between the measured and simulated results. The differences are about 15%. The effective dimensions still have some effects on the measurements. Finally, the flux, the eddy current loss, the hysteresis loss, and the total core loss distributions are shown qualitatively (Fig. 4.11 ~ Fig. 4.15) and quantitatively (Fig. 4.16 ~ Fig. 4.19). The hot spots are identified easily from the visual field or the loss distributions. They are located right at the intersections between the inside corners and the yz plane.

The RM10 core simulations are very time-consuming and require rather powerful computer resources due to the greatly uneven flux distribution. The accuracy of simulations highly rely on the fineness of the mesh to some degree.
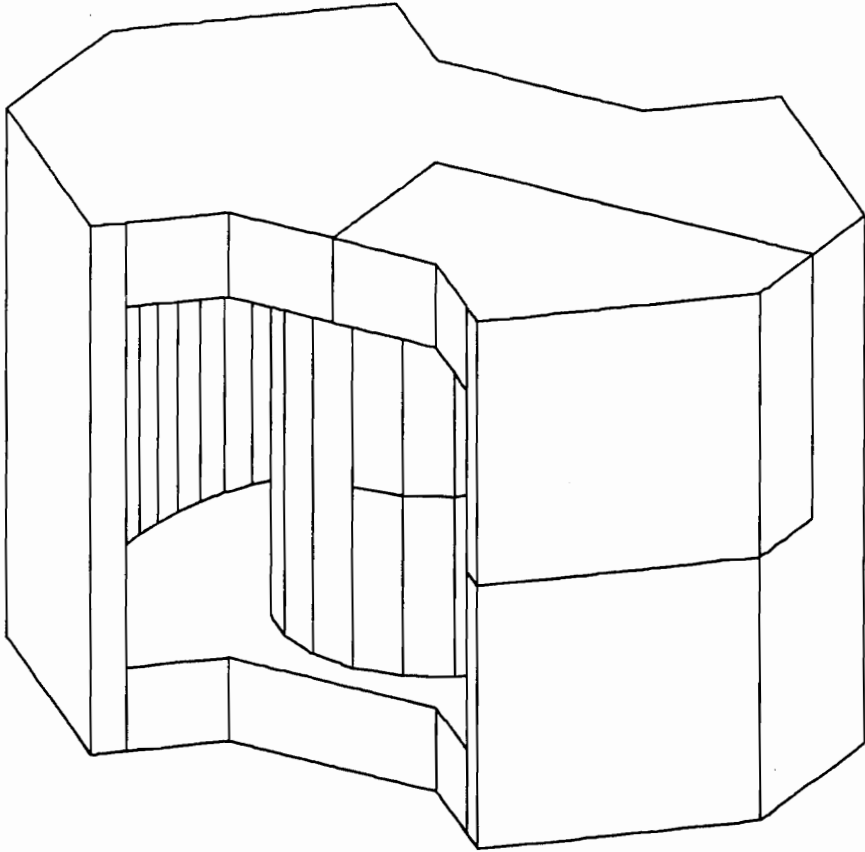
Fig. 4.9 The entire RM10 core and 1/8 core under simulation
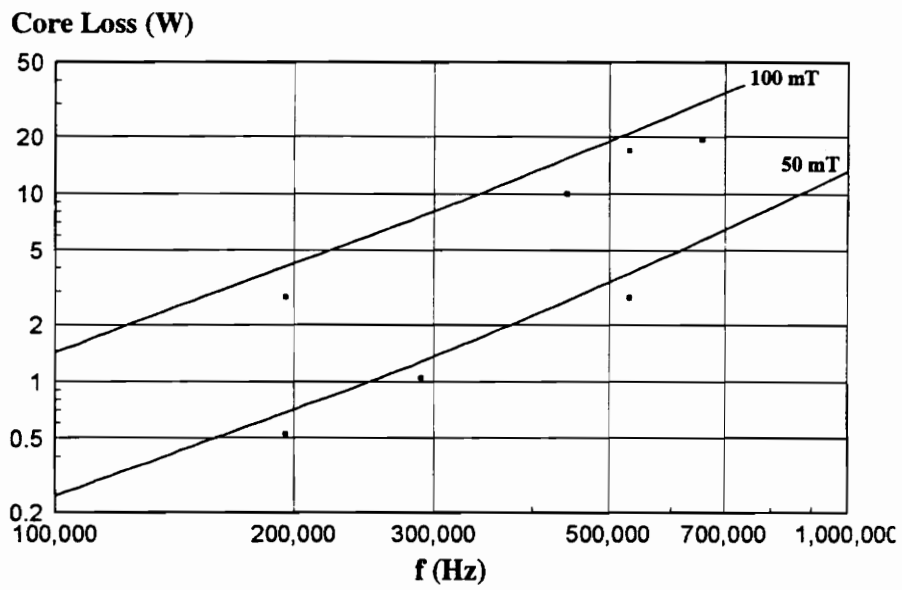
Fig. 4.10 The core loss comparison between simulations and measurements for the BE2 RM10 core, where dots are simulations and solid lines are measurements
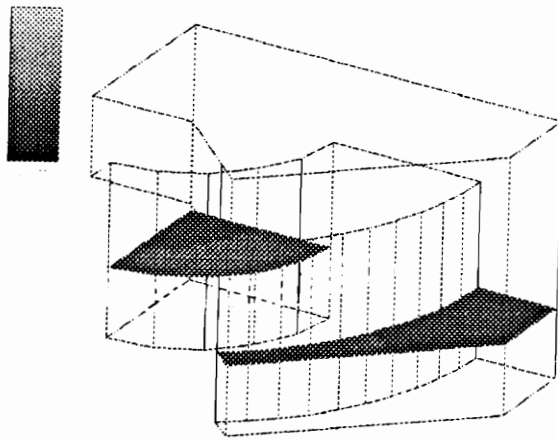
(a)
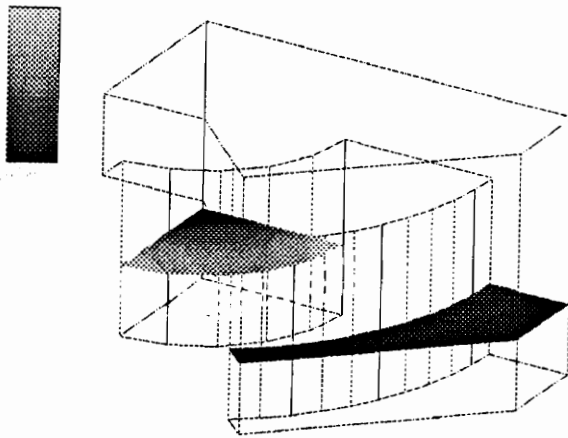
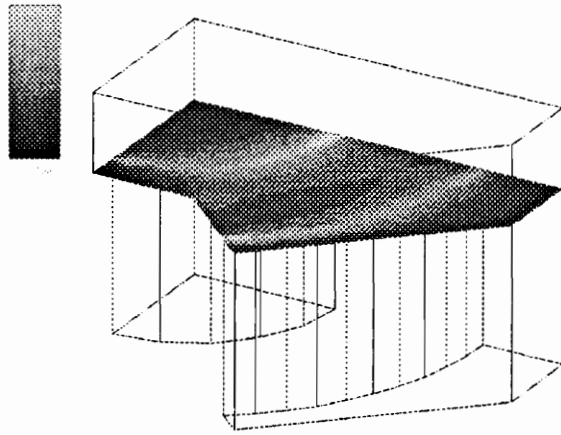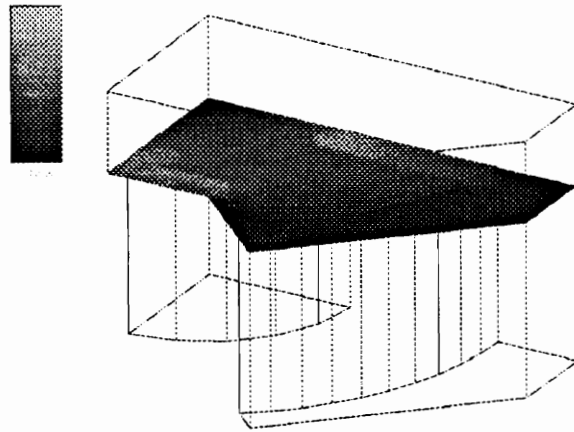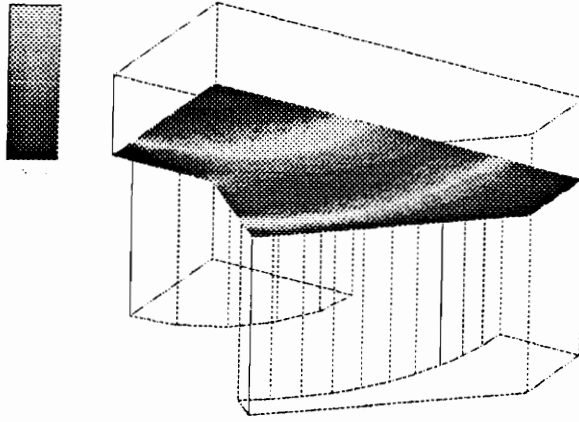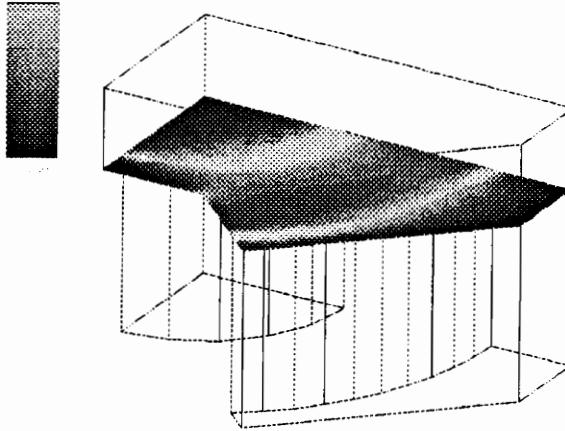
(b)

Fig. 4.11   The flux, the eddy current loss, the hysteresis loss, and the total core loss distributions on the plane which is parallel to and .1″ above the xy plane
(a)   the flux distribution in the centerpost and the leg: relatively uniform
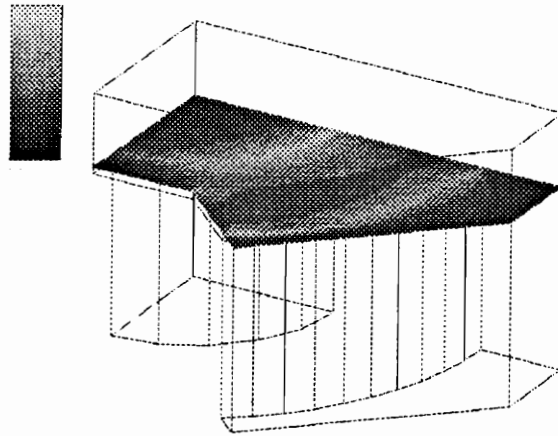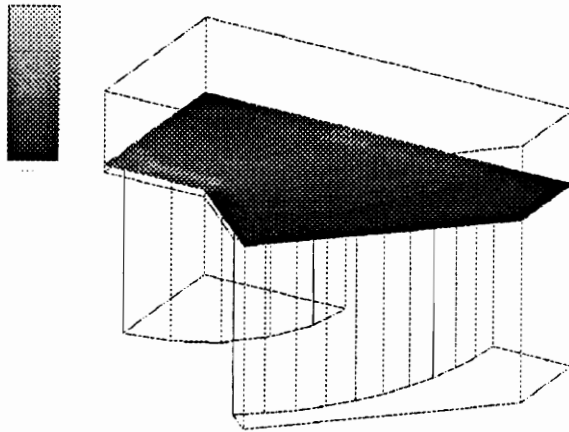(b)   the eddy current loss distribution in the centerpost and the leg
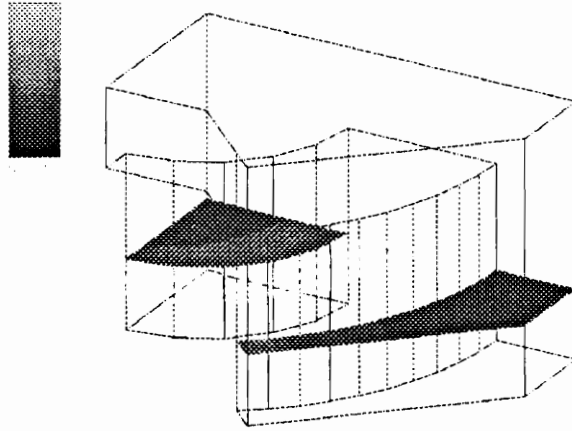
(c)
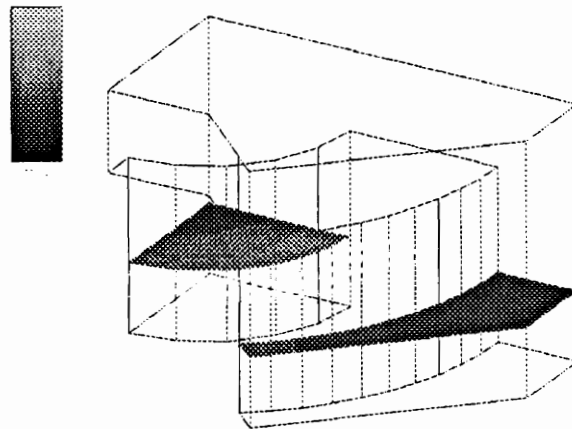
(d)

Fig. 4.11 The flux, the eddy current loss, the hysteresis loss, and the total core loss distributions on the plane which is parallel to and .1″ above the xy plane

(c)   the hysteresis loss distribution in the centerpost and the leg: relatively uniform

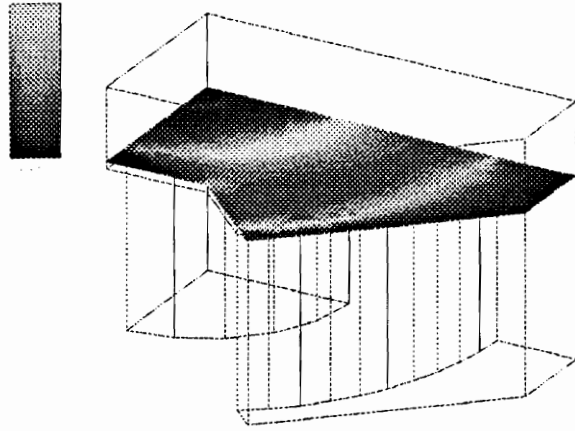(d)   the total loss distribution in the centerpost and the leg
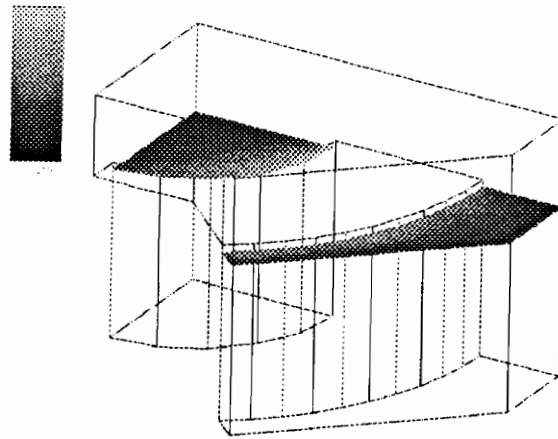
(a)
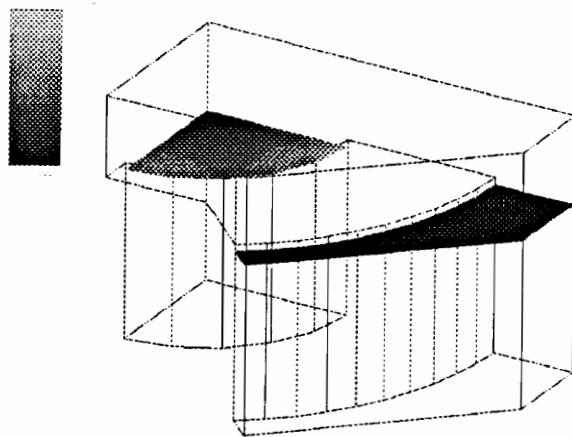
(b)

Fig. 4.12 The flux, the eddy current loss, the hysteresis loss, and the total core loss distributions on the plane which is parallel to the xy plane and .01″ below the bottom of the top plate

(a)   the flux distribution in the centerpost and the leg: flux concentrates at the corners

(b)   the eddy current loss distribution in the centerpost and the leg: evident skin effect
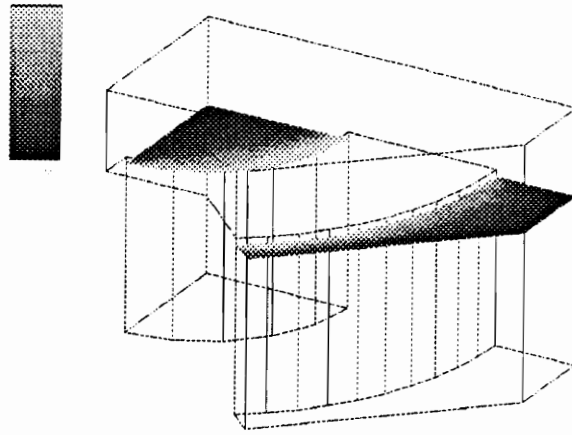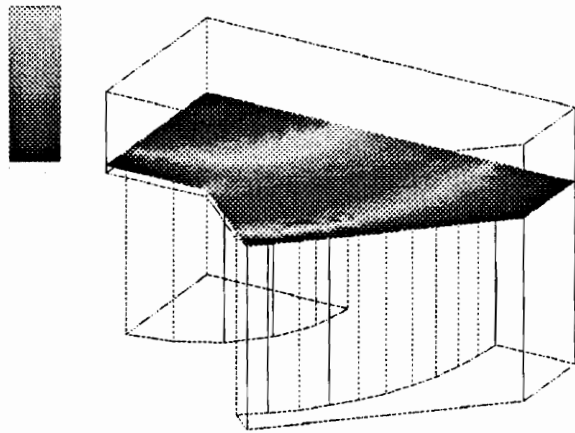
(c)
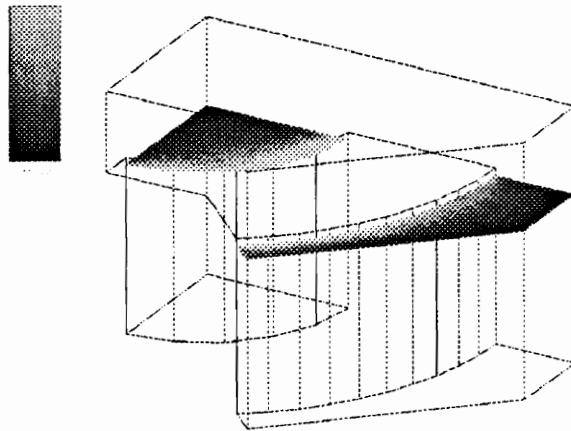
(d)

Fig. 4.12   The flux, the eddy current loss, the hysteresis loss, and the total core loss distributions on the plane which is parallel to the xy plane and .01″ below the bottom of the top plate

(c)   the hysteresis loss distribution in the centerpost and the leg: loss concentrates at the corners

(d)   the total loss distribution in the centerpost and the leg
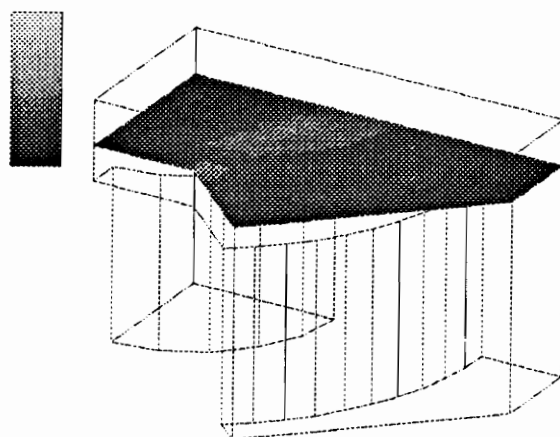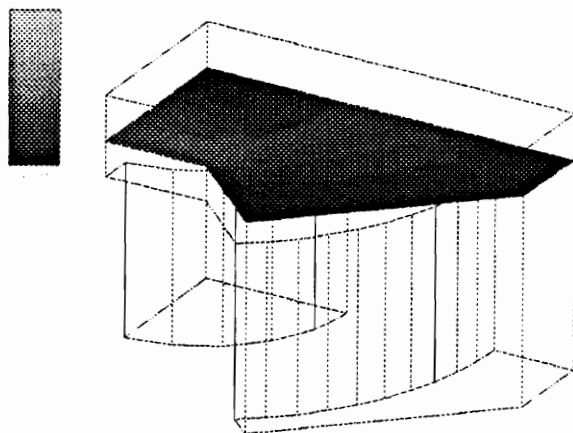
(a)

(b)

Fig. 4.13   The flux, the eddy current loss, the hysteresis loss, and the total core loss distributions on the plane which is parallel to the xy plane and right at the bottom of the top plate

(a)   the flux distribution in the centerpost, the top plate, and the leg: flux concentrates at the corners

(b)   the eddy current loss distribution in the centerpost, the top plate, and the leg

(c)

(d)

Fig. 4.13 The flux, the eddy current loss, the hysteresis loss, and the total core loss distributions on the
plane which is parallel to the xy plane and right at the bottom of the top plate
(c)   the hysteresis loss distribution in the centerpost, the top plate, and the leg
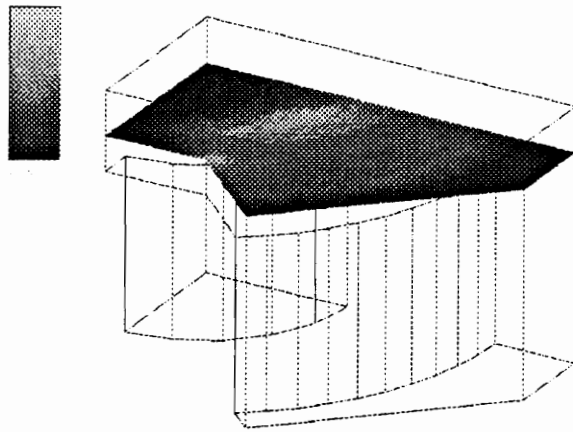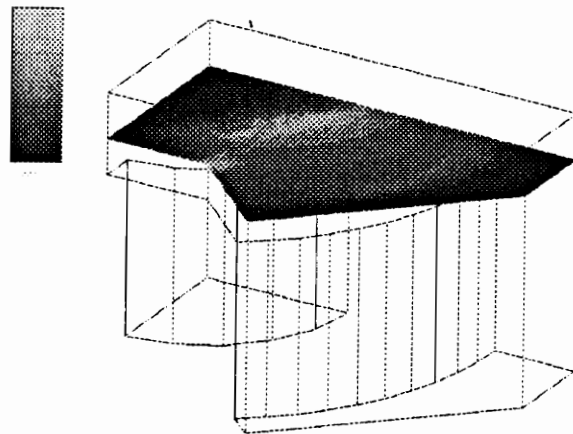(d)   the total loss distribution in the centerpost, the top plate, and the leg

(a)

(b)

Fig. 4.14 The flux, the eddy current loss, the hysteresis loss, and the total core loss distributions on the plane which is parallel to the xy plane and .01″ above the bottom of the top plate

(a)   the flux distribution in the centerpost, the top plate, and the leg

(b)   the eddy current loss distribution in the centerpost, the top plate, and the leg

(c)

(d)

Fig. 4.14 The flux, the eddy current loss, the hysteresis loss, and the total core loss distributions on the plane which is parallel to the xy plane and .01″ above the bottom of the top plate
(c)   the hysteresis loss distribution in the centerpost, the top plate, and the leg
(d)   the total loss distribution in the centerpost, the top plate, and the leg

Examples of Finite Element Simulations for Core Loss   81

(a)

(b)

Fig. 4.15 The flux, the eddy current loss, the hysteresis loss, and the total core loss distributions on the plane which is parallel to the xy plane and .05″ above the bottom of the top plate
      (a)   the flux distribution in the centerpost, the top plate, and the leg
      (b)   the eddy current loss distribution in the centerpost, the top plate, and the leg

(c)

(d)

Fig. 4.15   The flux, the eddy current loss, the hysteresis loss, and the total core loss distributions on the plane which is parallel to the xy plane and .05″ above the bottom of the top plate

    (c)   the hysteresis loss distribution in the centerpost, the top plate, and the leg

    (d)   the total loss distribution in the centerpost, the top plate, and the leg

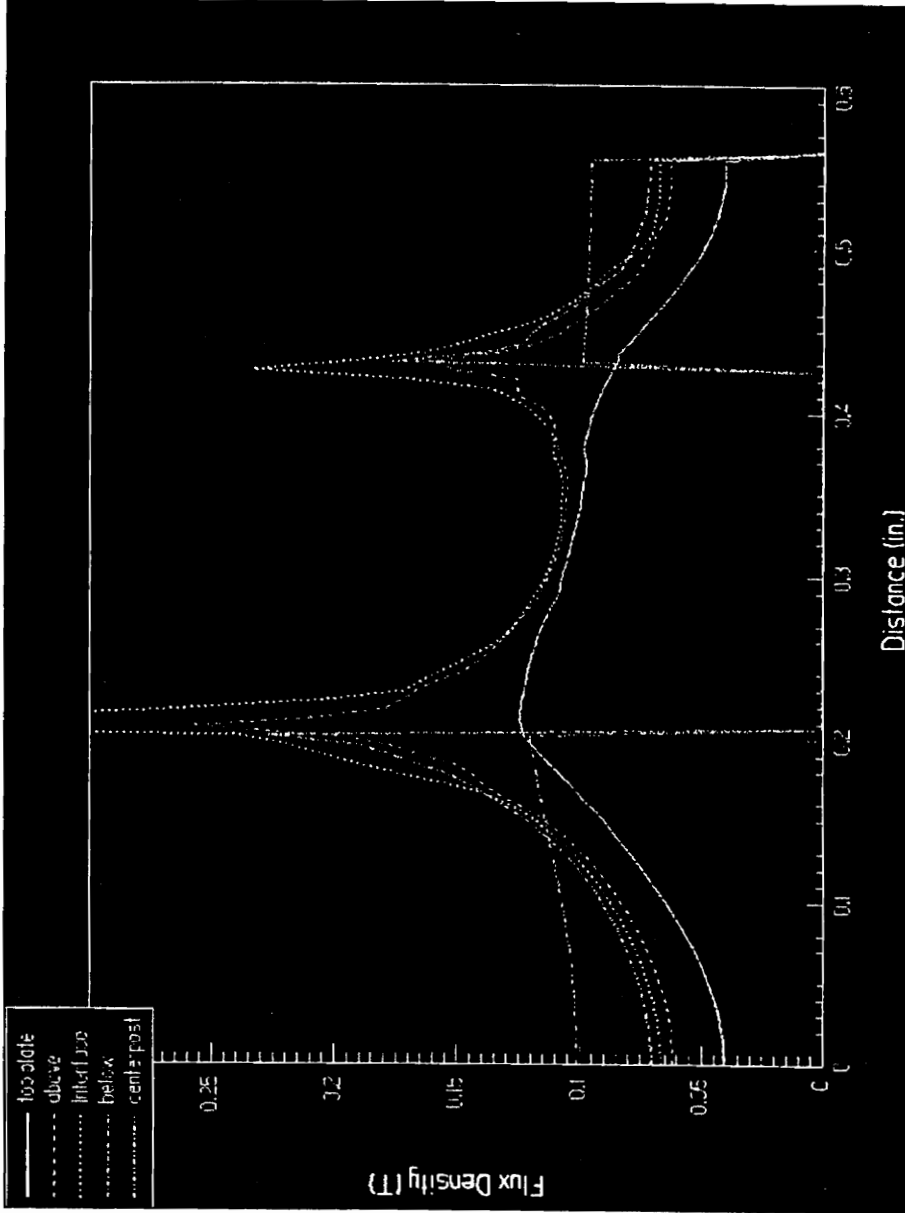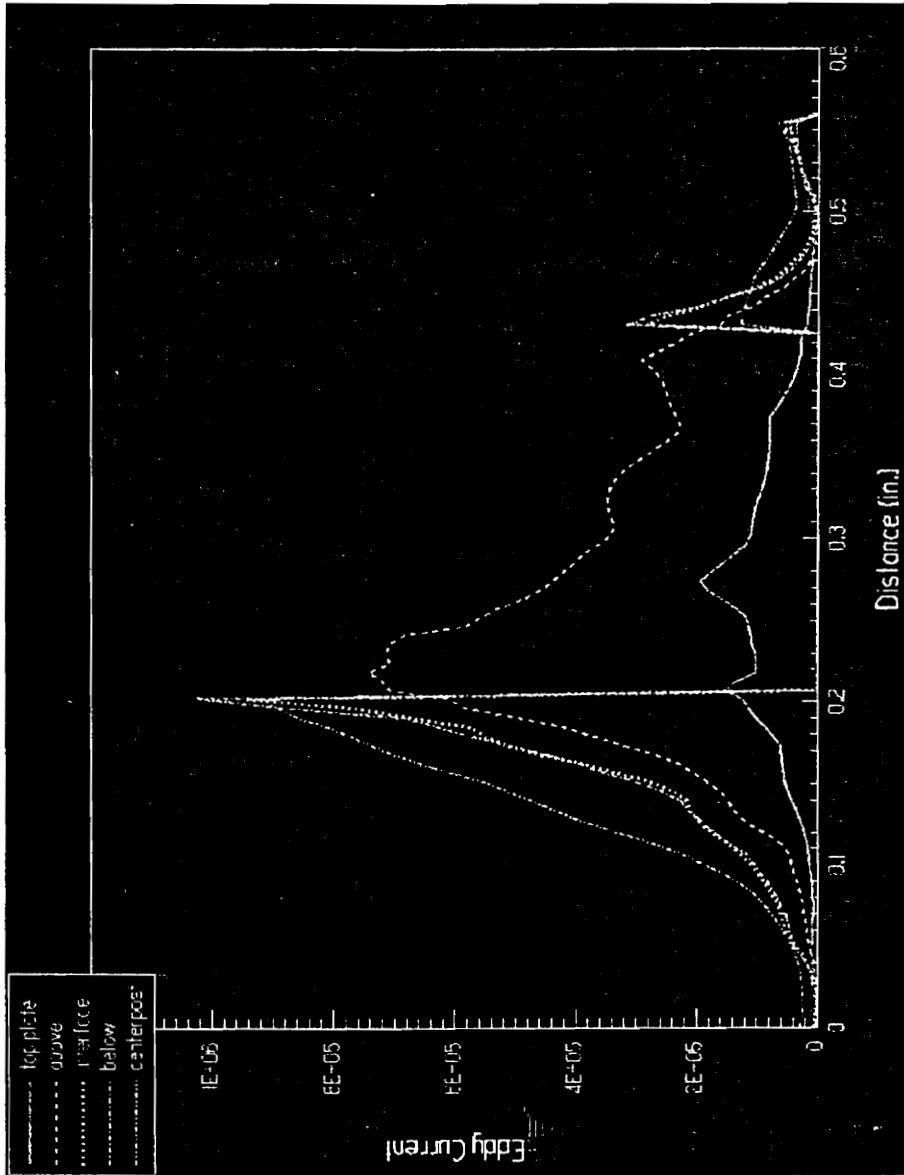**Examples of Finite Element Simulations for Core Loss**
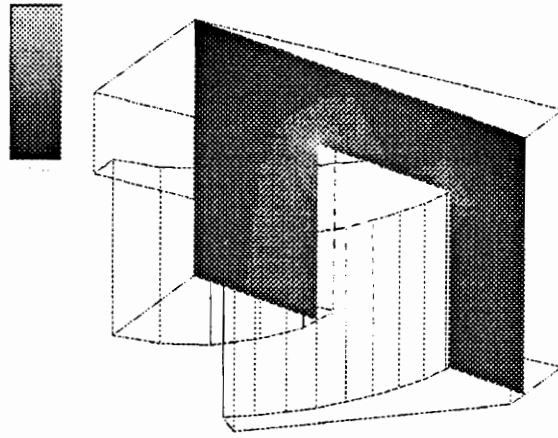
Fig. 4.16   The flux distribution on a vertical plane which has 10° angle with the yz plane, and the flux, the eddy current loss, the hysteresis loss, and the total core loss distributions on a set of horizontal lines which are the intersections of this plane and the five horizontal planes used in Fig. 4.11 ~ 4.15.

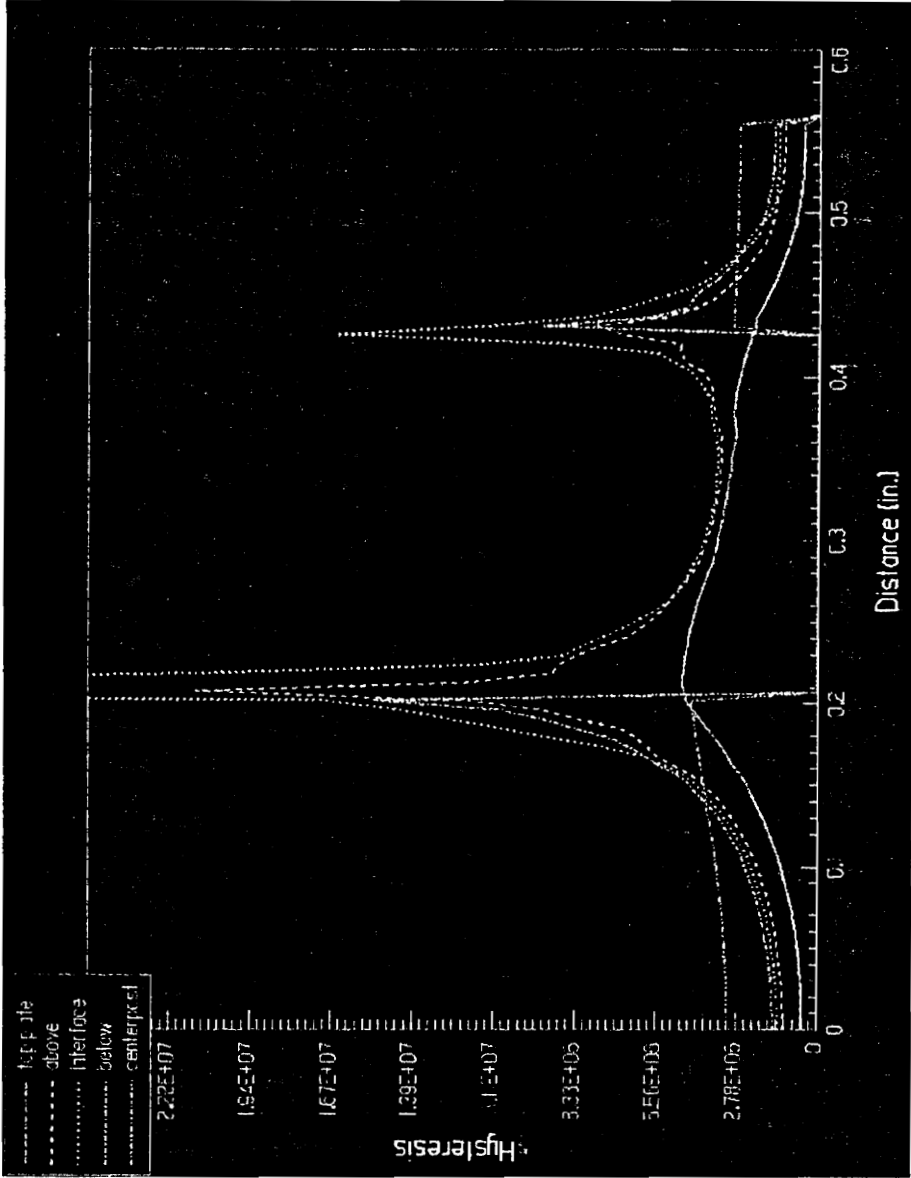(a)   the flux distribution on the vertical plane

Fig. 4.16 The flux distribution on a vertical plane which has 10° angle with the yz plane, and the flux, the eddy current loss, the hysteresis loss, and the total core loss distributions on a set of horizontal lines which are the intersections of this plane and the 5 horizontal planes used in Fig. 4.11 ~ 4.15.

(b) the flux distribution on the lines

Fig. 4.16   The flux distribution on a vertical plane which has 10° angle with the yz plane, and the flux, the eddy current loss, the hysteresis loss, and the total core loss distributions on a set of horizontal lines which are the intersections of this plane and the 5 horizontal planes used in Fig. 4.11 ~ 4.15.

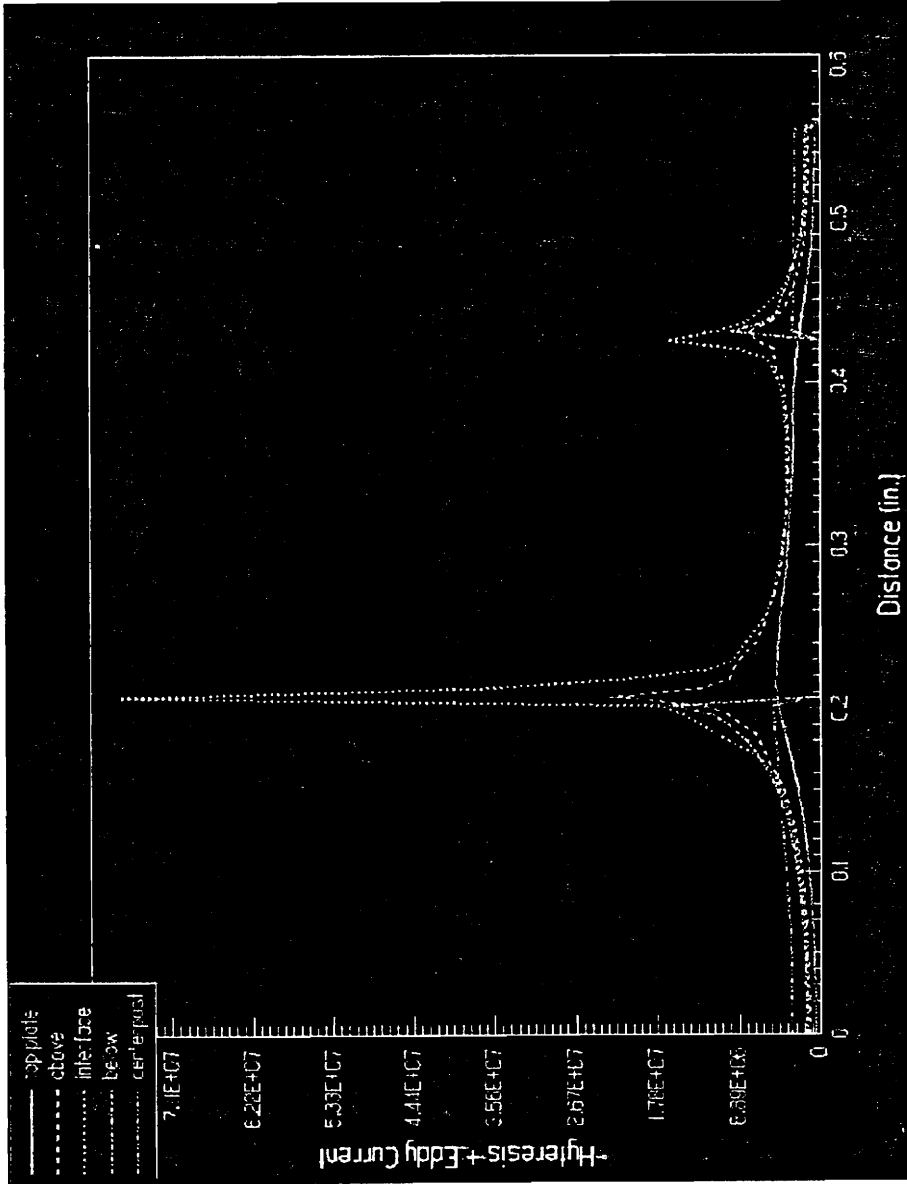(c)   the eddy current loss distribution on the lines

Fig. 4.16 The flux distribution on a vertical plane which has 10° angle with the yz plane, and the flux, the eddy current loss, the hysteresis loss, and the total core loss distributions on a set of horizontal lines which are the intersections of this plane and the 5 horizontal planes used in Fig. 4.11 ~ 4.15.
(d)   the hysteresis loss distribution on the lines

Fig. 4.16   The flux distribution on a vertical plane which has 10° angle with the yz plane, and the flux, the eddy current loss, the hysteresis loss, and the total core loss distributions on a set of horizontal lines which are the intersections of this plane and the 5 horizontal planes used in Fig. 4.11 ~ 4.15.

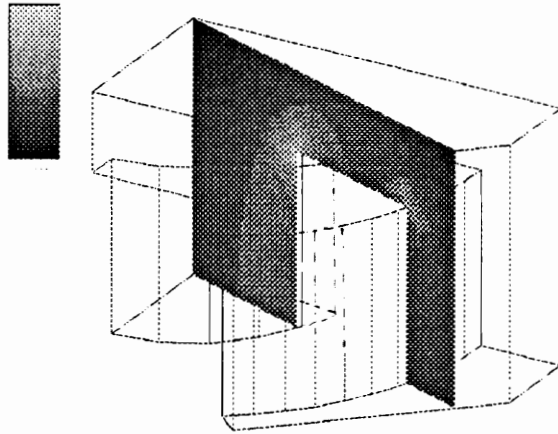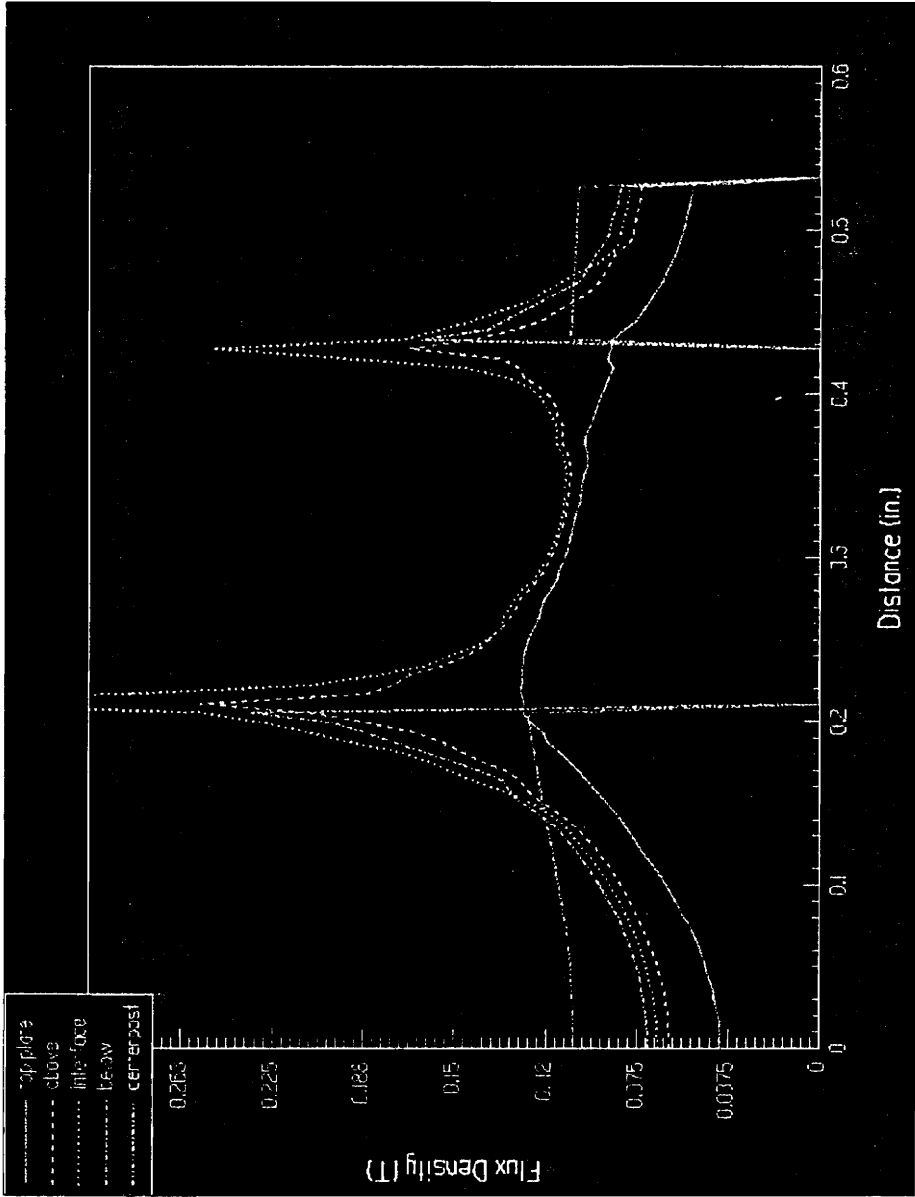(e)   the total core loss distribution on the lines

Fig. 4.17 The flux distribution on a vertical plane which has 20° angle with the yz plane, and the flux, the eddy current loss, the hysteresis loss, and the total core loss distributions on a set of horizontal lines which are the intersections of this plane and the five horizontal planes used in Fig. 4.11 ~ 4.15.

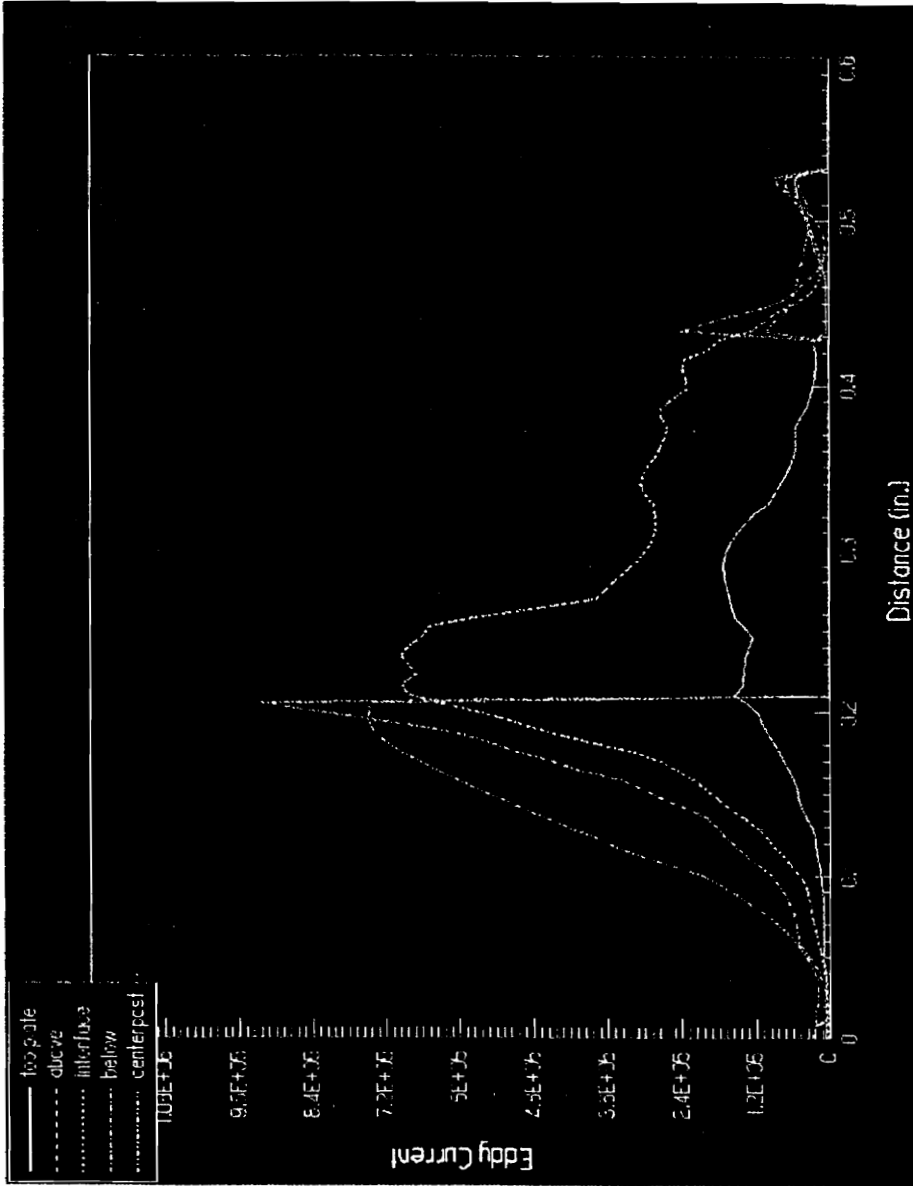(a)   the flux distribution on the vertical plane

Fig. 4.17 The flux distribution on a vertical plane which has 20° angle with the yz plane, and the flux, the eddy current loss, the hysteresis loss, and the total core loss distributions on a set of horizontal lines which are the intersections of this plane and the 5 horizontal planes used in Fig. 4.11 ~ 4.15.

(b)   the flux distribution on the lines

Fig. 4.17 The flux distribution on a vertical plane which has 20° angle with the yz plane, and the flux, the eddy current loss, the hysteresis loss, and the total core loss distributions on a set of horizontal lines which are the intersections of this plane and the 5 horizontal planes used in Fig. 4.11 ~ 4.15.

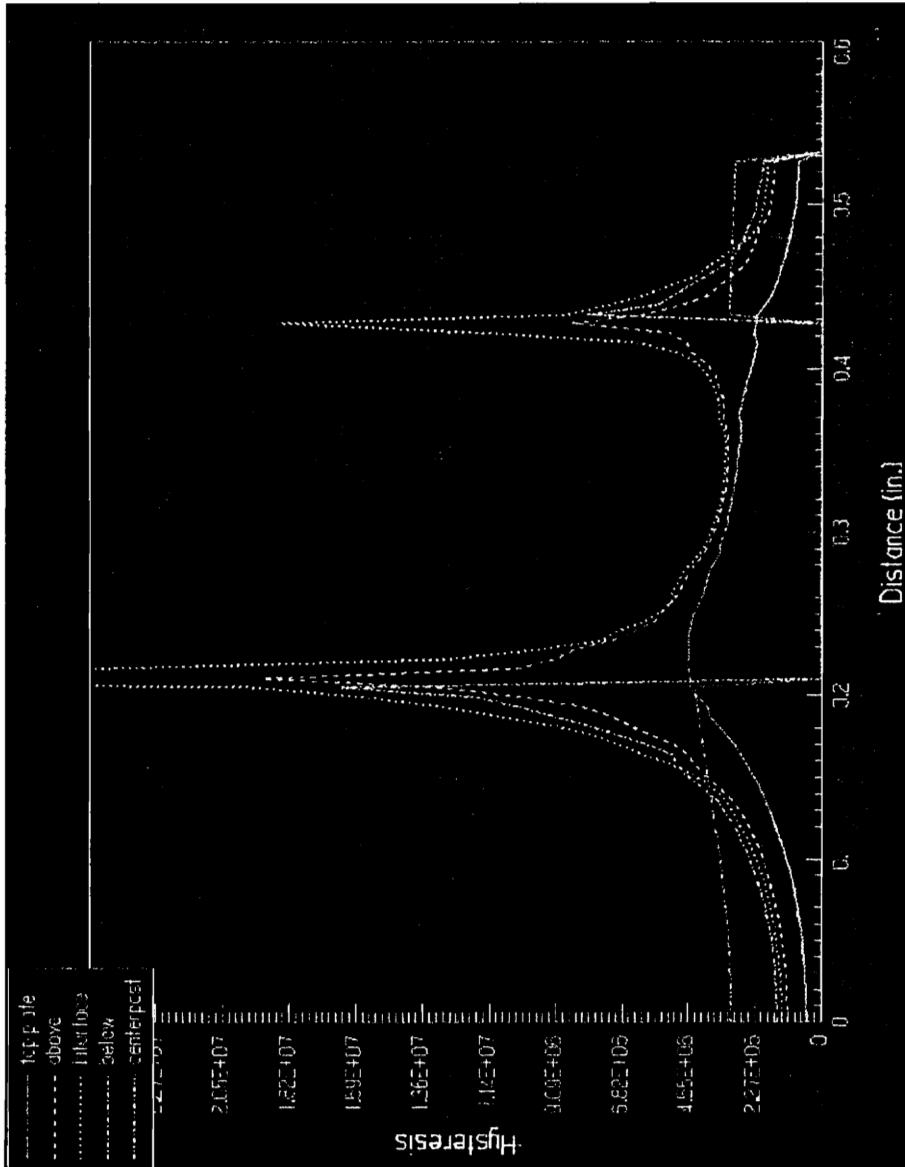(c)   the eddy current loss distribution on the lines

Fig. 4.17 The flux distribution on a vertical plane which has 20° angle with the yz plane, and the flux, the eddy current loss, the hysteresis loss, and the total core loss distributions on a set of horizontal lines which are the intersections of this plane and the 5 horizontal planes used in Fig. 4.11 ~ 4.15.
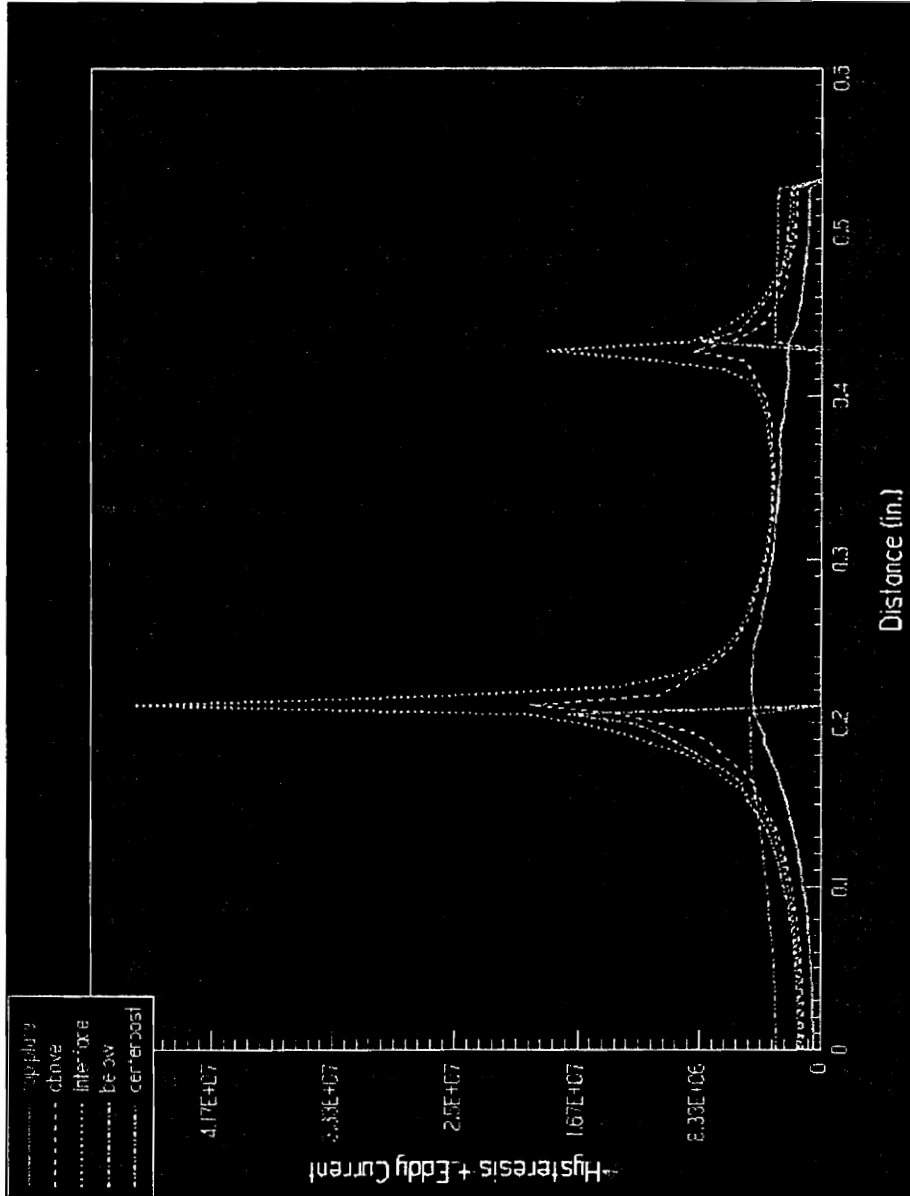(d) the hysteresis loss distribution on the lines

Fig. 4.17 The flux distribution on a vertical plane which has 20° angle with the yz plane, and the flux, the eddy current loss, the hysteresis loss, and the total core loss distributions on a set of horizontal lines which are the intersections of this plane and the 5 horizontal planes used in Fig. 4.11 ~ 4.15.

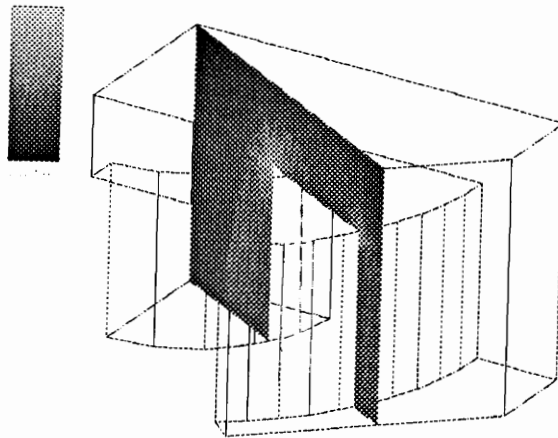(e)   the total core loss distribution on the lines

Fig. 4.18   The flux distribution on a vertical plane which has 30° angle with the yz plane, and the flux, the eddy current loss, the hysteresis loss, and the total core loss distributions on a set of horizontal lines which are the intersections of this plane and the five horizontal planes used in Fig. 4.11 ~ 4.15.

(a)   the flux distribution on the vertical plane

Fig. 4.18   The flux distribution on a vertical plane which has 30° angle with the yz plane, and the flux, the eddy current loss, the hysteresis loss, and the total core loss distributions on a set of horizontal lines which are the intersections of this plane and the 5 horizontal planes used in Fig. 4.11 ~ 4.15.

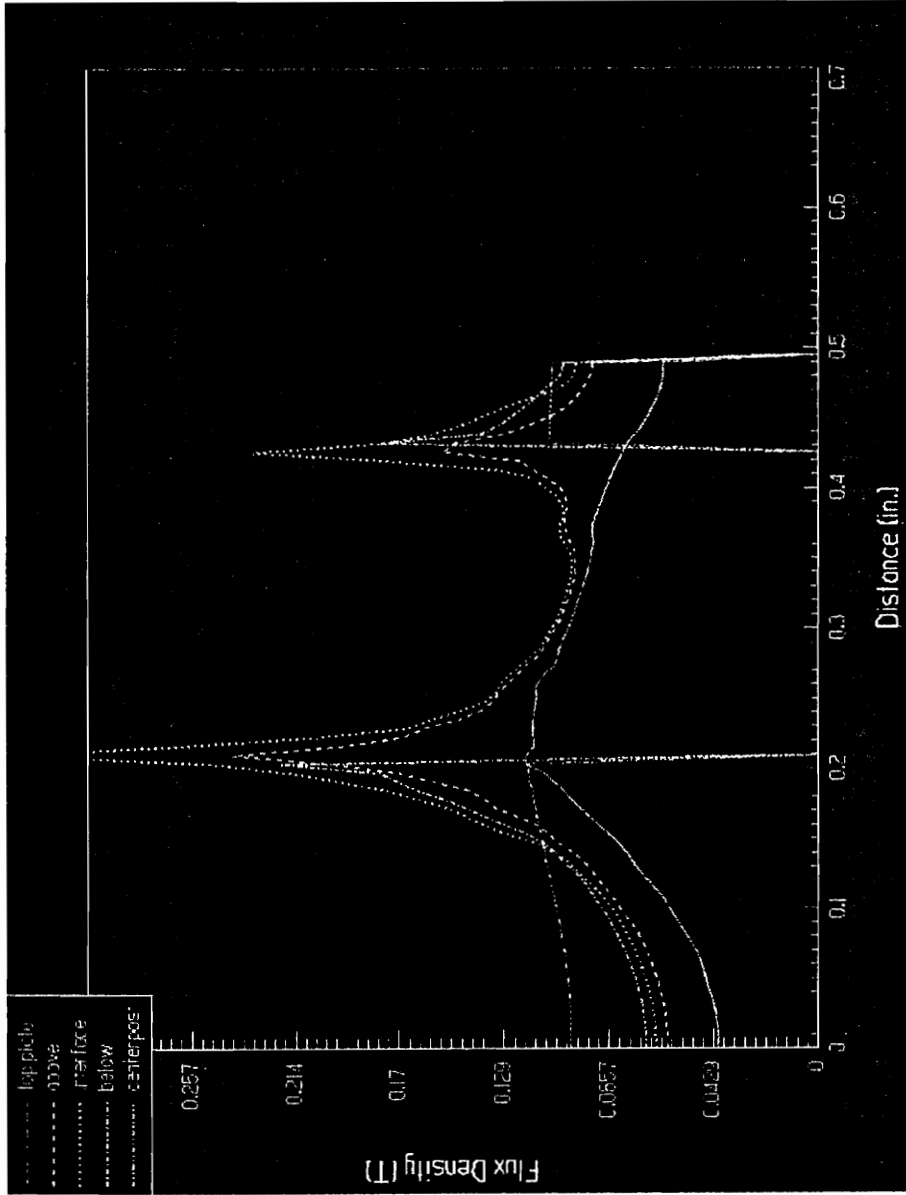(b)   the flux distribution on the lines

Fig. 4.18   The flux distribution on a vertical plane which has 30° angle with the yz plane, and the flux,
the eddy current loss, the hysteresis loss, and the total core loss distributions on a set of horizontal lines
which are the intersections of this plane and the 5 horizontal planes used in Fig. 4.11 ~ 4.15.
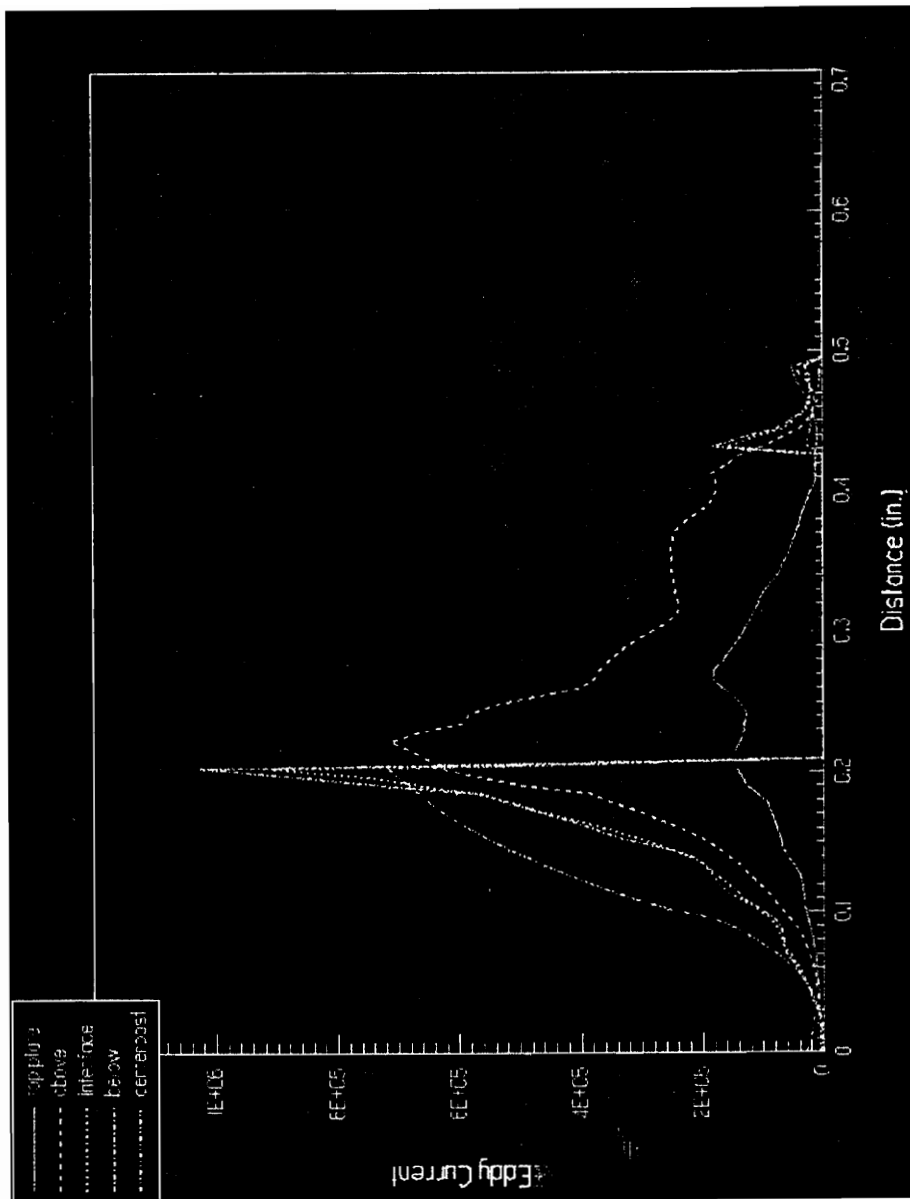(c)   the eddy current loss distribution on the lines

Fig. 4.18   The flux distribution on a vertical plane which has 30° angle with the yz plane, and the flux, the eddy current loss, the hysteresis loss, and the total core loss distributions on a set of horizontal lines which are the intersections of this plane and the 5 horizontal planes used in Fig. 4.11 ~ 4.15.
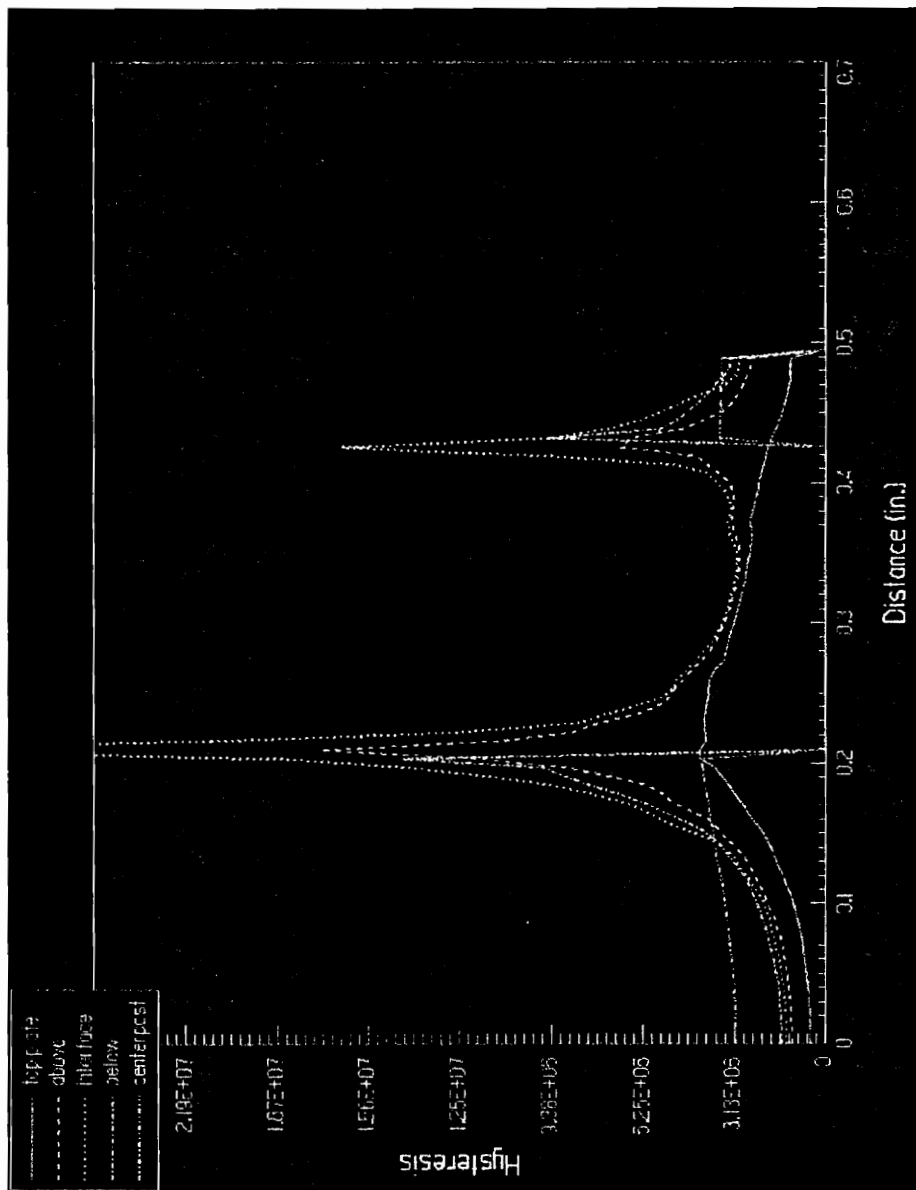(d)   the hysteresis loss distribution on the lines

Fig. 4.18 The flux distribution on a vertical plane which has 30° angle with the yz plane, and the flux, the eddy current loss, the hysteresis loss, and the total core loss distributions on a set of horizontal lines which are the intersections of this plane and the 5 horizontal planes used in Fig. 4.11 ~ 4.15.

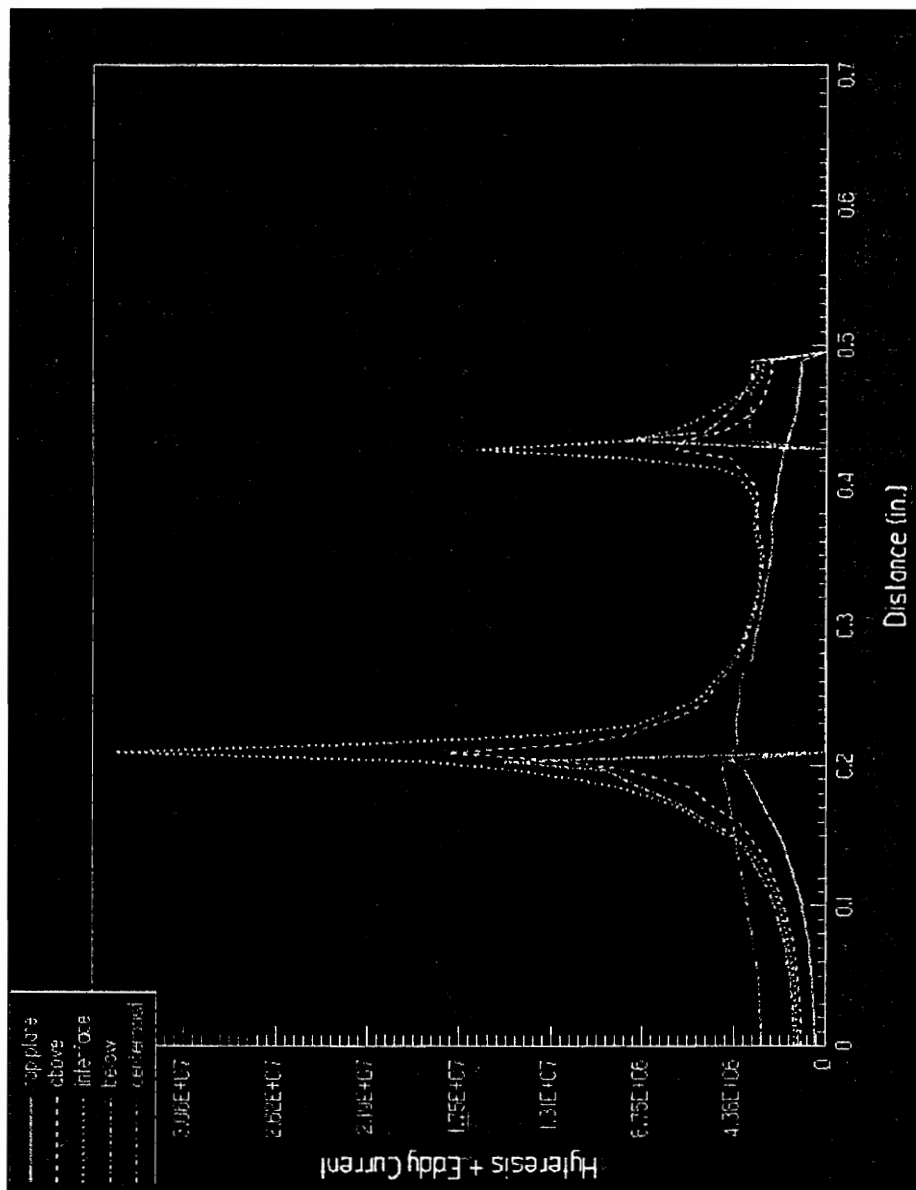(e)   the total core loss distribution on the lines

Fig. 4.19   The flux distribution on a vertical plane which has 60° angle with the yz plane, and the flux, the eddy current loss, the hysteresis loss, and the total core loss distributions on a set of horizontal lines which are the intersections of this plane and the five horizontal planes used in Fig. 4.11 ~ 4.15.

(a)   the flux distribution on the vertical plane

Fig. 4.19   The flux distribution on a vertical plane which has 60° angle with the yz plane, and the flux, the eddy current loss, the hysteresis loss, and the total core loss distributions on a set of horizontal lines which are the intersections of this plane and the 5 horizontal planes used in Fig. 4.11 ~ 4.15.

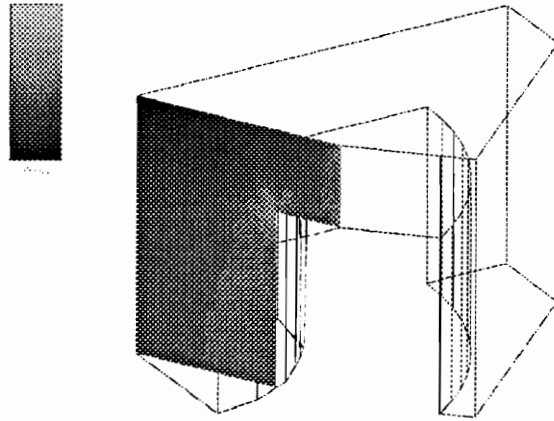(b)   the flux distribution on the lines

Fig. 4.19 The flux distribution on a vertical plane which has 60° angle with the yz plane, and the flux, the eddy current loss, the hysteresis loss, and the total core loss distributions on a set of horizontal lines which are the intersections of this plane and the 5 horizontal planes used in Fig. 4.11 ~ 4.15.

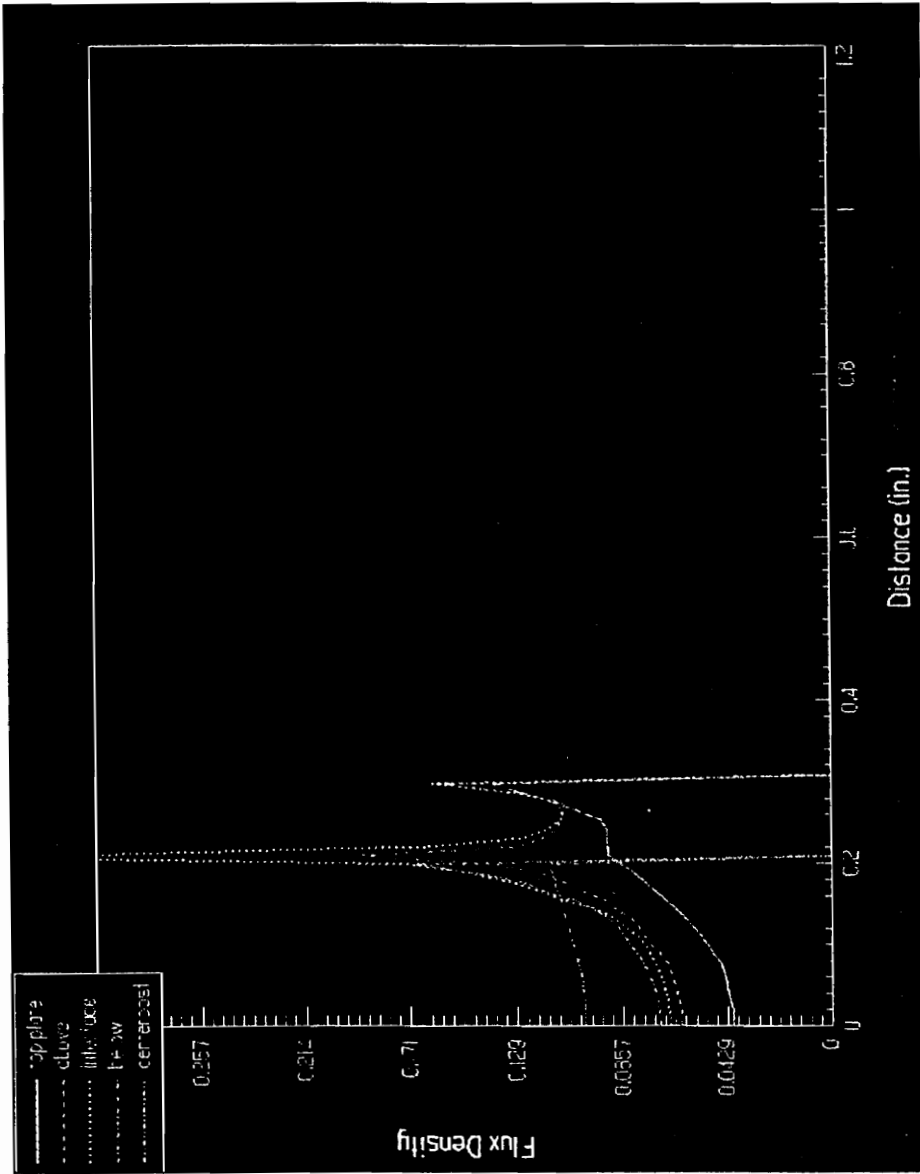(c)   the eddy current loss distribution on the lines

Fig. 4.19 The flux distribution on a vertical plane which has 60° angle with the yz plane, and the flux, the eddy current loss, the hysteresis loss, and the total core loss distributions on a set of horizontal lines which are the intersections of this plane and the 5 horizontal planes used in Fig. 4.11 ~ 4.15.
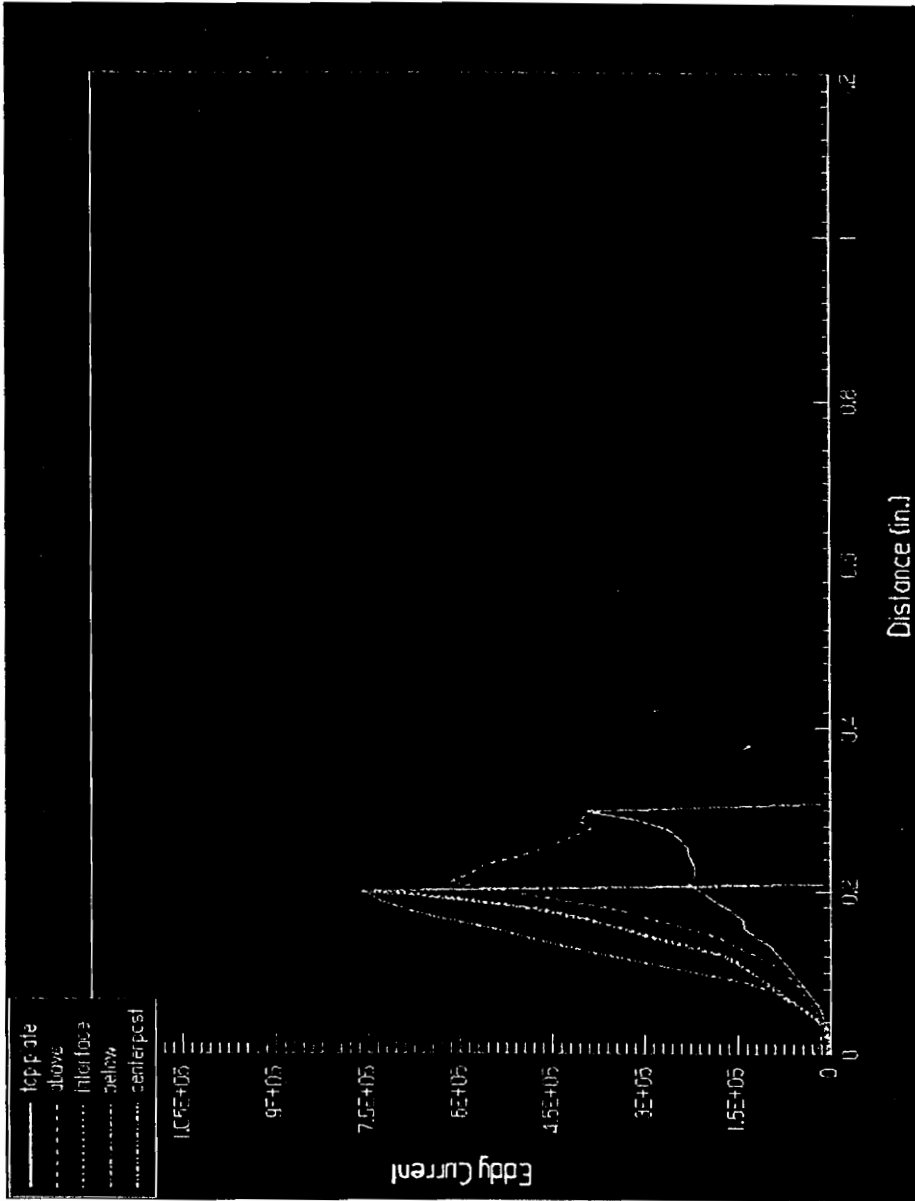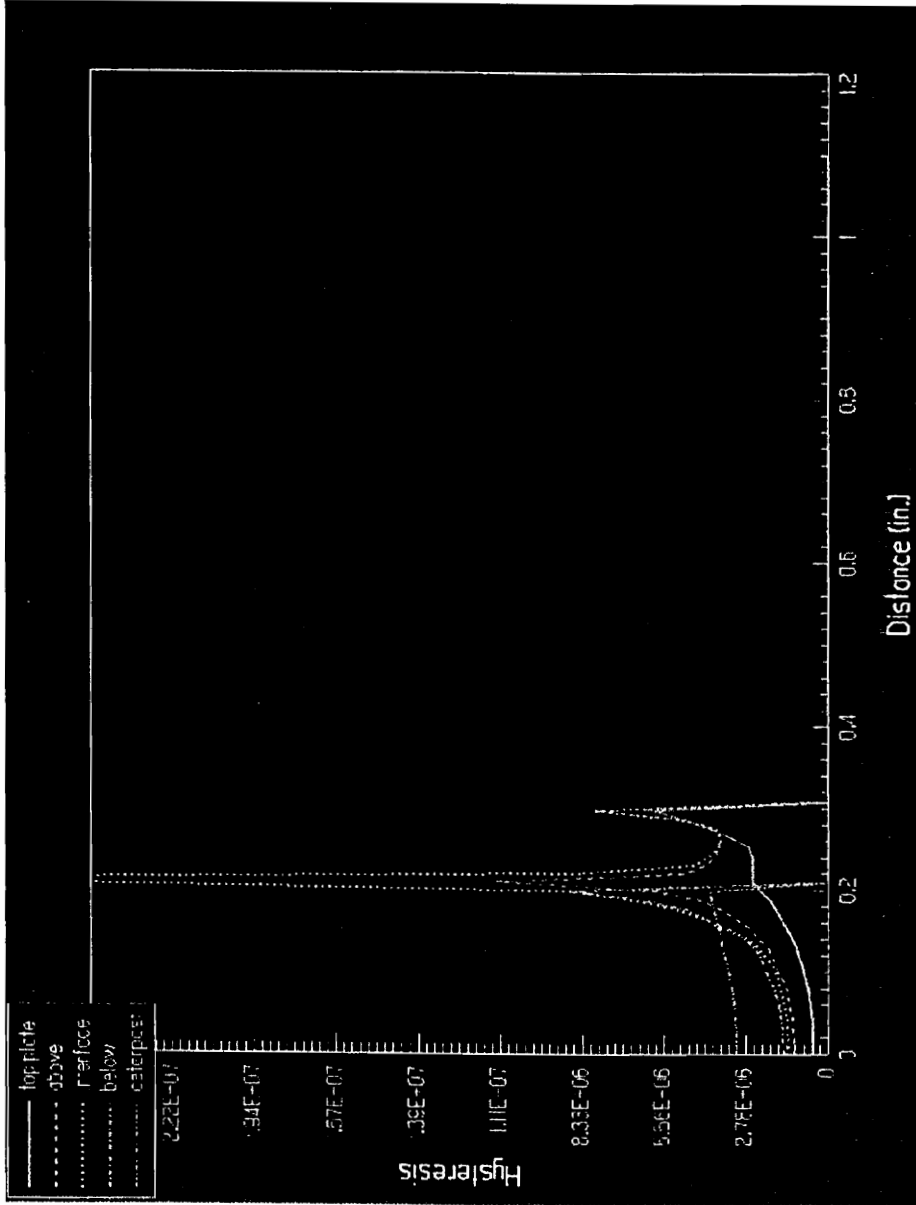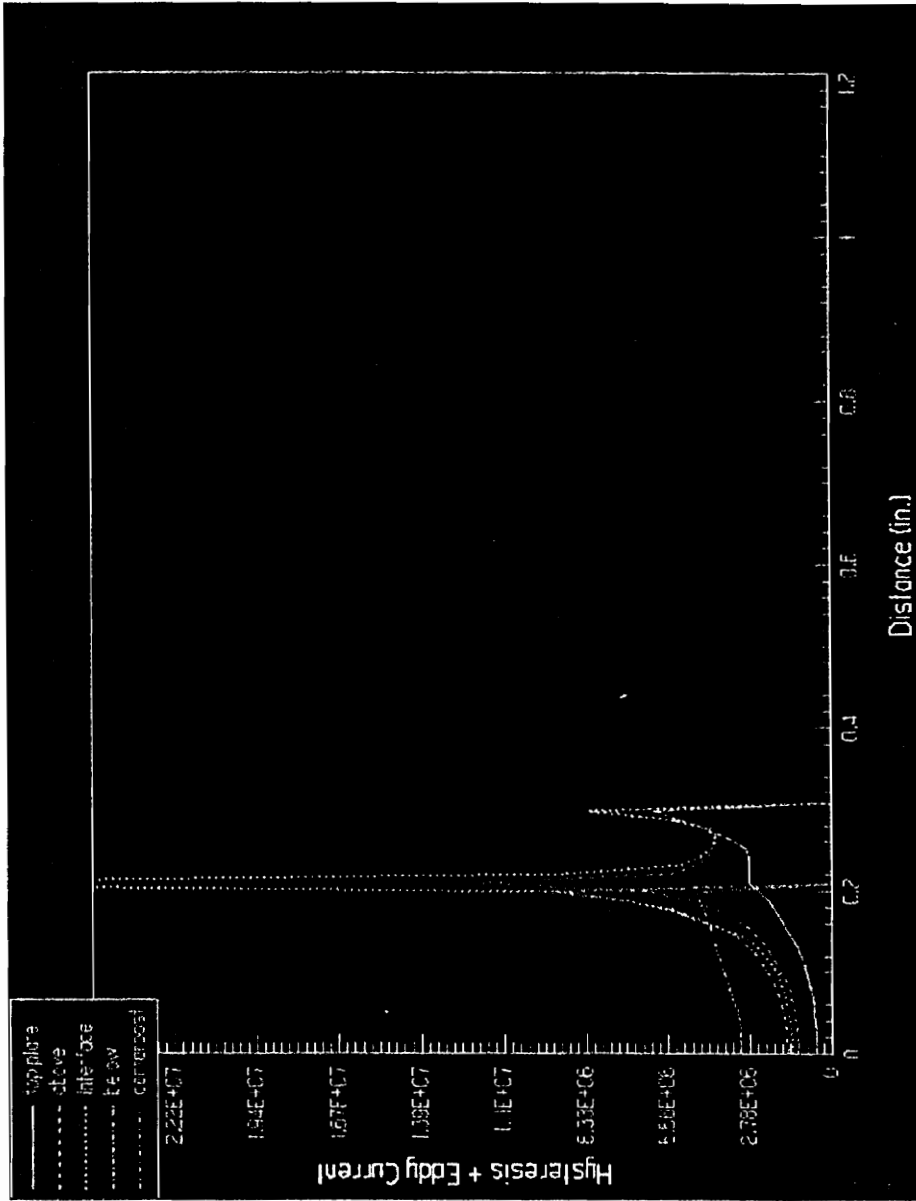(d)   the hysteresis loss distribution on the lines

Fig. 4.19   The flux distribution on a vertical plane which has 60° angle with the yz plane, and the flux, the eddy current loss, the hysteresis loss, and the total core loss distributions on a set of horizontal lines which are the intersections of this plane and the 5 horizontal planes used in Fig. 4.11 ~ 4.15.

(e)   the total core loss distribution on the lines

5. Conclusions and Future Work

This thesis includes two parts of work: the ferrite material characterization and FEA of the core loss in ferrite cores. Simulations require the characterized material data (the complex permeability, the conductivity, and the dielectric constant) as input. Since manufactures do not provide suitable material data required and there are no fundamental experimental test procedures available, the measurements of those material properties are first demonstrated in this work. The major contributions of this part of work are:

1. illustrating that the toroid with OD/ID ≈ 1 should be used in the magnetic properties (complex permeability) measurements to guarantee the flux uniformly distributed in the core and the eddy current loss negligible;

2. proposing that the imaginary component of the complex permeability should be measured at the frequency of interest instead of DC due to the frequency-dependent hysteresis in the ferrites;

3. pointing out that the use of the effective dimensions, A_e and l_e, which are defined at low magnitude of flux density, at the large-amplitude field conditions will influence the

accuracy of the core loss in the cores with non-uniform flux distribution. A more reliable core loss test method needs developing;

4. finding out why the AC conductivity, rather than the DC conductivity, should be employed in the simulation, and setting up a testing system in the laboratory.

All the material data are collected at room temperature in this research. Multi-temperature level measurements need to be done in the future work.

Based on the measured material data, FEA of the ferrite core loss are performed on the sample toroidal core, an EI core, and an RM10 core. There is very good agreement between simulated and measured core losses for the sample toroid. The simulations of the EI core and the RM10 core show how to simulate a core with an non-uniformly distributed flux. The comparison of the simulated core loss with the measurements has differences to some degree due to the measurements. So, more extensive verifications need to be done in the future. Also, more accurate solutions of core loss in greatly non-uniform flux cores rely on more powerful computer resources and a non-linear FEA solver.

References

[1] P. L. Dowell, "Effects of Eddy Currents in Transformer Windings", *Proc. IEE*, vol. 113, No. 8, pp. 1387-1394, August 1966.

[2] J. P. Vandelac and P. Ziogas, "A Novel Approach for Minimizing High Frequency Transformer Copper Losses", *IEEE Proc. PESC*, pp.355-367, 1987.

[3] Ashraf W. Lotfi, "The Electrodynamics of High Magnetics in Power Electronics", *Ph.D. Dissertation*, Virginia Polytechnic Institute and State University, Blacksburg, VA, 1993.

[4] B. Carsten, "High Frequency Conductor Losses in Switchmode Magnetics," *High Freq. Power Conv., Conference Proc.*, pp.155-76, 1986.

[5] F.W. Carter, "Eddy Currents in Thin Circular Cylinders of Uniform Conductivity Due to Periodically Changing Magnetic Fields, in Two Dimensions," *Proc. Cambridge Phil. Soc.*, Vol. 23, pp. 901-6, 1927.

[6] S. Butterworth, "Eddy-Current Losses in Cylindrical Conductors with Special Conductors with Special Applications to the Alternating Resistance of Short Coils," *Phil Trans. Roy. Soc. Lon.*, Ser. A, vol. 22, pp. 57-100, 1992.

[7] G. W. O. Howe, "The High-Frequency Resistance of Wires and Coils," *J. IEE*, vol. 58, pp. 152-61, 1920.

[8] G. M. O. Howe, "The High Frequency Resistance of Multiply-Stranded Insulated Wire," *Proc. Royal Soc. Lon.*, A, vol. 93, pp. 648-92, 1917.

[9] P. P. Biringer and K. Gallyas, "Analytical Approximations for Determining the Current Density and Power Loss Distributions in Multilayer Sheet Windings," *IEEE Trans. Ind. Appl.*, vol. IA-13, no. 4, pp. 315-20, 1977.

[10] L. Fleischmann, "Eddy Current Losses in Twisted Conductors," *J. AIEE*, vol. 47, no. 4, pp. 1062-4, 1924.

[11] P. D. Evans and K. H. El-Shara, "Losses in Foil-Wound Secondaries in High-Frequency Transformers," *IEEE Trans. Magn.*, vol. 25, no. 4, pp. 3125-32, 1989.

[12] *Maxwell® 3D Field Simulator User's Reference*, 3rd Ed., Ansoft Corp., 1993.

[13] *Flux2D*, version 7.11, Magsoft Corp., France, 1994.

[14] *Magnet5*, Infolytica Corp., Canada.

[15] *EMAS*, MacNeal-Schwendler Corp., CA.

[16] E. C. Snelling, "Soft Ferrites", *Butterworth*, London, 1988.

[17] D. C. Jiles and D. L. Atherton, "Theory of Ferromagnetic Hysteresis", *J. Appl. Phys.*, vol. 66, no. 6, pp. 2115-20, March 1984.

[18] L. G. Van Uitert, "Dielectric Properties of and the Conductivity in Ferrites", *Proc. of the IRE*, pp. 1294-1301, Oct., 1956.

[19] O. Inone, N. Matsutani and K. Kugimiya, "Low Loss Mn-Zn-Ferrites: Frequency Dependence of Minimum Power Loss Temperature", *IEEE Trans. on Magnetics*, vol. 29, no. 6, Nov. 1993.

[20] "Linear Ferrite Materials and Components", *Philips catalog,* 1984.

[21] V. J. Thottuvelil, T. G. Wilson, and H. A. Owen, Jr., "High-Frequency Measurement Techniques for Magnetic Cores", *Proc. PESC*, pp.412-425, 1985.

[22] Steef A. Mulder, "Loss Formulas for Power Ferrites and Their Use in Transformer Design", *Philips Components*, February 1994.

[23] J. R. Gatcia, J. M. Burdio, A. Martinez, and J. Sancho, "A Method for Calculating the Workpiece Power Dissipation in Induction Heating Processes", *Proc. APEC*, pp. 302-7, 1994.

[24] P. Han, G. R. Skutt, J. Zhang, and F. C. Lee, "Finite Element Method for Ferrite Coreloss Calculation", *IEEE APEC Proc.* pp. 348-53, March, 1995.

[25] P. M. Gradzki and F. C. Lee, "High-Frequency Core Loss Characterization Based on Impedance Measurements", *Proc. HFPC*, pp.108-115, 1991.

[26] David Jiles, "Introduction to Magnetism and Magnetic Materials", *Chapman and Hall*, 1991.

[27] J. F. Janak, "Dynamics of Diffusion-Damped Domain Wall Motion," *J. Appl. Phys.* vol. 34, no. 4, pp. 1119-20, 1963.

[28] D. Park, "Magnetic Rotation in a Polycrystalline Ferrite," *Phys. Rev.*, vol. 97, no. 1, pp. 60-6, 1955.

[29] T. G. W. Stijintjes and J. J. Roelofams, "Low-Loss Power Ferrites for Frequencies up to 500 kHz," *Adv. Ceram.* 16, pp. 493-500, 1985.

[30] I. D. Mayergoyz, "Mathematical Models of Hysteresis," *IEEE Trans. on Magn.*, vol. MAG-22, no. 5, pp. 603-8, September 1986.

[31]W. Roshen, "Ferrite Core Loss for Power Magnetic Components Design," *IEEE Trans. on Magn.*,vol. 27, no. 6, pp. 4407-15, Novenber 1991.

[32] P. Tenant and JJ. Rousseau, "Dynamic Model for Soft Ferrites", *IEEE, PESC Proc.*, pp. 1070-76, 1995.

[33] D. C. Jiles, "Frequency Dependence of Hysteresis Curves in "Non-Conducting" Magnetic Materials", *IEEE Trans. on Magnetics*, vol. 29, no. 6, Nov., 1993.

[34] J. Zhang, G.R. Skutt, and F. C. Lee, "Some Practical Issues Related to Core Loss Measurement Using Impedance Analyzer", *IEEE APEC Proc.*, pp.547-554, March, 1995.

[35] J. T. S. Irvine and A. R. West, "AC Electrical and Magnetic Measurements of a NiZn Ferrite", *Proc. ICF-5*, pp. 221-225.

[36] S. Ramada, E. Otsuki, and T. Otsuka, "AC resistivity of Mn-Zn Ferrites", *Proc. of INTELEC*, pp. 703-708, 1991.

[37] L. G. Van Uitert, "Dielectric Properties of and the Conductivity in Ferrites", *Proc. of the IRE*, pp. 1294-1301, Oct., 1956.

[38] J. N. Damask, "Characterization of Commercial Maganese-Zinc Ferromagnetic Materials", *M.S. Thesis, MIT*, 1990.

[39] *HP 16451B Dielectric Test Fixture Operation and Service Manual*, Hewlett-Packard, 1994.

Appendix A. The Derivation of Core Loss in Ferrites

In this section, the core loss formulas under sine drive conditions will be derived based on the electromagnetic field theory.

Maxwell's equations under sinusoidal excitations can be expressed in the complex form:

$$\nabla \times H = J + j\omega D, \tag{A.1}$$

$$\nabla \times E = -j\omega B, \tag{A.2}$$

$$\nabla \cdot B = 0, \tag{A.3}$$

$$\nabla \cdot D = \rho, \tag{A.4}$$

where **B** is the magnetic flux density,

E is the electric field intensity,

D is the electrical flux density,

J is the conduction and convection current density,

ρ is the volume density of free charges,

B, H, E, D, and J are phasors in the complex plane.

In the linear, homogenous, and isotropic media, there are several constitutive relations between field quantities:

$$B = \mu H, \tag{A.5}$$

$$D = \varepsilon E, \tag{A.6}$$

$$J = \sigma E, \tag{A.7}$$

where μ, ε, σ are the permeability, the dielectric constant, and the conductivity of the media, respectively. All of these quantities are material data.

In order to study the sinusoidal time-varying electromagnetic field, any field quantity, $A(t)$, can be expressed by a phasor, $A(\omega t)$, as shown in Fig. A.1.

In particular, $A(t)$ changes with time sinusoidally:

$$A(t) = A_m \cos(\omega t + \theta). \tag{A.8}$$

In the complex plane, $A(t)$ can be represented by a rotating phasor, $A(\omega t)$, which has the initial phase angle, θ, and rotates around the origin at angular speed. $A(\omega t)$ can be expressed as

$$A(\omega t) = A_m e^{j(\omega t + \theta)}, \tag{A.9}$$

where the magnitude of $A(\omega t)$ is the same as the magnitude of $A(t)$. According to Euler's formula,

$$e^{j(\omega t + \theta)} = \cos(\omega t + \theta) + j\sin(\omega t + \theta). \tag{A.10}$$

The projection of $A(\omega t)$ on the real axis is the quantity $A(t)$ which oscillates sinusoidally with time as $A(\omega t)$ rotates. That is,

$$A(t) = \Re e[A(\omega t)] = \Re e[A_m e^{j(\omega t + \theta)}], \tag{A.11}$$

where $\Re e$ indicates the real component of a complex number.

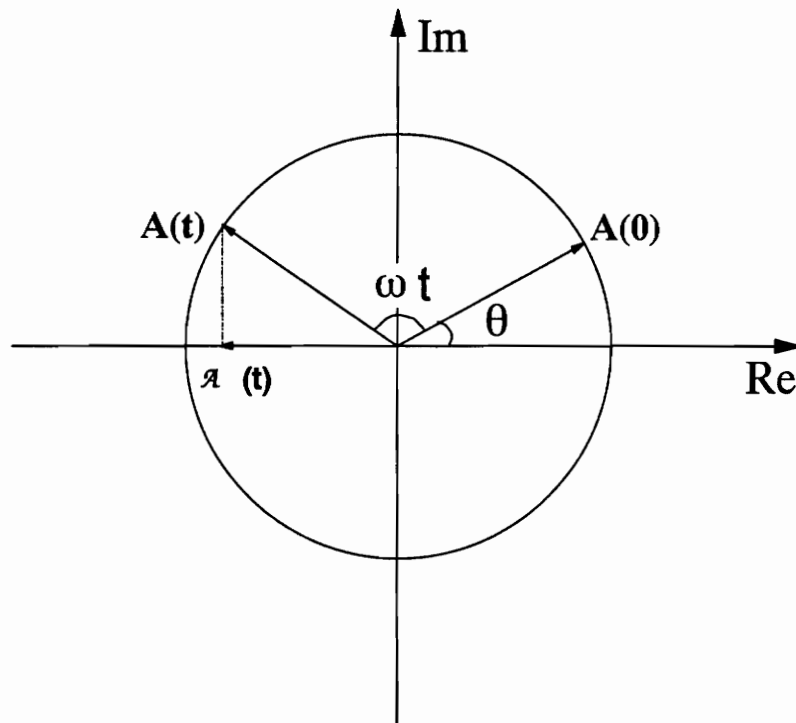Fig. 2.1 A phasor in the complex plane

Electromagnetic field is an energy carrier. The energy passing through δ, the unit area which is normal to the direction of energy flow, can be represented by the Poynting vector,

$$\delta(\mathbf{t}) = \mathcal{E}(\mathbf{t}) \times \mathcal{H}(\mathbf{t}). \tag{A.12}$$

$\mathcal{E}(t)$ and $\mathcal{H}(t)$ can be represented by the corresponding phasors,

$$\mathcal{E}(t) = \Re e(E(\omega t)) = \Re e(\mathsf{E}_m e^{j(\omega t + \theta 1)}), \tag{A.13}$$

$$\mathcal{H}(t) = \Re e(H(\omega t)) = \Re e(\mathsf{H}_m e^{j(\omega t + \theta 2)}), \tag{A.14}$$

where E_m and H_m are only spatial functions, not time functions.

Then the Poynting vector, $\delta(t)$, can be written in this form,:

$$\delta(\mathbf{t}) = \Re_e[E(\omega t)] \times \Re_e[H(\omega t)]. \tag{A.15}$$

If two general phasors **A** and **B** are considered, the following identity can be obtained.

$$\Re e(A) \times \Re e(B) = \frac{1}{2} \Re e(A \times B^* + A \times B) \quad . \tag{A.16}$$

Eq. (A.15) can be written in another form according to above identity,

$$\delta(t) = \frac{1}{2} \Re e(E(\omega t) \times H^*(\omega t) + E(\omega t) \times H(\omega t)). \tag{A.17}$$

The time-average power density, $S = < \delta(t) >$, can be obtained by integrating $\delta(t)$ over the period, T,

$$S = \langle \delta(t) \rangle = \frac{1}{T}\int_0^T \delta(t)dt = \frac{1}{T}\int_0^T \frac{1}{2}\Re e(E(\omega t) \times H^*(\omega t) + E(\omega t) \times H(\omega t))dt$$

$$= \frac{1}{T}\int_0^T \frac{1}{2}\Re e(E_m H_m e^{j(\theta 1 - \theta 2)})dt + \frac{1}{T}\int_0^T \frac{1}{2}\Re e(E_m H_m e^{j(2\omega t + \theta 1 + \theta 2)})dt.$$

(A.18)

Since the first term on the right hand side of Eq.(A.18) is independent of time, its integration over the period is equal to itself. The integration of the second term equals zero, as shown in Eq. (A.19):

$$\int_o^T (E \times H)dt = \int_0^T \frac{E_m H_m}{2\omega} e^{j(\theta 1 + \theta 2)} de^{j2\omega t} = \frac{E_m H_m}{2\omega} e^{j(\theta 1 + \theta 2)}(e^{j2\omega t}|_0^T) = 0.$$

(A.19)

Hence, we know,

$$S = \langle \delta(t) \rangle = \frac{1}{2}\Re e(E(\omega t) \times H^*(\omega t)).$$ (A.20)

Next, the divergence of $\langle \delta(t) \rangle$ can be expressed as

$$\nabla \cdot \langle \delta(t) \rangle = \nabla \cdot [\frac{1}{2}\Re e(E(\omega t) \times H^*(\omega t))] = \frac{1}{2}\Re e[\nabla \cdot (E(\omega t) \times H^*(\omega t))]$$

$$= \frac{1}{2}\Re e[H^*(\omega t) \cdot (\nabla \times E(\omega t)) - E(\omega t) \cdot (\nabla \times H^*(\omega t))].$$

(A.21)

Substitution of Eqs. (A.1) and (A.2) into Eq. (A.21) yields

$$\nabla \cdot \langle \delta(t) \rangle = -\frac{1}{2}\Re e[H^*(\omega t) \cdot (j\omega B(\omega t)) +$$

$$E(\omega t) \cdot J^*(\omega t) + E(\omega t) \cdot (j\omega D(\omega t))^*].$$

(A.22)

For two phasors, A and B, there is another identity,

$$(A \cdot B)^* = A^* \cdot B^*. \tag{A.23}$$

Also,

$$(j\omega D)^* = -j\omega D^*. \tag{A.24}$$

Eq. (A.22) turns to Eq. (A.25) by substituting Eqs. (A.23) and (A.24) into it:

$$\nabla \cdot < S >= -\frac{1}{2}\Re e[H^*(\omega t) \cdot (j\omega B(\omega t))$$
$$+E(\omega t) \cdot J^*(\omega t) - E(\omega t) \cdot (j\omega D^*(\omega t))]. \tag{A.25}$$

The Poynting theorem tells us that the average power, $\sum P$, coming into the volume is

$$\Sigma P = -\int_s < S > \cdot ds. \tag{A.26}$$

And the divergence theorem tells us,

$$\int_s <S> \cdot ds = \int_v \nabla \cdot < S > dv. \tag{A.27}$$

Therefore, $\sum P$ can be given by

$$\sum P = -\int_v \nabla \cdot < \delta > dv = \frac{1}{2}\int_v \Re e[H^* \cdot (j\omega B) + E \cdot J^* - E \cdot (j\omega D^*)]dv. \tag{A.28}$$

Vita

The author was born in China, on March 25, 1964. She received the B.S. and M.S. of Electrical Engineering in the area of electrical machines from Tsinghua University in China, in 1986 and 1988, respectively. She was then employed as a CAD engineer at Chinese Academy of Space Technology from 1988 to 1990. She was a master student at VPEC (Virginia Power Electronics Center) from 1993 to 1995, engaged in research in the areas of magnetics and power converters.